Development of Low-Energy Calibration Techniques for SuperCDMS using LEDs Operated at Cryogenic Temperatures

by

Muad Mohammad Ghaith

A thesis submitted to the
Department of Physics, Engineering Physics and Astronomy
in conformity with the requirements for
the degree of Doctorate of Philosophy

Queen's University
Kingston, Ontario, Canada
December 2020

Abstract

The desire to unveil the mystery of dark matter which, according to compelling astrophysical and cosmological evidence, constitutes about 85% of the matter in the Universe, drives physicists to continuously develop their tools and search methodologies. There are several proposed candidates for new particles among which the Weakly Interacting Massive particle (WIMP) is considered the most propitious.

The SuperCDMS SNOLAB experiment is a direct dark matter (DM) detection experiment. It is expected to start taking science data by the beginning of the year 2023. The plan is to start the operations with a total payload of ∼30 kg of Ge and Si detectors, situated in a well-shielded cryostat with ∼15 mK at the coldest thermal stage. The experiment aims to probe DM with masses down to 0.3 GeV (0.5 MeV) through nuclear (electron) scattering. To accomplish this, detectors have to have energy thresholds of a few eV.

The Cryogenic Underground TEst facility (CUTE) is currently the underground facility equipped to operate the future SuperCDMS detectors. Since summer 2019, the facility has operated a variety of detectors to identify, quantify, and mitigate its noise sources and investigate its potential for dark matter search while the construction of the SuperCDMS experiment is in progress. In this thesis, I discuss key contributions to setting up and commissioning the CUTE facility in a timely manner.

I also summarize the major tests and findings.

The low energy reach of the new SuperCDMS detectors brings the need for new calibration methods. We propose two different methods that use LEDs operated next to the detectors. This has initiated the study of LED properties at low temperatures. One of the suggested methods has been shown to be viable, and preliminary tests for the other method have shown promising results. Finally, I show the possibility of operating LEDs in the proximity of an eV-sensitive detector without impacting its performance.

To my parents, my wife and my kids.

Acknowledgments

The work presented in this dissertation is a result of collaborative work and support from many institutions and people. I think it will be almost impossible to acknowledge the support I had from each person. So, I am really grateful to each one I had the opportunity to meet and learn from throughout my studies.

Many thanks for my course instructors at Queen's University. I was fortunate to be in your class and I am really grateful for each one for being a wonderful teacher and mentor; Marc Dignam, Mark Chen, Philippe Di Stefano in addition to all the SNO group members. I have learned a lot from each one of you and during my study period.

Many thanks to Charles Hearns and Patrick Given for producing all parts necessary for my measurements in a timely manner. Many thanks to Loanne Meldrum for her continuous support during the whole period of my graduate studies. Thanks to Steve Gillen for your help and time whenever I needed for the work related to my setup with the LEDs and for allowing me to your equipment at any time. Many thanks to Samantha Millard and Julie McDonald for placing the purchase orders necessary for my work. Many thanks to all the graduate students for the useful discussions and nice time we had together.

A very special thanks to Abo Yuko-Lsametl from Marubeni Company (U.S.A), for providing us with the IR LEDs. The core component of many of the tests reported in my dissertation. Thanks to Afshin Namin for providing us with the fused silica wafer which was a basic component for building a prototype for an electron gun and thanks to Kiran Birdee for her help in coating the wafer with Al film.

Many thanks for the SNOLAB staff for the support I had during my work at the laboratory. Thanks to Silvia Scorza for organizing the work at SNOLAB, the nice dinner time after a very long day underground. Thanks to Kalpana Joshi for arranging the mining gear on time for my underground shifts.

Moreover, I had tremendous support from many members of the SuperCDMS collaboration. Many thanks for Bruno Serfass and Matt Pyle from the University of California, Berkeley, Tsuguo Aramaki from SLAC, Ziging Hong from Northwestern University, Matthew Fritts from the University of Minnesota and Emanuele Michielin from the University of British Columbia for all the useful discussions and their help in data interpretation, analysis or setup installation. I have learned a lot from each one of you. Many thanks to Sten Hansen for the continuous support whenever I had issues with the DCRC boards. I wish you, Sten, a nice retirement time.

Huge thanks to Gilles Gerbier for the great experience I had while working at the CUTE facility. Several tests reported in my dissertation would have been impossible to achieve without having this opportunity.

For Wolfgang's group, in no specific order: Adam Mayer, Ryan Underwood, Jonathan Corbett, Eleanor Fascione, Richard Germond. I am so grateful for the experience and time we spent together. And for all the support I received from each one. Without your help, I would not have been able to perform many of the measurements and without your help in performing many of the data analysis tasks, especially for the CUTE facility noise studies and the HVeV detector tests.

One key person is left. My supervisor, Wolfgang Rau. At this point I become speechless. I have learned a lot from you. So, I “believe” there are no words that can describe how grateful I am for each experience I had with you. I have made sure to learn something from you each day and you were always there for me. You have raised the bar for any supervisor in the support they can provide to his students. Thanks a million for each day we spent together in the lab (even if we stayed till after midnight :)), I truly enjoyed every moment. You made every day a new experience and dedicated your time to discuss everything with me. For every shooting star, Thank You, Wolfgang!

On the other side, and after going home late. I have always found the support and the understanding I needed. For that, I thank my beloved wife, Serene Farhan for her patience. You were there for me and for our kids (Wajd, Haya, and Rashid) at each step despite you were overloaded with your master’s degree at Queen’s. I don’t think I would have been able to go through this if you hadn’t been there for me at all times. I Love You :)

My parents, Mohammad Ghaith and Abla El Haje (may god be mercy on you): you have endlessly supported me, took good care of me, and provide me with the best education. For that, I am very grateful and honored to be your son. Thank You!

Statement of Originality

I certify that the work described within this dissertation is the original work of the author. Any assistance received in preparing this dissertation and resources have been fully acknowledged in accordance with the standard referencing practices and all figures have been produced by my self unless otherwise cited.

Muad Ghaith, November 2020

Glossary

CDMS: Cryogenic Dark Matter Search

CMB: Cosmic Microwave Background

CUTE: Cryogenic Underground Test Facility

DAQ: Data Acquisition system

DCRC: Detector Control Readout Circuit

DIB: Detector Interface Board

ER: Electron Recoil

GHS: Gas Handling System

HEMTs: High Electron Mobility Transistors

HV: High Voltage

iZIP: interleaved Z-Sensitive Ionization and Phonon

LED: Light Emitting Diode

LHC: Large Hadron Collider

NR: Nuclear Recoil

NTL: Neganov-Trofimov-Luk amplification

OF: Optimal Filter

PBH: Primordial Black Hole

POE: Power Over Ethernet

PSD: Power Spectral Density

QET: Quasiparticle-trap-assisted Electrothermal-feedback

QTF: Queens Test Facility

SM: Standard Model

SUF: Stanford Underground Facility

SuperCDMS: Super Cryogenic Dark Matter Search

SQUID: Superconducting Quantum Interference Device

TES: Transition Edge Sensor

VFC: Vertical Flex Cable

VIB: Vacuum Interface Board

WIMP: Weakly Interacting Massive Particle

Contents

List of Tables

List of Figures

Chapter 1

Introduction

1.1 The Early Universe

Scientists have explored the Universe in the last few decades, and made significant contributions to the whole civilization, for many generations to come. The big bang theory is the currently accepted model of cosmology, and if we consider the mathematical equations which describe the expansion of our Universe, as in Eqn. 1.1

$$(\frac{\dot{a}}{a})^2 \equiv H(t)^2 = \frac{8\pi G}{3}\rho(t) \tag{1.1}$$

where $H(t)$ is the Hubble parameter, $a(t)$ is the scale factor, $\rho(t)$ is the mass density of the Universe and G is the gravitational constant, then extrapolate our knowledge to the start of time, we reach to ∼13.8 billion years ago where there was nothing at a size of zero [1]. The term "Big Bang" refers to the very early seconds of this Universe when it was excessively hot. And thus, the Universe of which we are part of today was born.

The Universe was infinitesimally small but then, something happened and triggered this point to expand rapidly, allowing its interior contents to breathe. As the

Universe expands, its energy and temperature became finite and began to fall, which allowed atomic nuclei to form [2]. During the early expansion of the Universe, the metric of space-time itself has changed, so the current models are insufficient to determine what the Universe was actually like in its first moments. We also cannot rule out that the Universe was not physically small on its creation and we cannot conclude on a definite shape. The points between unbound objects and all parts of space-time have increased in unison and thus, there is no center. For this reason, it is said that the big bang happened everywhere and not at one initial point.

In the Universe today, we experience four fundamental forces: gravity, strong nuclear force, weak nuclear force, and electromagnetism. During the earliest increment of cosmic time, known as the Planck Epoch [3], these four fundamental interactions were bundled by extreme conditions of the micro-universe and were as one, in an overall unified fundamental force. We cannot test or verify that such a unified force existed, but many scientists assume that it did. It is also possible that the laws of physics, as we currently experience them, may not have applied under these extreme conditions either. Around 10^{-40}s later, things start to happen, gravity separates from other forces, and the temperature fell as the Universe expanded. As space cooled, the quantum fields which created the particles and forces we see today were able to settle at lower energy levels, becoming more stable. This increased stability has completely changed how these quantum fields interacted and caused the single force to break into two and continue as separate forces. This phenomenon is known as Symmetry Breaking, where the unified force continued as gravity and electro-nuclear interaction.

When the temperature fell below 10^{28} K, the electro-nuclear force broke into two separate interactions, strong and electro-weak interactions. The symmetry breaking had a profound effect on the Universe, as after this breaking occurred the Universe violently expanded in an event called Cosmic Inflation, as depicted in Fig. 1.1. This expansion caused the Universe to become at least 10^{78} more voluminous in under a trillionth of a second. The energy of this inflation decayed into the first elementary particles, the first tiny building blocks of information in the Universe. At this point, the entire Universe was filled with Quark-Gluon Plasma, which is why scientists believe that it was distributed homogeneously across space.

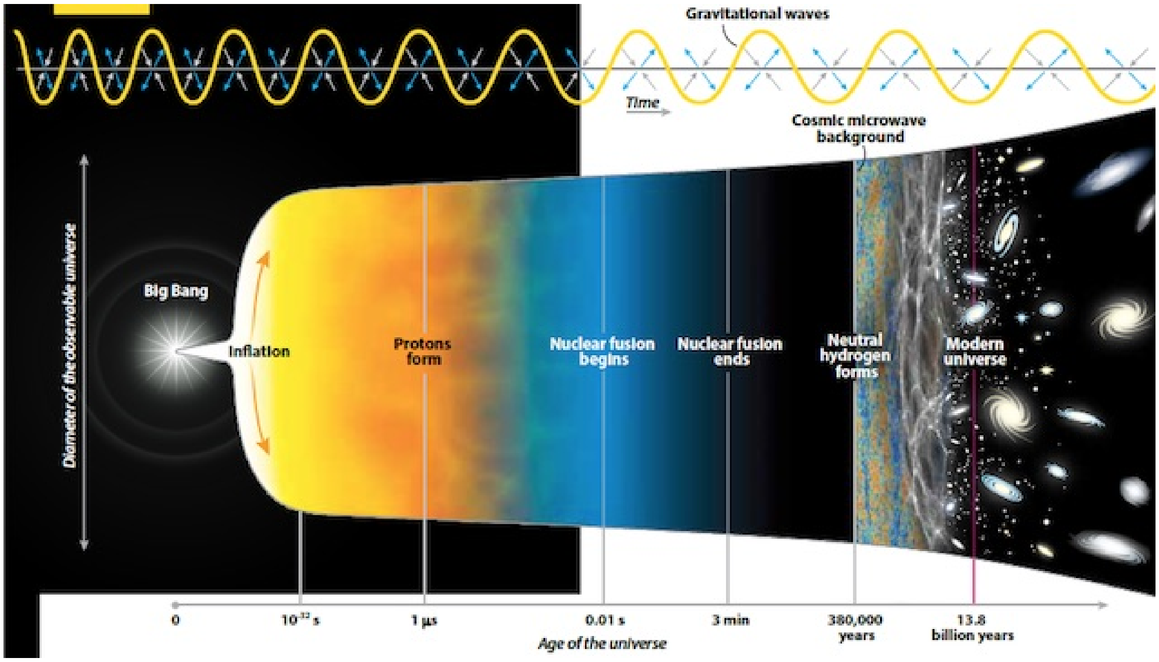

Figure 1.1: Inflation of the Universe. Image source: [4].

The density of the Universe fell dramatically during inflation and allowed the temperature to fall below the threshold of the third event of symmetry breaking. At this point, all the elementary particles created by the quantum field gained mass and electroweak interaction separated into electromagnetic and weak interactions, and the four fundamental forces that govern the Universe had been established. Thus, particles with mass had been formed and are bound by these forces.

Within the first pico-second of time after the big bang, the Universe had emerged and was hot, voluminous, and dense. But the fundamentals are now in place to occur among the elementary particles such as quarks and leptons [5]. These quarks and leptons are capable of binding together, but during this increment of time, known as the Quark Epoch, it was still too hot and energetic for binding to stick. But then, a millionth of a second after the big bang had occurred, the temperature of the Universe fell below this threshold and now quarks can begin binding without being destroyed. This led to Baryogenesis and bound pairs of two or more quarks began forming, such as protons and neutrons. As the temperature of the Universe decreased, there was not enough energy to form new particles, and most of the anti-particles annihilated others, creating high energy photons in the process. Only a small fraction of the hadrons remained in what is called the Hadron Epoch at ∼1 second of cosmic time [6–8].

After the formation of the neutrinos, they were still flying around because they only interact very weakly with matter. As such, there is strong evidence that these neutrinos created what is referred to as the Cosmic Neutrino Background of the Universe [9]. At this point, radiation dominates the behavior of the cosmos. Tiny random fluctuations in energy and continuity during the inflation have now led to some areas of the matter being denser than others. So, some scientists hypothesize that some areas might be dense enough to experience a gravitational collapse that is capable of forming a singularity, and the Universe may have seen its first Primordial Black Hole (PBH). These black holes are not formed by stars, therefore, they do not have to be as massive, as predicted by the late Steven Hawking, they might be as little as a billionth of a gram. PBH are considered good candidates for the seeds of supermassive black holes at the center of old large galaxies [10, 11].

In the 9 seconds that followed these early hypothetical black holes, the plasma was now composed of mostly leptons, in what is referred to as, the Lepton Epoch. So, now the Universe has protons, neutrons, and electrons. Between 2 and 20 min after the big bang, the temperature and pressure of the Universe allowed Nuclear Fusion to occur and its products to remain stable. So, protons and neutrons could now form the first atomic nuclei in what is called Nucleosynthesis. The resulting matter of the Universe after this period was about 75% Hydrogen (H), about 25% Helium (He), and less than a billionth of a percent Lithium (Li). Now photons continue to dominate the behavior of the Universe for about 50,000 years and as the Universe continues to expand; H and He are fairly homogeneously distributed across all over the space.

At about 47,000 years of cosmic time, the Universe has expanded so much that the density of photons is lower than the density of matter and the Universe's large scale behavior becomes dominated by matter rather than photons. This matter is composed of about 15% Baryonic matter and an estimated 85% Dark Matter. This dark matter helped to accelerate cosmic structure formation by adding mass. The dark matter clumps and gathers into huge filaments across space, the same way Baryonic matter would do. But because dark matter does not interact with light, and is not slowed down by radiation pressure, it groups faster than normal matter. So, these dark matter filaments formed quickly across space laying the blueprints for the first galactic mega structure billions of years later.

1.2 Evidences for Dark Matter

The effect of dark matter was first noticed in the year 1933. The astronomer Fritz Zwicky was the first to notice that, the galaxies in the Coma Cluster were not moving as he expected. Using the virial theorem, he found out that the galaxies are moving too fast to be gravitationally bound within a cluster, and there must be around 400 times the matter he saw, to explain the observed difference in rotation speed. So, he concluded the presence of “Dunkle Materie” or Dark Matter, which is invisible to the telescope but, whose gravitational effect held the cluster together [12, 13].

The search for dark matter started again a few decades later when Vera Rubin and a fellow astronomer, Kent Ford turned their attention to how the stars orbiting the centers of galaxies while they were measuring the ration curves [14].

1.2.1 Rotation Curves

The measured orbital speed of stars as a function of the distance from the center of a galaxy, given the distribution of both, stars and gas we can see, does not match what is calculated with the Newtonian and Einstein dynamics, as depicted in Fig.1.2 [15]. By applying Newtonian dynamics and gravity, we can calculate the expected dependence, given in Eqn. 1.2, but as we can see in Fig. 1.2 this does not match with observation. On the other hand, we can invert the equation and use it to calculate the mass distribution from the rotation curve to calculate how much the galaxy tugs at each particular star.

$$v(R) = \sqrt{\frac{GM(R)}{R}} \tag{1.2}$$

where $v(R)$ is the orbital speed, G is the gravitational constant, $M(R)$ is the total mass of the galaxy enclosed at radius R from the center of the galaxy.

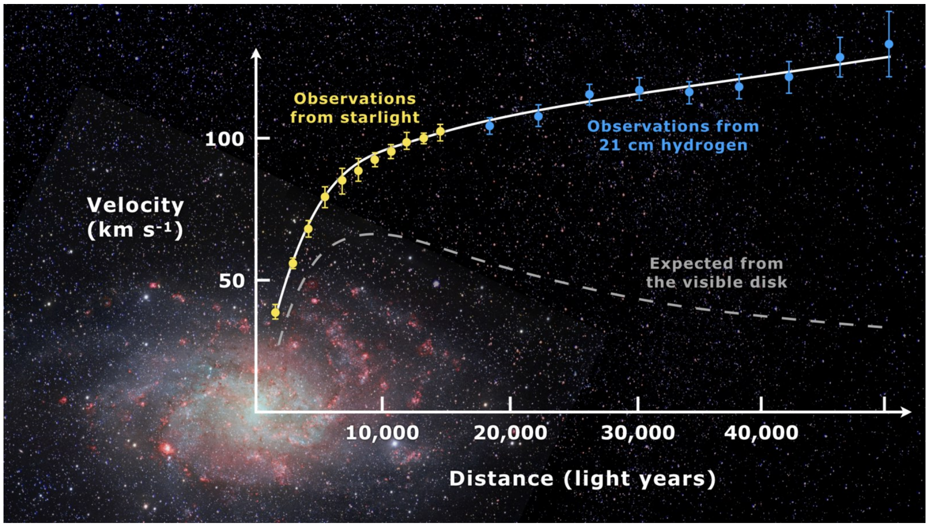

Figure 1.2: Orbital speed as a function of distance from the center of the spiral galaxy Messier 33. Yellow points are the measured velocities. The grey dashed line is the predicted velocity from the visible matter. Image source: [16]

Since the measured orbital speed is faster than what it should be, this discrepancy is attributed to the presence of an extra non-visible matter, dark matter.

1.2.2 Gravitational Lensing

From Albert Einstein's Theory of General Relativity, he concluded that objects do not orbit other objects because they are attracted together, instead, objects travel in a straight line in curved space. So space can be treated as malleable where its shape can be distorted. As an observation to prove the curving in space, we can use the gravitational lensing, which is caused by a large mass distorting and bending the path of light in the outer space, as shown in Fig. 1.3. So, on one side, gravitational lensing proves the wrapping in space, and on the other, it also proves the presence of huge invisible mass causing the bending in space.

Figure 1.3: The effect of gravitational lensing of galaxy Abell 370. The blue-ish arcs are the distorted light from galaxies far behind the cluster. Image source: NASA, ESA, J. Lotz and the HFF Team/STScI.

The net result will be an image of the distant light source that looks like a ring around the nearby mass (the lensing mass). Those rings are also called “Einstein rings”.

We can use the distorted images of galaxies to measure the mass between those distant galaxies and us, which also includes the amount of invisible matter. Scientists use microlensing which causes small distortions, to build the map of the dark matter in the Universe [17,18]. For example, the DESI experiment is using the gravitational lensing technique to produce a map for the matter in the Universe, including dark matter [19], similar to the one shown in Fig. 1.4. Basically, Einstein’s theory of General Relativity has allowed us to determine the structure of the Universe, both the visible and the invisible.

Figure 1.4: Visible matter combined with dark matter distributions in the supercluster Abell 901/902. The image consists of more than 80 images put together to cover the observed field of view. Image source: ESA/Hubble Images [20]

1.2.3 The Bullet Cluster

The Bullet Cluster (1E 0657-56) is located about 3.5 billion light-years away and is composed of two separate clusters that have collided with each other more than 100 million years ago. If we look at the separate clusters, we find that the galaxies have passed through each other and moved faster than the gas clouds, so they will be further away from the center of the collision. On the other hand, the surrounding gas collided and its location can be measured through its x-ray emission, as shown in Fig. 1.5.

If we separate out the two types of matter, the expectation is to have about 90% of the matter in the gas cloud, and that's where the strongest gravitational effects should be. But when gravity is measured by gravitational lensing, that was not the case. Instead, we see that most of the gravity is actually around the galaxies. That tells us that something else has to be there, such as dark matter, and it cannot be only the stars.

The bullet cluster is strong evidence for the existence of dark matter against other theories that do not involve dark matter, because in this case, the center of the observable mass is where the gas is, but the center of gravity is somewhere else. There is no way one can modify the fundamental laws such that the gravity is offset from the mass. Thus, the bullet cluster is very strong evidence against explanations that don't involve dark matter [21].

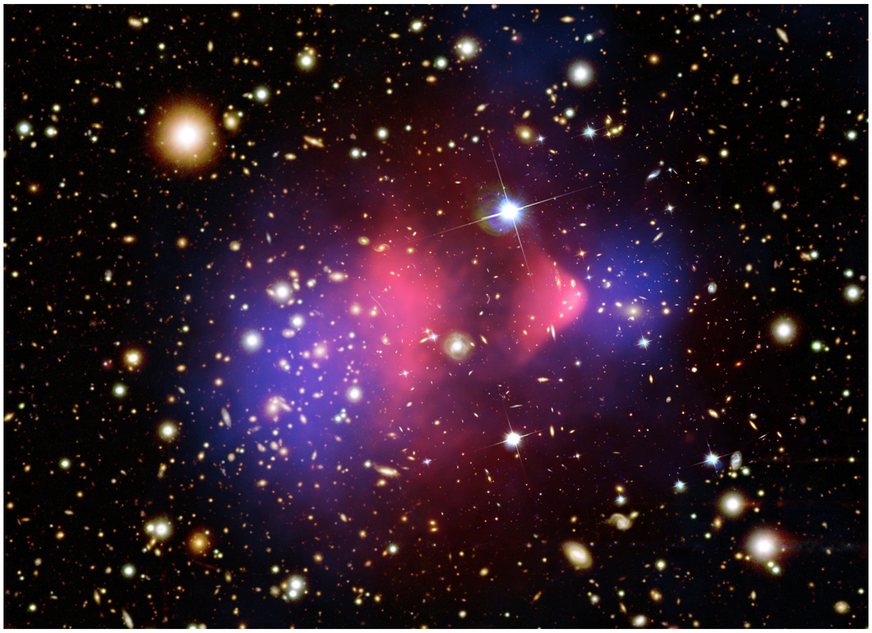

Figure 1.5: A composite image for the Bullet Cluster, combining X-ray data (in red), gravitational lensing data (in blue) in addition to optical image of the galaxies. Image source: [22]

1.2.4 Cosmic Microwave Background (CMB)

380,000 years after the big bang, the Universe had expanded and cooled down enough for the protons to capture electrons and from the Hydrogen atoms, then the Universe became transparent and photons could travel through space. Knowing that the Universe is expanding since that time, those photons red-shifted to the microwave range ∼13.5 billion years later.

The Planck satellite is orbiting a second Lagrange point of our Earth-Sun system and taking pictures in all directions of the sky and collecting microwave light which is considered the oldest light in the Universe. The CMB or "relic radiation" is shown in Fig. 1.6. The difference in color here represents the difference in temperature with tiny fluctuations. This light represents a historical snapshot of the whole universe with RMS temperature fluctuations of about 17 μK [23, 24].

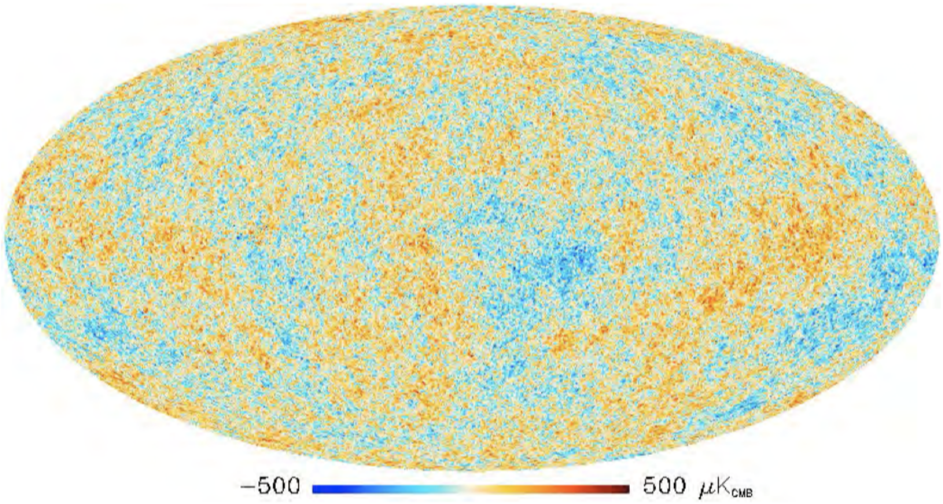

Figure 1.6: CMB for most of the sky with an angular resolution of 5' and about 17 μK RMS noise. Image source: [23]

The Planck CMB power spectrum plot, Fig. 1.7, can inform us about the root-mean-square fluctuations of the power on different scales. When the measurements of the angular power spectrum are fitted to a model of a small number of parameters, it included dark matter as one of the parameters. Hence, the model is able to perfectly describe the measurements.

Therefore, the strongest evidence for the existence of dark matter comes from CMB, because there is no way that the data points from the CMB can be fitted without the presence of collision-less dark matter, and it appears to out-number all the matter we can see by the ratio 5:1.

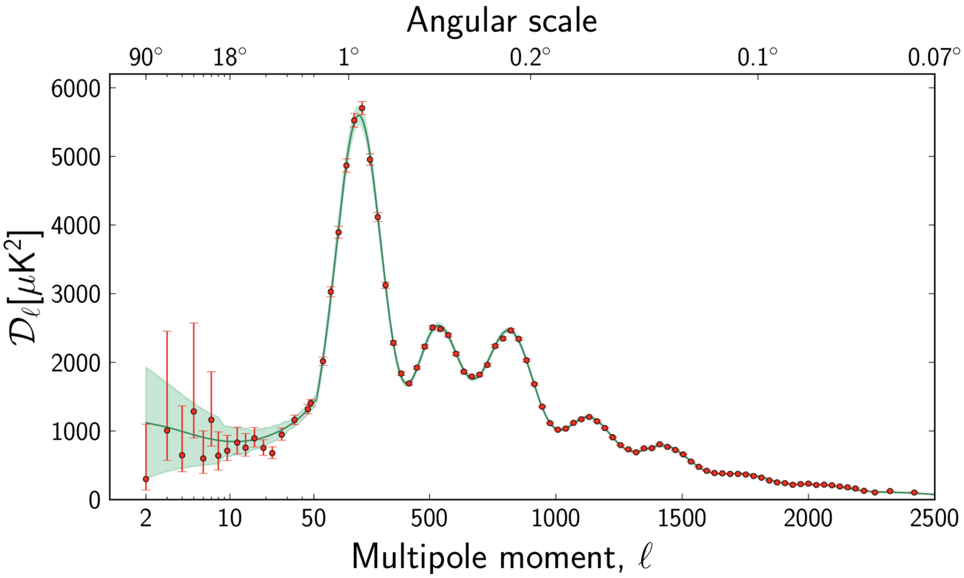

Figure 1.7: A well-fitted six-parameter angular power spectrum for 7 peaks using a six-parameter model. Area in green around the fit and error bars are the variance for the cosmic sample. Image source: [23]

1.3 Candidates of Dark Matter

The chart shown in Fig. 1.8, shows the elementary particles we understand in this Universe. So far, we do not know what the dark matter is, but at least we can confirm what it is not. The first thing we can do is, ruling out any particle that interacts via the EM force since dark matter does not interact with EM. This means we can rule out Quarks, electrons, muons, and tau in addition to the W boson. Then, if we rule out everything that feels the strong force, we cancel the quarks besides the gluon. Since dark matter is stable, we can also rule out the Higgs, Z boson. Eventually, we are left with only the neutrinos. However, neutrinos are too fast-moving, “hot” to clump the way we need. So, none of the particles listed in the Standard Model could explain the phenomena we observe that are attributed to dark matter.

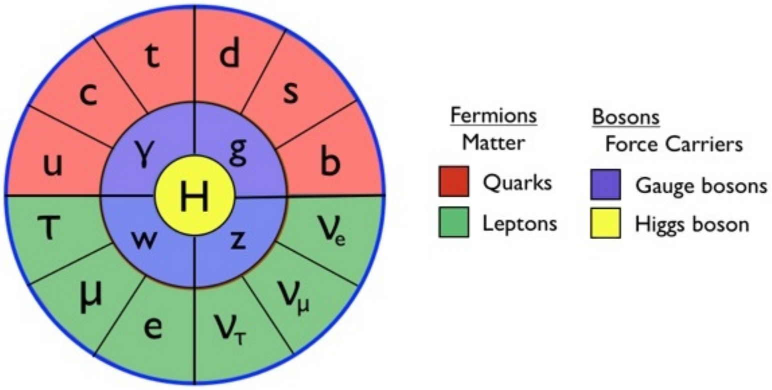

Figure 1.8: The Standard Model (SM) particles and force carriers. Image source: [25].

As the name suggests, dark matter is a type of matter that we cannot see, at least till this moment. We only infer its existence because of the gravitational effect it has. Astroparticle physicists have spent decades trying to identify what dark matter is made of. In this section, I will be listing some of the candidates along with the attempts taken to prove or disprove each candidate [26].

1.3.1 Primordial Black Holes

The Primordial Black Holes (PBH) are hypothetical objects which are expected to be in existence before the birth of the first star in the Universe. Since PBH did not originate from stars, they may have a wide range of masses, from fractions of a gram up to many times that of a giant star. Unlike Black Holes originating from stars, PBH is not expected to be surrounded by gas, which makes them harder to detect. As suggested by Stephen Hawking [10], those could make up at least some of the Universe's dark matter.

Research has been published recently showing the expectation for how abundant PHB might be. To find these Black Holes, the research group did a scan in the galactic halos, which does not have as many stars, gas, or dust as the galactic center. They looked for the change in the brightness due to expected gravitational lensing from such objects for more than 10 million stars in the outer fringes of the Andromeda and Milky Way galaxies [27, 28].

Only one event was found that may possibly be attributed to a PBH. If PBHs in the mass range of the search made up all dark matter, it would have been expected to see about a thousand PBH events in the collected data. Hence, having only one possible PBH, indicates that those PBHs could account for no more than 0.1% of dark matter [29, 30]. Recently, a study from Japan claimed to rule out PBHs, of any mass, to be the dominant source of dark matter [31].

1.3.2 Axions

Two famous physicists, Frank Wilczek and Steven Weinberg named this hypothetical particle after Axion detergent [32], because it seems to clean up the charge conjugation-Parity (CP) problem quit well. The Axion is expected to have no electric charge, nor quantum spin and would be extremely light, a tiny fraction of the mass of the electron. Even though Axions have no electric charge, they can still interact with the EM field and produce photons indirectly via the strong force. This can be done when photons convert into axion in the presence of a strong magnetic field in what is called the Primakoff effect, as depicted in Fig. 1.9 [33].

Figure 1.9: *Left*: Feynman diagram for the Primakoff effect. *Right*: The inverse representation of the Primakoff effect in the presence of a strong magnetic field. Image source: [33].

If they exist, Axions could be a fundamental particle that might change the laws of electricity and magnetism, even by a minor effect. So far, experiments have not given reliable positive results for the detection of Axion [34–36], but it could be possible that Axions are lighter or more weakly interacting than could be detected by current experiments.

The reason why Axions could be dark matter is that they have the right properties in terms of no direct interaction with light, and only weak interactions via the other forces. Moreover, if they exist, they are likely to have been produced in enormous numbers in the big bang, which means there could be enough of them to explain the invisible source of gravity that seems to dominate the Universe. And if Axions turn out to be real, they may solve two of the main problems, the strong CP problem and the nature of dark matter [37].

There are several experiments, such as ADMX [38,39], looking for Axion as a dark matter candidate and they have set several exclusion limits, as depicted in Fig. 1.10

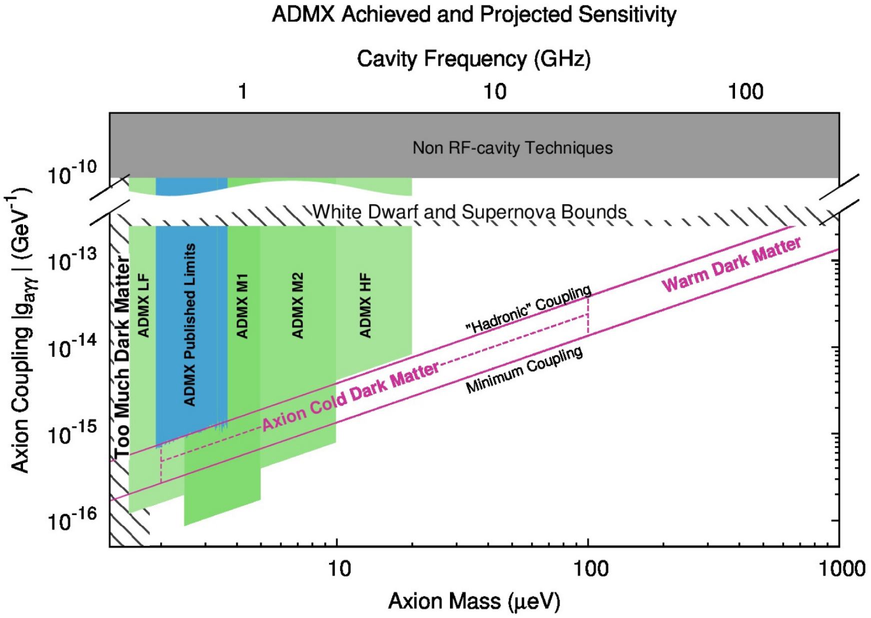

Figure 1.10: ADMX exclusion limits for Axion parameter space is the area highlighted in blue. The areas highlighted in green indicate expected sensitivities for future runs of the experiment. Image source: [39].

1.3.3 Dark Photon

The Dark Photon could be a new force-carrying particle, much like the regular photon, which is the force-carrying particle of electromagnetism [40].

It is dark because in theory, it only interacts very slightly with our everyday electromagnetic world which makes it effectively hidden from all previous experiments, and because it can help explain some of the odd astrophysical results related to dark matter.

Very recently, the SuperCDMS experiment has released results to set new limits for the dark photon. This was accomplished by using data collected from the former SuperCDMS experiment at Soudan. The limits were for electron recoil (ER) interactions, in the mass range of 40 eV/c^2 to 500 eV/c^2, as depicted in Fig. 1.11 [41].

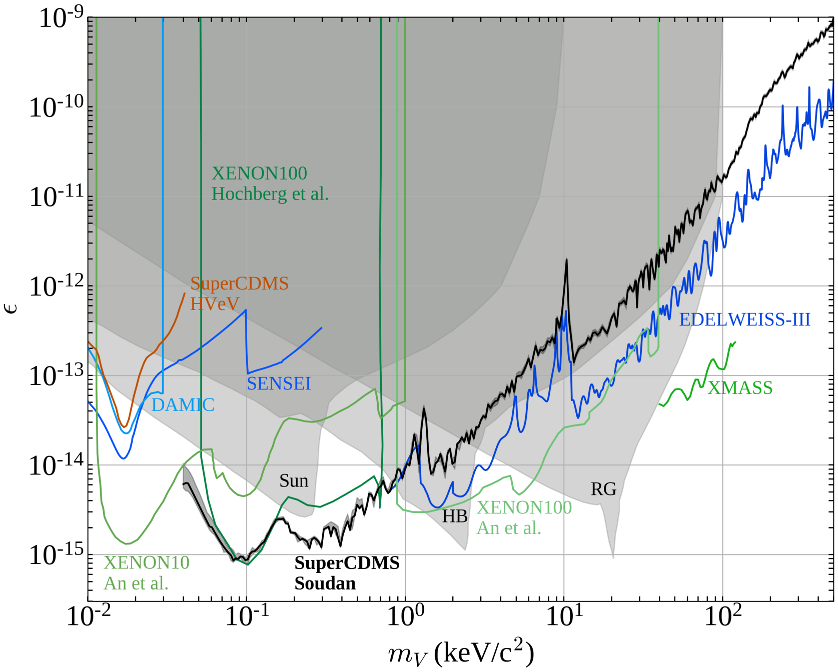

Figure 1.11: Limits on the parameter describing the kinetic mixing between standard photons and dark photons set by several experiments. The three shaded areas show the limits set from anomalous energy loss mechanisms in the Sun, Horizontal Branches (HB), and Red Giants (RG). Image source: [41].

1.3.4 The WIMP

The simplest picture scientists have for dark matter is a particle of mass between roughly 1 and 10,000 times the mass of a proton. This particle should have no electric charge, and it interacts with ordinary matter via gravity, and possibly involving forces weaker than what has been discovered so far. For this reason, scientists called this particle a Weakly Interacting Massive Particle (WIMP).

Using the WIMP idea, scientists could explain many mysteries starting from galactic rotation curves to the motion of vast clusters of galaxies. Because of the success of this theory, the WIMP idea is very well regarded in the astrophysics field. However, while the WIMP hypothesis would solve many mysteries in astronomy, it does not solve all of them. For instance, when the WIMP hypothesis is used to simulate the formation of large galaxies like the Milky way, the simulations predict many small satellite galaxies to be around the peripheries of the Milky Way. But when observations are made, astronomers could only find an order of magnitude fewer satellite galaxies. Also, the simulations predict that the small galaxies should be arrayed uniformly around the Milky way, while the observed satellite galaxies are located in a plane perpendicular to the Milky way's orbital plane. These discrepancies have pointed to a possible weakness of the WIMP theory. However, they are not enough to entirely disregard the theory, as tweaking in simulations may be possible to bring them into an agreement with what has been observed. Moreover, there is a number of proposed solutions to make some tweaks in the theory itself.

For instance, dark matter may have a different kind of charge, a Dark Charge. From analogy with electromagnetism, the particles carrying dark charge, could emit dark photons and feel the force of a dark electric field. Because ordinary matter does not carry this hypothetical dark charge, these dark photons pass by ordinary matter without interacting at all.

Finally, the WIMP is considered the most promising candidate for dark matter. There are several experiments such as, SuperCDDMS, LUX/LZ, PandaX-II, XENON, and many others [42–46], which are racing to search for dark matter. Therefore, each experiment sets new exclusion limits on the WIMP parameters. An example of the exclusion limits curve from some of these experiments is depicted in Fig. 1.12. More focus will be on the SuperCDMS experiment in Chapter 2 of my dissertation.

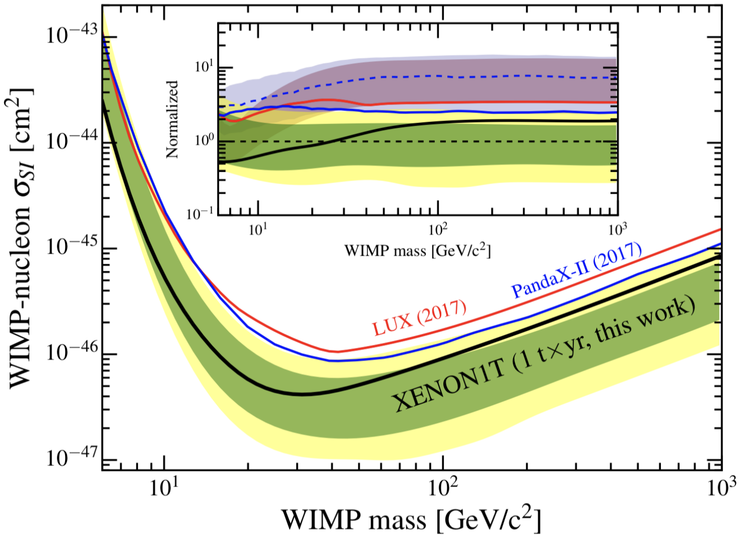

Figure 1.12: One of the limits is set by XENON 1T for nuclear-recoil elastic-scattering with 1σ and 2σ sensitivity bands highlighted in green and yellow. Image source: [43]

1.4 Detection of Dark Matter

There are three different classes of experiments to look for dark matter and to figure out what kind of matter or particle it consists of. The three search methods can be represented by the diagram shown in Fig. 1.13 and will be discussed in the following sections.

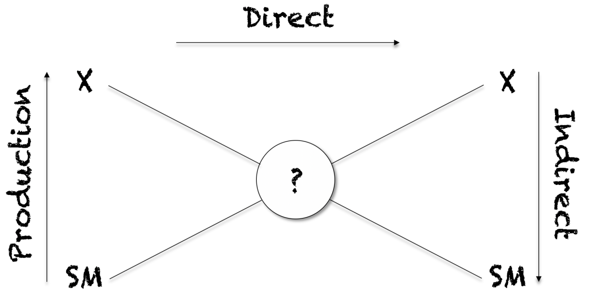

Figure 1.13: A diagram for the dark matter detection methods. Proposed Interactions between dark matter particle (χ) and baryonic matter (SM).

1.4.1 Dark Matter Production

Dark matter production experiments make an attempt to create dark matter particles by colliding protons together at very high energy. The violent head-on collision produces showers of exotic particles in all directions. Within this debris, dark matter particles might come into existence. The signature of these new particles could be found in experiments such as ATLAS and CMS by calculating the missing transverse momentum [47, 48]. Any missing momentum would be a direct indication of a new weakly interacting particle passing through the detectors without leaving a trace. An example of one of the most recent experimental exclusion limits is shown in Fig. 1.14. The limits set in this search method depend on interaction assumptions. Therefore, even if a new particle is found, it could not be proven that it was dark matter. That is because dark matter has to be very long-lived (billions of years).

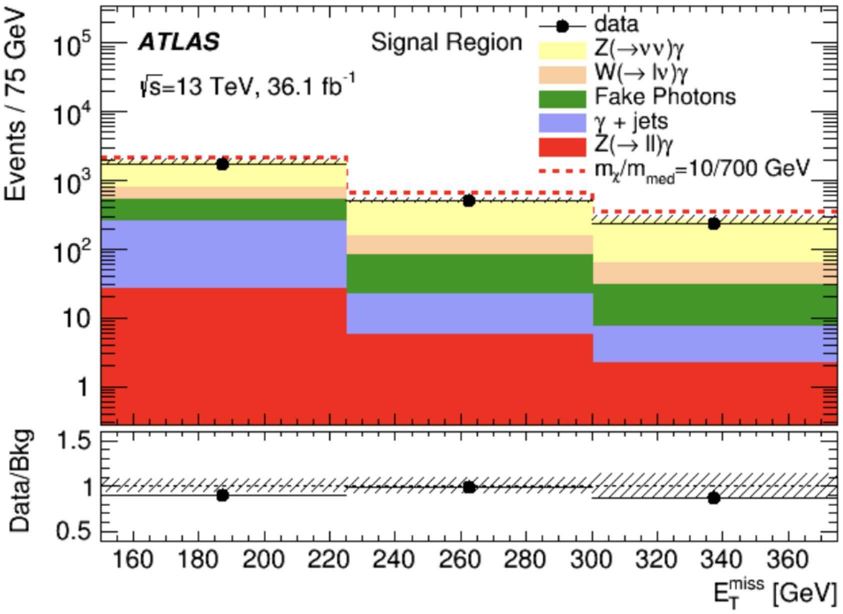

Figure 1.14: Red dashed line shows an example of WIMP scenario in a transverse missing momentum distribution. Image source: [49]

1.4.2 Indirect Detection Method

There are two expected signature classes for indirect detection. One class of signatures is that dark matter could decay into Standard Model particles that can be detected [49]. So, the observable signatures, in this case, are controlled by dark matter mass (total available energy), preferred decay channel (controls spectrum of products), and decay lifetime (controls rate). Since the lifetime should be much greater than the age of the Universe, the decay rate is proportional to 1/lifetime.

The other class of signatures is the annihilation of dark matter into a SM particle. The annihilation of dark matter is expected to produce various final states such as gamma rays, neutrinos, or charged cosmic rays, as depicted in Fig. 1.15 [31, 50]. However, the unknown signal and limited background knowledge are considered as some of the difficulties in the indirect dark matter search experiments [51].

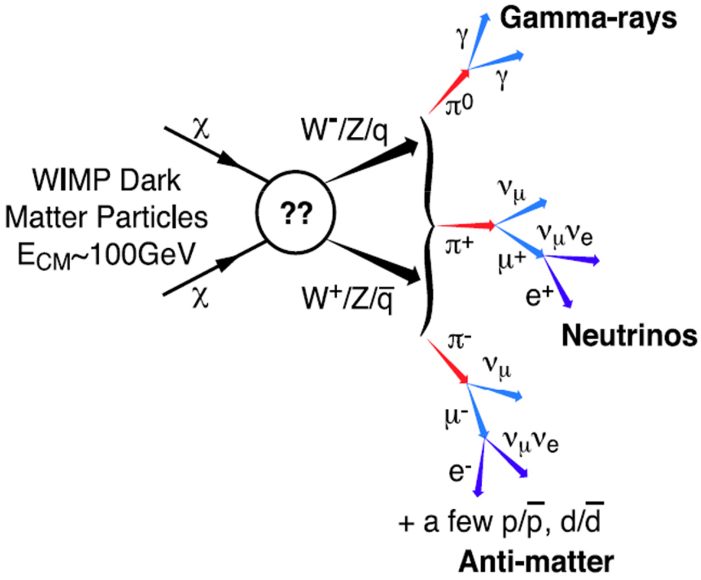

Figure 1.15: Representation of the dark matter annihilation processes into some detectable SM particles. Image source: [31]

1.4.3 Direct Detection Method

The direct detection method is searching for interactions between dark matter and regular matter through very small energy depositions in the detector material in the form of light, heat, and charge, as shown if Fig. 1.16. Because the dark matter we are trying to detect is bound to our galaxy, it must be non-relativistic with a typical velocity of a few hundred km/s. Therefore, the assumption is that they have low momenta, which could result in very small energy depositions into the detector material.

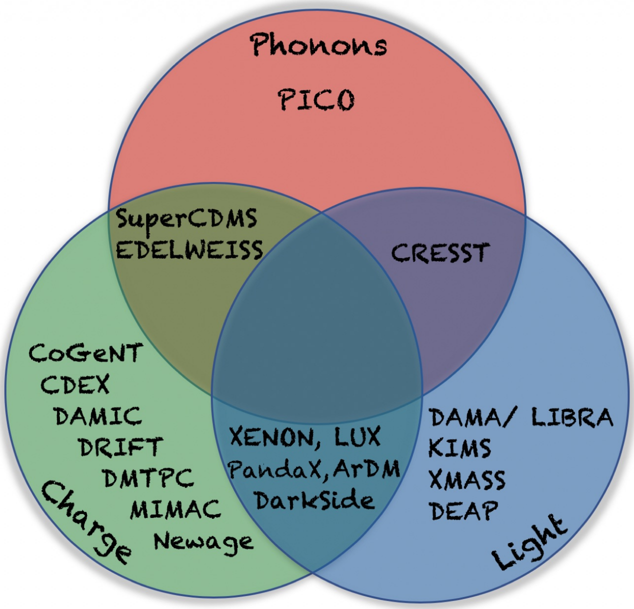

Figure 1.16: Classification of direct detection experiments based on their signal from their detectors.

In the direct detection method, the key feature is the local flux of dark matter in our solar system, where the local dark matter density is $\rho_o \approx 0.3$ GeV/cm^3 [52]. In terms of the number density, it depends on the mass of the dark matter particles and is given by: $n_o = \frac{\rho_o}{m_\chi} \approx \frac{10^3}{Liter}$ for a mass of 300 MeV.

In elastic collision interactions between the dark matter particle and the nucleus of the detector material, the recoil energy is given by:

$$E_R = \frac{|\vec{q}|^2}{2m_N} = \frac{\mu^2 v^2}{m_N}(1 - cos\theta) \tag{1.3}$$

where $\vec{q}$ is the momentum transfer, μ is the reduced mass which is equal to $m_N m_\chi/(m_N + m_\chi)$, m_N is the nucleus mass, m_χ is the dark matter particle mass, v is the dark matter particle velocity with respect to the target, and θ is the scattering angle. So, for a 100 GeV particle, the maximum energy transfer is about 100 keV. [53].

For the rate of interaction between the dark matter particle and direct search detectors, it is usually expressed in counts/kg/day/keV or dru (differential rate unit) and can be written as

$$\frac{dR}{dE_R} = \frac{\rho_o}{m_N m_\chi} \int_{v_{min}}^{\infty} v f(v) \frac{d\sigma}{dE_R}(v, E_R) dv \tag{1.4}$$

where $f(v)$ is the velocity distribution for the dark matter particle in the detector frame of reference, and the other term inside the integral is the elastic scattering cross-section between dark matter particle and nucleus. [54].

On the other hand, there are some models motivated by potential symmetry between dark matter and regular matter. These models predict that dark matter particles may have a mass of less than 10 GeV/c^2. This has encouraged experiments to further develop their detection instruments in order to be sensitive at the low mass range. This also requires that experiments should have a lower energy threshold to be able to detect low-mass dark matter particles. For example, the SuperCDMS experiment (which will be introduced in the next chapter), is aiming to be sensitive at the lower dark matter particle mass range [55,56]. An illustration for the expected recoil energy as the mass of dark matter particle change along with the proposed energy threshold is shown in Fig. 1.17.

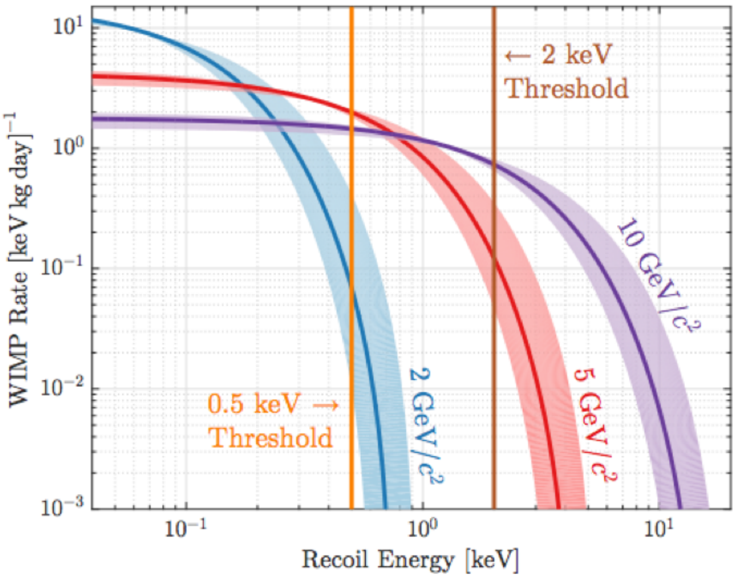

Figure 1.17: The expected WIMP rate for three mass values (0.5, 2 and 10 GeV/c^2). The ability to detect a lower mass requires a lower energy threshold as the vertical lines show. Image source: [57]

The direct detection experiments look for light, heat, or charge signal from the interaction between dark matter and their detectors, such as the ones shown earlier in Fig. 1.16.

1.5 Conclusion

Dark matter is still a big mystery, but this is an exciting time to be working on it. We have very clear evidence that it exists, from the scale of the smallest galaxies to the scale of the whole Universe. There are lots of possibilities for discovery, and we will definitely learn more about what dark matter is doing and what is not. Regardless of whether we will find that particle at anytime soon, but it's worth every step of the journey.

Chapter 2

The SuperCDMS Experiment

2.1 Introduction

The Super Cryogenic Dark Matter Search (SuperCDMS) experiment is a direct search experiment. The main idea of the experiment is to detect new particles utilizing ultra-pure Ge and Si crystals, cooled to mK temperatures, and shielded as best as possible from cosmogenic radiation and environmental radioactivity.

The CDMS experiment has started in the early 90s at Stanford Underground Facility (SUF) [58,59]. The second stage of the experiment, CDMS II started at SUF then moved to Soudan Underground Laboratory in Minnesota around the year 2003. The experiment was called SuperCDMS around the year 2010 in which improved detectors of interleaved electrodes were employed with a total of five towers, operated for several years. The many runs of science data have enabled the experiment to set competitive (at the time results were published) exclusion limits on the WIMP-nucleon cross-section and WIMP mass parameter space before being decommissioned at the end of 2015 [60–66].

Currently, the next phase of the SuperCDMS experiment is under construction at the new site at SNOLAB, near Sudbury, ON. It is expected to be completed by the end of 2022. Therefore, several R&D tasks are in progress to produce the new generation of detectors, readout electronics, and mitigate background sources. The dilution refrigerator is designed to be able to cool down the new detectors and readout electronics to the sub-Kelvin temperatures.

Due to the availability of resources and information about the experiment, there are many aspects and subsystems that will not be covered in this chapter. In this chapter, I will be giving a general overview of the experiment and the SNOLAB facility, reporting the current installation status, highlighting the latest results from the SuperCDMS experiment, and showing the projected sensitivities for SuperCDMS SNOLAB.

2.2 The SNOLAB Facility

The choice of experiment location for direct Dark Matter search experiments is vital to reduce the background levels from cosmic ray flux, and spallation induced products. Fig. 2.1, the left panel, shows the reduction in muon flux with depth for various underground facilities, where the overburden rock provides about 6,000 meter water equivalent (m w.e) of shielding.

Besides SuperCDMS, SNOLAB is currently the host of many DM and neutrino experiments, as shown in the right panel of Fig. 2.1. SNOLAB facility is an active mine where many local seismic events - rock bursts - can take place while experiments are running. Therefore, experiments sensitive to these vibrations, such as SuperCDMS, have taken the necessary measures to mitigate the effect of these vibrations.

In order to provide the experiments with the optimal operating conditions, the whole underground laboratory is designed to be a cleanroom of class 2000 [67].

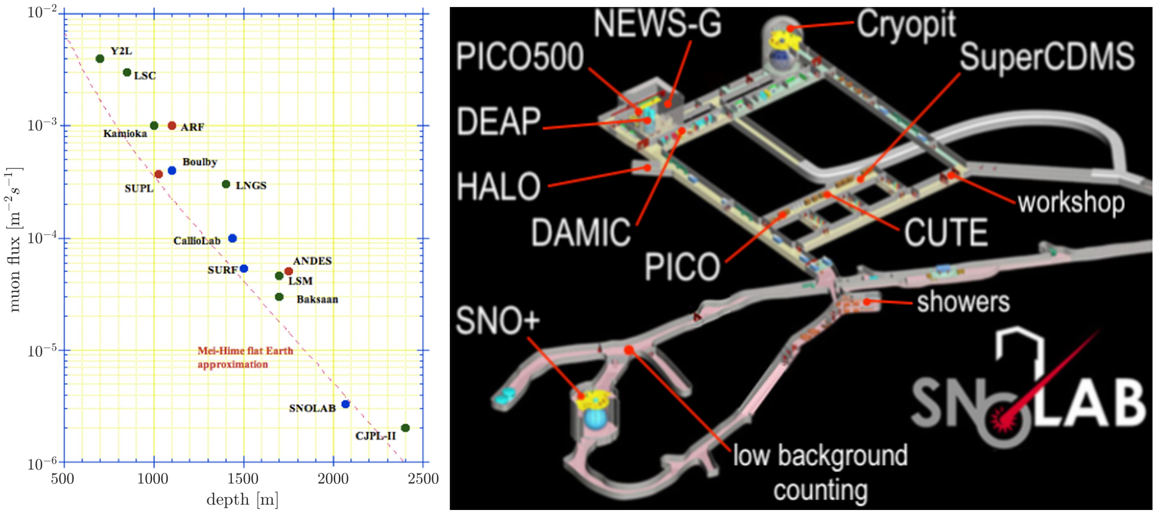

Figure 2.1: *Left*: The muon flux as a function of the depth at selected underground facilities [68]. *Right*: The layout for SNOLAB showing the names and locations of the physics experiments.

2.3 Experiment Overview

The SuperCDMS experiment will be employing two detector types: Interleaved Z-sensitive Ionization and Phonon (iZIP) detectors optimized for background discrimination, and detectors with a high voltage bias (HV), optimized for low threshold energy. In order to disentangle the expected signal from known or even unknown backgrounds, two different crystals will be used: germanium and silicon. Further discussion and details about the detectors will be in the next chapter.

There are several subsystems that are necessary for the full operation of the experiment. These systems include:

- The cryostat: a set of six nested copper cans used to hold the detector towers and cool them down to a few tens of mK temperature. The cryostat will be cooled down by a dilution refrigerator from Leiden Cryogenics with a cold finger that penetrates the shielding layers.

- The detector tower: is the mechanical fixture that holds the detectors and provides them with the electrical and thermal contacts.
- Calibration systems: an automated gamma calibration system, and provisions to insert a neutron calibration source through the shielding will be used to calibrate the detectors and monitor their stability. LED-based calibration methods may also be applicable and will be discussed further in this thesis.
- Data acquisition system: data will be transferred to a set of computers located next to the experiment to confirm that the detectors are operating properly. Afterward, data will be distributed to data centers in the US and Canada for processing and analysis.
- Cleanroom: a low-radon ($\sim$50 μBq/m^3) cleanroom of class 100 will be used for mounting the detectors and the towers into the inner cans of the cryostat to minimize the contamination risk and radon deposition at the setup surrounding the detector.
- Cryo-compressor: a two-stage cryocooler used for providing a continuous cooling power to keep the two outermost thermal stages at $\sim$50 K and $\sim$4 K.
- Backup power: regular maintenance is performed at the active mine near SNOLAB. This requires a scheduled power outage. Therefore, a generator backup power system will be installed on the surface to run the experiments during power outage periods.

- Chilled-water System: cooling water is necessary for the operation of the cryo-compressors. The cooled water will be provided by SNOLAB at a pressure that is too high for the equipment's internal circulations. Therefore, an auxiliary cooling system will be installed to reduce the pressure.
- Shielding: several layers of shielding will surround the experiment for shielding against environmental radioactivity.
- Seismic platform: the active mine causes local seismic events, powerful enough, that they might damage the experiment if they are not mitigated. Therefore, the whole experiment is situated on a spring-loaded platform for seismic isolation.

In the following sections, we will have a closer look at selected subsystems that have more relevance to the work detailed in the following chapters, such as the cryostat, detector towers, the shielding, and the seismic platform.

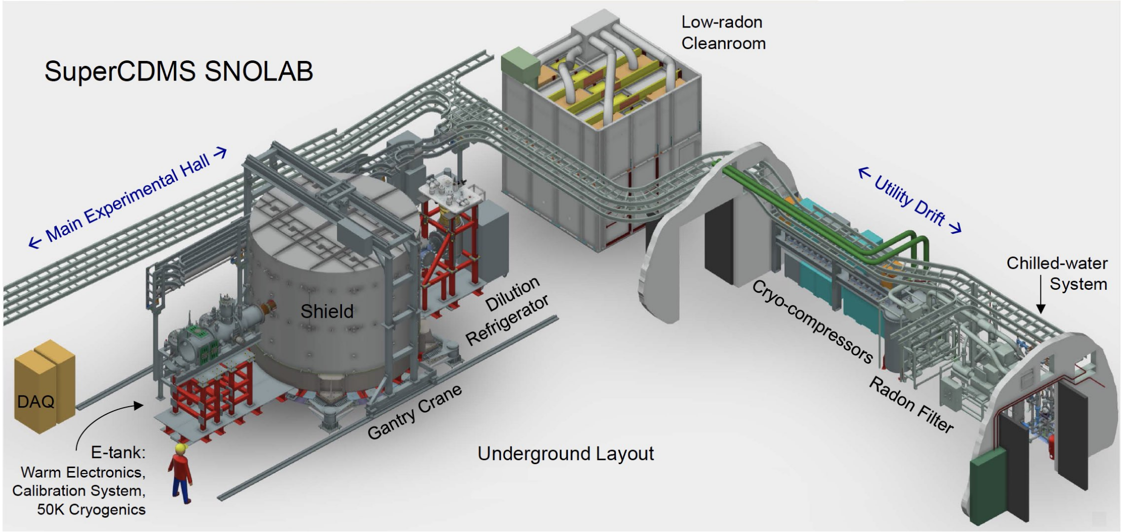

Figure 2.2: SuperCDMS SNOLAB layout. Image source: A 3D model annotated by Raymond Bunker.

2.4 The Cryostat

The design of the experiment at SNOLAB is based on the previous experience of the CDMS and SuperCDMS collaborations through the past three decades. The cryostat, a custom-built, six nested cylindrical copper cans (SNOBOX) will be attached to two stems, as shown in Fig. 2.3. One is called the C-stem, which will be connected to the cooling refrigerator, while the other is called E-stem, which will contain the readout cables and cooling fluids. The cans will be thermally isolated and each one is at a different thermal stage. The Room Temperature (RT) is the outermost can, followed by 50 K, Liquid Helium (LH), Still (ST), Cold Plate (CP), and Mixing Chamber (MC) with temperatures of RT, 50 K, 4 K, 1 K, 220 mK, and 30 mK respectively. The SNOBOX is designed to fit a total of 7 towers, six detectors in each tower, with a total initial payload mass of ∼30 kg.

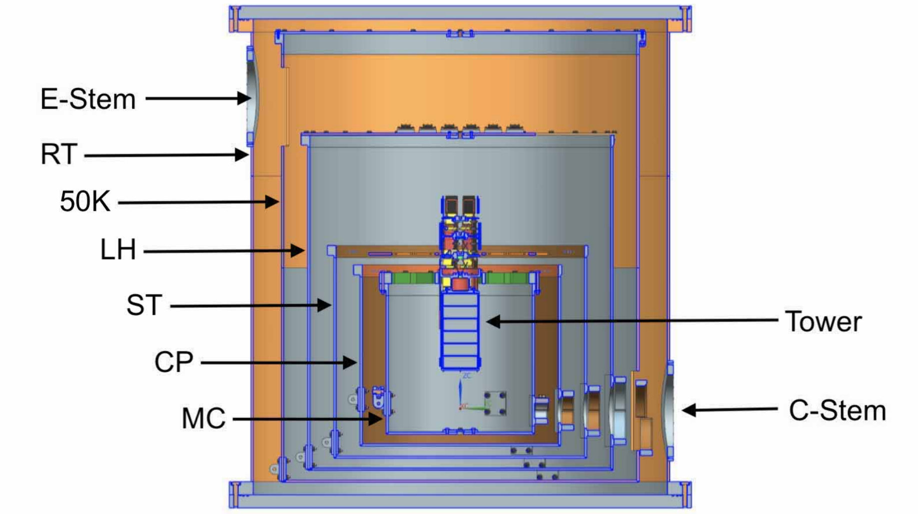

Figure 2.3: A cross-sectional view of the SNOBOX, showing the order of the nested cans. Image source: SuperCMDS internal pages.

2.5 The Detector Towers

The detector tower in the superCDMS experiment is the mechanical fixture that provides support for the total mass of the detectors, heat sinking, electrical connection, and it is located inside the innermost can, as depicted in Fig. 2.3. Each tower can fit six detectors and it consists of four thermally isolated stages: LH, ST, CP, and MC with a total height of 190 mm (excluding the stack of detectors), as shown in Fig. 2.4. The tower is designed to be rigidly attached to the cryostat can lid at each stage, and the design of "Wedding-cake" shape was adopted to minimize the passage of infrared black-body radiation from the higher stages to the detectors.

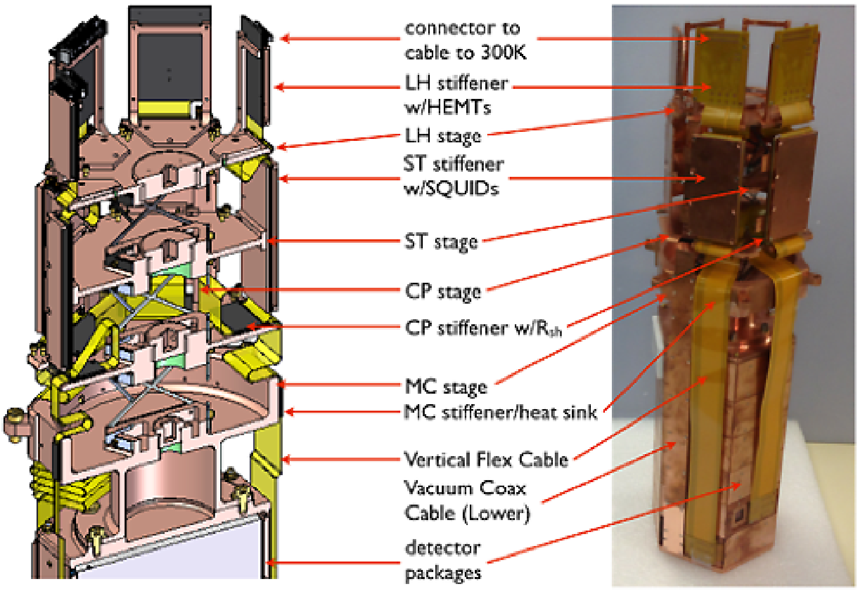

Figure 2.4: The SuperCDMS SNOLAB tower showing the different thermal stages and electrical wiring. Image source: SuperCMDS internal pages.

The readout cables are connected at the 4K stage of the tower and they transfer the signal through the layers of the E-Stem to the Vacuum Interface Board (VIB), located inside the E-tank[1] at room temperature.

2.6 Shielding

It is essential to minimize the environmental background levels at the detectors to prevent any particle which could imitate the WIMP interaction from reaching the detectors. Therefore, the cryostat will be shielded from external radioactivity by surrounding it with three passive shielding layers of:

- Lead: aims to reduce gamma rays and the flux of other particles.
- Polyethylene: aims to reduce the flux of external neutrons by several orders of magnitude at the low energy range.
- Water: aims to reduce the flux of external neutrons, as well.

The layers surrounding the detector have to be made of radiopure material, as depicted in Fig. 2.5. The closer the shielding material to the detectors, the higher the requirement for its radio purity. Furthermore, the copper for the nested cans of the cryostat also needs to be radiopure.

The outermost shielding aims to mitigate the environmental and muon-induced neutrons by about six orders of magnitude, while the inner layer of polyethylene reduces the flux of any neutrons resulting from spallation [69, 70].

In between the two layers of polyethylene, layers of Ultra-Low Background (ULB) and a Low Background (LB) lead will be installed to block external gamma rays. The lead shield consists of interleaved bricks, with a total weight of ∼120 tons, reducing

---

[1] E-tank: is a closed-end, under vacuum vessel attached to the E-Stem at room temperature and provides shielding for the readout electronics.

the gamma flux by five orders of magnitude. The shielding production phase and assembly were completed during summer 2019 at the manufacturing company in France.

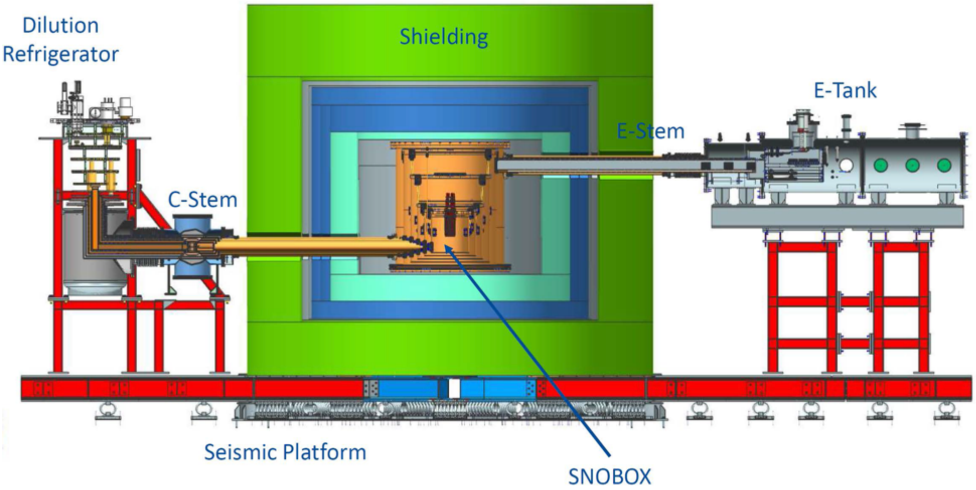

Figure 2.5: A cross-sectional view for the SNOBOX and the surrounding shielding material. Image source: SuperCMDS internal pages.

A radon barrier will be enclosing the lead shielding and the plan is to continuously purge it with nitrogen with low radon activity of ∼50 μBq/m^3 to minimize the background resulting from the radon decay chain.

Eventually, the estimated background at the facility is ∼0.04 (∼0.12) dru (1 daily rate unit: 1 event/kg/day/keV) for silicon (germanium) detectors for energy below 1 keV.

2.7 The Seismic Platform

The seismic platform plays a crucial role in attenuating the impact of local seismic events resulting from the nearby active mine. The design of the platform is based on a spring and bearing system which is able to decouple the base from the horizontal vibrations of the ground.

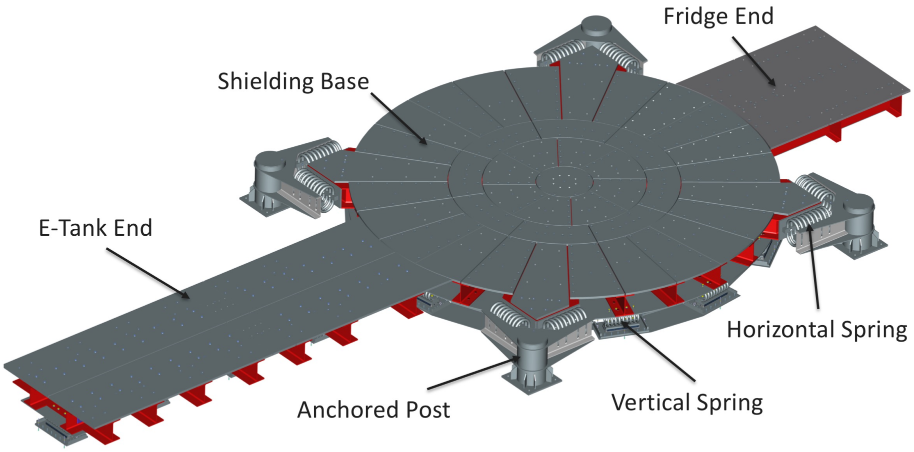

Figure 2.6: The seismic platform is designed to reduce vibrations in the E-tank, fridge and SNOBOX.

2.8 Past Results and Future Goals

The continuous development in all aspects of the CDMS and SuperCDMS experiments led the collaborations to publish competitive exclusion limits (at the time when the results were published) for the WIMP mass parameter space over the past two decades. The CDMS collaboration has utilized a total detector mass of 200 g of silicon and 2 kg of germanium. They reported an upper exclusion limit for the WIMP-nucleon cross-sections larger than $\sigma \approx 3{\times}10^{-42}$ cm^2 for WIMP masses between 10-70 GeV/c^2 [71, 72].

The next generation of the experiment, CDMS-II, has utilized a total of 30 detectors. The experiment was able to set an upper limit on the WIMP-nucleon cross-section of $6.6{\times}10^{-44}$ cm^2 for WIMP mass of 60 GeV/c^2 [73]. Several exclusions limits were released before the high voltage mode of the SuperCDMS, CDMSlite (CDMS low ionization threshold experiment) could achieve $\sim$55 eV threshold energy for electron recoils. The CDMSlite was able to exclude a new parameter space of the WIMP mass $\leq$3 GeV/c^2 [74, 75].

The future SuperCDMS SNOLAB experiment has projected sensitivities for the lower WIMP mass scale, as shown in Fig. 2.7 [76]. In this plot, all curves steeply go up at the lower mass region due to kinematics or detector threshold in the experiments. That is, the lower mass will result in a smaller energy deposition in the detector material, so if the detectors are not sensitive to those small energy depositions, the efficiency to observe such events decreases, which results in increasing the limit. On the other hand, the curves go up at the high mass range due to the decrease in dark matter number density at higher masses.

The yellow shaded region shows the limit where the signal in the detector, will be dominated by the background from interactions with neutrinos for each corresponding mass and cross-section.

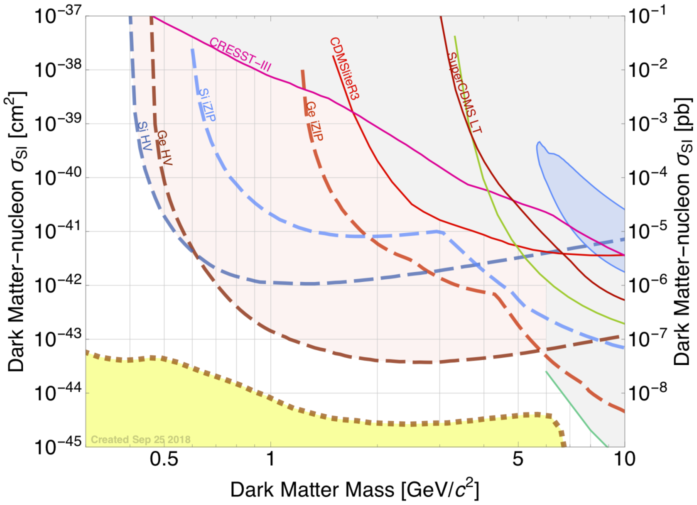

Figure 2.7: The vertical axis is the spin-independent WIMP-nucleon cross-section, and the horizontal axis is the WIMP mass. Exclusion limits from CDMSlite, SuperCDMS LT [57, 77], CRESST-III [78], and Lux [79], all in solid lines. The projected sensitivity for SuperCDMS SNOLAB for all detector types: germanium and silicon both, iZIP, HV are in dashed lines. Image source: [76].

Chapter 3

Future SuperCDMS Detectors

3.1 Introduction

The detectors in the SuperCDMS experiment are classified into two types (HV and iZIP) made from two different materials (germanium and silicon). The different material are essential for several reasons: to break the strong degeneracy in the WIMP mass-cross section plane, to have a better constrains on the WIMP mass which is related to the uncertainty in the WIMP velocity distribution, and to have a better sensitivity for the different possible interaction types.

The detectors are made from cylindrical crystals of the target material, 100 mm in diameter and 33.3 mm thick for a total mass of 1.39 kg for germanium and 0.61 kg for silicon. The detectors are equipped with phonon sensors (both detector types) and charge electrodes (iZIPs only), deposited onto the crystals' top and bottom surfaces.

In this chapter, I will discuss the following: the development of the CDMS detectors, the generation of the phonon and charge signal thorough their circuits, and the characteristics of SNOLAB detectors. I will introduce some measurements used to characterize the sensor performance. Finally, I will go through the different detector calibration methods in SuperCDMS.

3.2 CDMS Detectors

The detectors of the CDMS experiment went through several development stages, but the technology of these ultra-pure germanium and silicon detectors (impurity density of $O\ (10)^{-10}/\mathrm{cm}^3$) has always been the same [80]. The particle interaction with the crystal will cause lattice vibrations, as well as excite electrical charges. The iZIP detectors have the ability to simultaneously measure athermal phonon and charge signals. These measurements of phonon and charge, provide the experiment with a discrimination ability against background particles [81]. A detailed description of the different detector types, in chronological order, can be found in Ref. [82].

3.3 The Phonon Signal

As a phonon calorimeter, SuperCDMS detector is able to measure the total energy deposited after any interaction in the crystal. There are three types of phonons based on the time of creation. Primary phonons: created at the interaction time between the crystal and incoming particles [83]. These phonons have a relatively short mean-free-path $\mathcal{O}(1\text{ mm})$. Ballistic phonons: after some time (few microseconds) the primary phonons undergo a quasi-diffusion process and become ballistic, where the mean-free-path becomes comparable to the detector size (∼1 cm). Ballistic phonons will propagate throughout the crystal and will be collected by the phonon sensors on both detector surfaces. Neganov-Trofimov-Luk (NTL) phonons: generated when detectors are biased at a voltage (V_{bias}). The number of NTL phonons is directly proportional to the bias voltage, as stated in Eqn. 3.1.

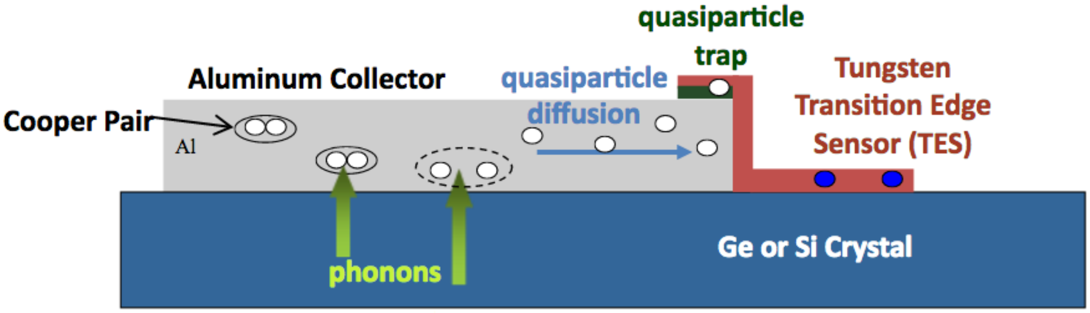

Figure 3.1: A schematic for the phonon collection process through the Al fins, which causes a change in the TES resistance through the diffusion of quasiparticles into the TES. Image source: [84]

The process of phonon collection from the crystal takes place at the Al fins that are attached to a tungsten (W) Transition Edge Sensor (TES), as depicted in Fig. 3.1 [84]. Once the ballistic phonons propagate through the crystal and reach the surface, they move into the Al fins and create quasi-particles by breaking the Cooper Pairs that are naturally present in Al at this temperature. One of the key features of this setup is that the bandgap for the quasi-particles is reduced in the overlap region between the Al and the W (compared to the bandgap in Al). So, when the quasi-particles diffuse to the interface, they can lose some energy and then will be trapped in this region. The only direction they can go is the pure W region, where the bandgap is 0 since the sensor is in transition[1].

During the detector operation, the TES is set to be almost at its critical temperature (T_c). So, any excess heat will cause the resistance of the TES to dramatically change for any slight change in temperature (due to the change in TES state from transition to the normal), as depicted in the left panel of Fig. 3.2. This change in

---

[1] Full details about TES dynamics can be found in Ref. [85].

resistance will result in changing the current which is measured by a Superconducting Quantum Interference Device (SQUID)-base amplifier. The output signal from the feedback circuit will have an amplification proportional to the mutual inductance ratio ($L_{input}/L_{feedback}$) at the SQUID. The phonon readout circuit[2] is shown in the right panel of Fig. 3.2.

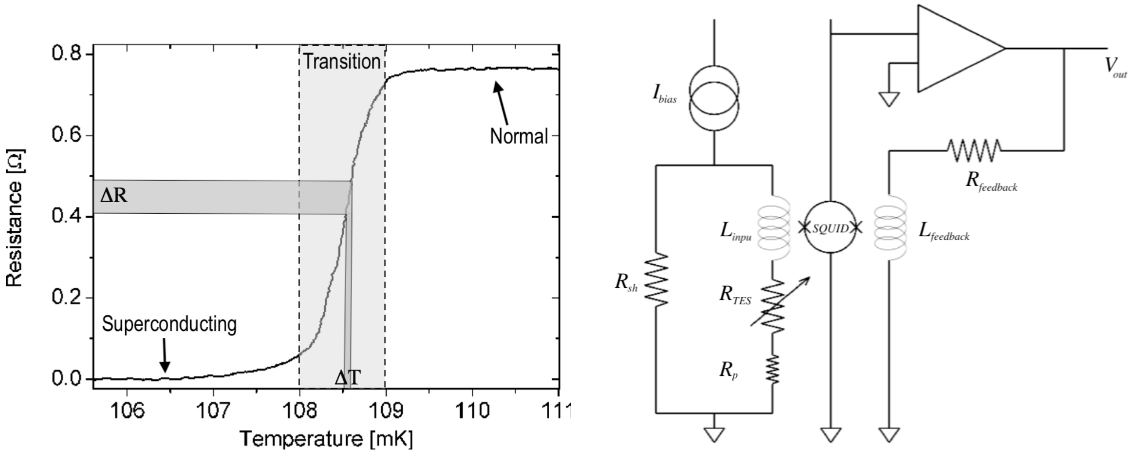

Figure 3.2: *Left*: The TES transition curve. Image annotated from source: [86]. *Right*: The phonon readout circuit. Image source: SuperCDMS internal pages.

NTL Amplification

The SuperCDMS experiment utilizes the NTL effect to achieve low recoil-energy thresholds in the HV detectors. The NTL effect was utilized for the first time in the CDMSlite [66, 87, 88]. In CDMSlite, an energy threshold of 56 $\mathrm{eV_{ee}}$[3] was achieved and it is expected to achieve energy threshold of about 0.6 $\mathrm{eV_{ee}}$ in the future HV detectors.

The NTL effect is exploited to amplify the amplitude of the phonon signal via biasing the detector. The bias voltage will cause the charge carriers to accelerate

---

[2] More details about the phonon electrical circuit can be found in section 2.4.3 of reference [84].

[3] eV_{ee}: 'ee' stands for 'electron equivalent'; this is unit for the energy, reconstructed under the assumption that the primary interaction was an electron recoil.

across the crystal and produce additional phonons which will be collected at the phonon sensors, as depicted in Fig.3.3.

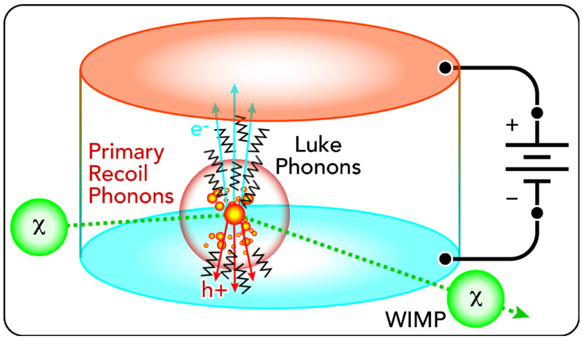

Figure 3.3: A sketch for a biased detector. The Luke phonons are generated and then the work done by the electric field in accelerating the charges (electrons in cyan and holes in red) causes the phonon signal's amplification. So, each number N of e^-/h^+ pairs, will get an addition energy of $N \times \mathrm{V}_{applied}$. The image was modified from the source: [80].

3.4 The Charge Signal

The charge readout circuit is simple compared to the phonon one. The circuit is read out through the High Electron Mobility Transistors (HEMTs) card attached at the 4 K stage of the tower, shown in Fig. 3.4. The key components of this circuit are R_{fb} and C_{fb}, because their value determine the fall time of charge pulses out of the feedback loop which equals to $\sim$40 μs in our circuit. On the other hand, the rising edge of the charge pulses is almost instantaneous because it depends on the digitization rate, which is 0.8 μs per sample.

After an interaction takes place in the detector, the charge carriers will propagate differently within the crystal [89, 90]. Image charges will be collected within nanoseconds at the sensors located at both detector sides, resulting in a pulse out of the feedback amplifier at an amplitude V_o, then the signal is eventually read by the room

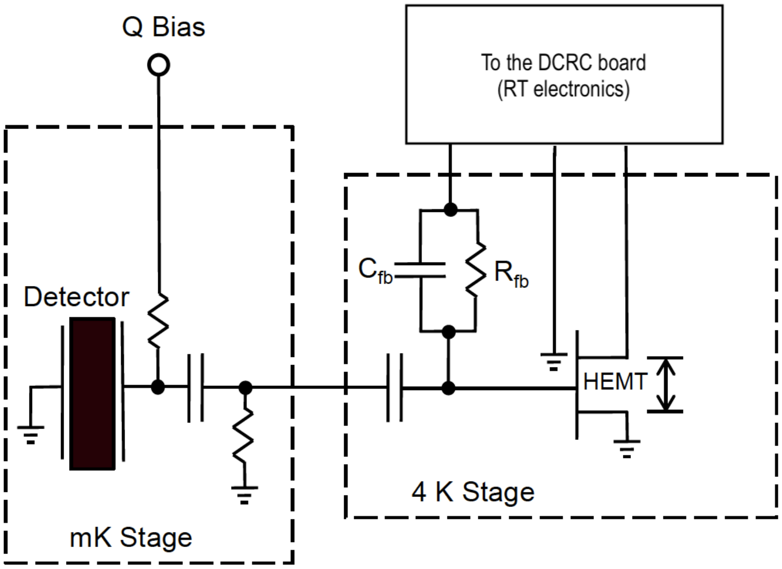

Figure 3.4: The charge circuit block diagram. The dashed line indicated the thermal stage at which the components exist. Image source: SuperCMDS internal pages.

temperature electronics (located at the E-tank).

Over the course of the run, some charges get trapped (at the crystal impurities) during their drift and don't make it all the way to the sensors. So over time, we collect space charges that impact the performance of the detector and reduce the effect of the applied voltage.

To overcome the problem of trapped charges, detectors have to be neutralized. The detector neutralization is performed by flashing the detector with IR photons of energy ∼1.3 eV (940 nm), at high intensity for several hours. The IR photons help to free the trapped charges (or trapping opposite charges) into the crystal impurities. This process will cause the detector to warm up to a few hundred mK, but the base temperature can be easily recovered, and taking data can resume afterward.

The future SNOLAB detectors are aiming to have ionization energy resolution of about 100 eV_{ee} and is dominated by the electronic noise in the ionization readout circuits.

3.5 SuperCDMS SNOLAB Detectors

The SuperCDMS SNOLAB detectors are larger (more than twice the volume) than the previous generation of SuperCDMS detectors with a 30% larger volume-to-surface and a reduced number of sensors per volume (∼2/3) [91]. This results in an increase of over 100% in mass, 75% in surface area, and 50% in the number of phonon sensors. The number of sensors and their layout is selected to optimize the phonon collection efficiency.

The two sensor layouts with complementary technologies to one another provide sensitivity to a lower-energy recoil without being able to discriminate the type of recoil. The first is called interleaved Z-sensitive Ionization and Phonon (iZIP), and the second is High Voltage (HV). The final sensor layouts are depicted in Fig. 3.5.

The adjustment of the TES T_c value is critical in determining the final phonon energy resolution because it scales as T_c^3 [83]. So, to achieve the projected science goals [76], the T_c value for the HV (iZIP) detector should not exceed 45 (60) mK. The projected SNOLAB detector specifications are listed in Table. 3.1.

Detector	Phonon Resolution	T$_c$	Operating Temp.
HV	10 eV	40-45 mK	below 30 mK
iZIP	50 eV	40-60 mK	below 30 mK

Table 3.1: Projected detector specifications and operating temperature at SNOLAB.

The sensors are connected through a Detector Interface Board (DIB) that is mounted inside the detector housing. On each DIB, there are 2 LEDs with an emission peak at 940 nm (∼1.4 eV) used during detector operation to recondition (neutralize) the detector by shining photons at the crystal with enough energy to liberate the trapped charges which have a significant impact on the charge collection efficiency [92].

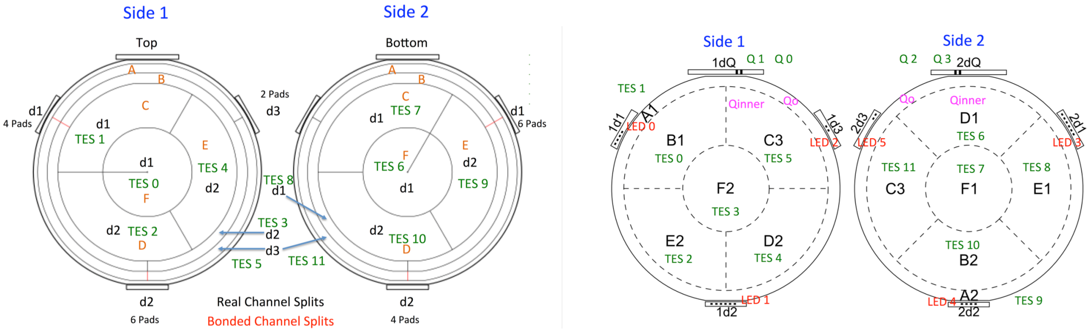

Figure 3.5: The channel layout for SNOLAB germanium detectors. *Left:* HV detector has six phonon sensors on each side. *Right:* iZIP detector has six phonon interleaved with two charge sensors on each side. Image source: N. Kurinksy, SuperCDMS internal documentation

3.5.1 iZIP Detectors

The interleaved six phonon and two charge sensors are photolithographed on both faces (sides) of the detector. For phonon sensing, a tungsten TES coupled with Al fins is being instrumented on each face. The measurement of the charge signal from both sides of the detector is essential for discriminating surface (events occurring at the first ∼2 mm from the surface) from bulk events (events occurring at the bulk of the detector) in addition to estimating the event-depth into the crystal, as shown in the electric field mapping in Fig. 3.6. Using the measured charge signal from both sides of the detector, we can apply a charge-symmetry cut to discriminate bulk from surface events, as shown in the left panel of Fig. 3.7.

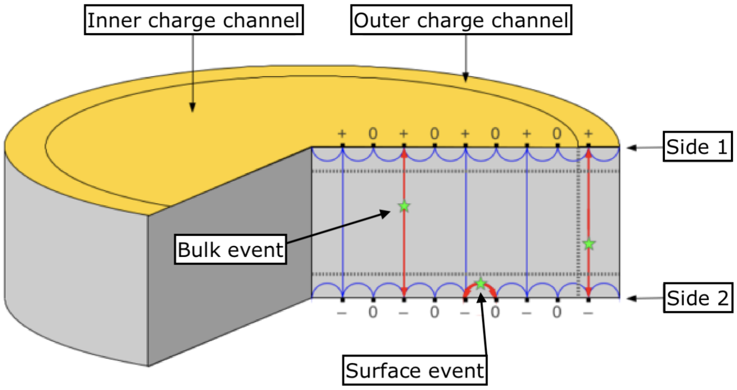

Figure 3.6: A cross-sectional view of the iZIP detector (operated at Soudan). Electric field lines in blue. Charges from a surface event will be collected on one side of the detector, and those from a bulk event will be collected from both surfaces. The image was annotated from the source: [93]

The total measured energy is used to calculate the recoil energy and can be expressed as:

$$E_{total} = E_{recoil} + N_{eh} e V_{bias} \tag{3.1}$$

where E_{recoil} is the energy from initial particle interaction, N_{eh} is the number of e^-/h^+ pairs created in the interaction, e is the elementary charge and V_{bias} is the detector bias voltage.

Another useful physical quantity is the yield, which equals to the ratio between $E_{ionization}$ and E_{recoil}:

$$Y_{ionization} = \frac{E_{ionization}}{E_{recoil}} \tag{3.2}$$

where $E_{ionization}$ is amplitude of the charge signal, calibrated for gamma interaction to give Y value of 1 (for electron recoils). To find the recoil energy we can use:

$$E_{recoil} = \frac{E_{total}}{1 + Y_{ionization} \times (\frac{eV_{bias}}{\epsilon})} \tag{3.3}$$

where ϵ is the average energy required to produce one e^-/h^+ pair. For germanium (silicon) this will be about 3 eV (3.8 eV) [94, 95], at SuperCDMS operating temperature.

In the case of germanium detectors, nuclear recoils (NR) produce about 1/3 ($\epsilon = 3\ eV$) the ionization energy as electron recoils (ER) of the same energy electron recoils. The yield as a function of energy is well described by the Lindnard theory [96], at energies above ∼40 eV for silicon [76]; but for lower energies, the yield is not well-known, and it is part of the supplemental research program of SuperCDMS to measure this value for germanium.

The difference between ER and NR creates a separation between the two energy bands when plotted against the recoil energy, as depicted in the right panel of Fig. 3.7 (taken for the old SuperCDMS detectors). In this figure, the area with green lines is $\pm 2\sigma$ for the neutron-ionization yield. The black vertical line is the recoil energy threshold (analysis threshold), and the hyperbolic line is the ionization threshold.

The SNOLAB iZIP detectors are aiming to be sensitive to an extremely low nuclear recoil energy. Hence, the discrimination is expected to be much better, with the ability to set the analysis threshold at about 1 keV [91].

3.5.2 HV Detectors

The SNOLAB HV detectors will have an optimized sensor geometry for a good ability to collect phonons from both sides of the detector. This is accomplished by utilizing the NTL amplification and will improve the phonon resolution to about 10 eV_t. On

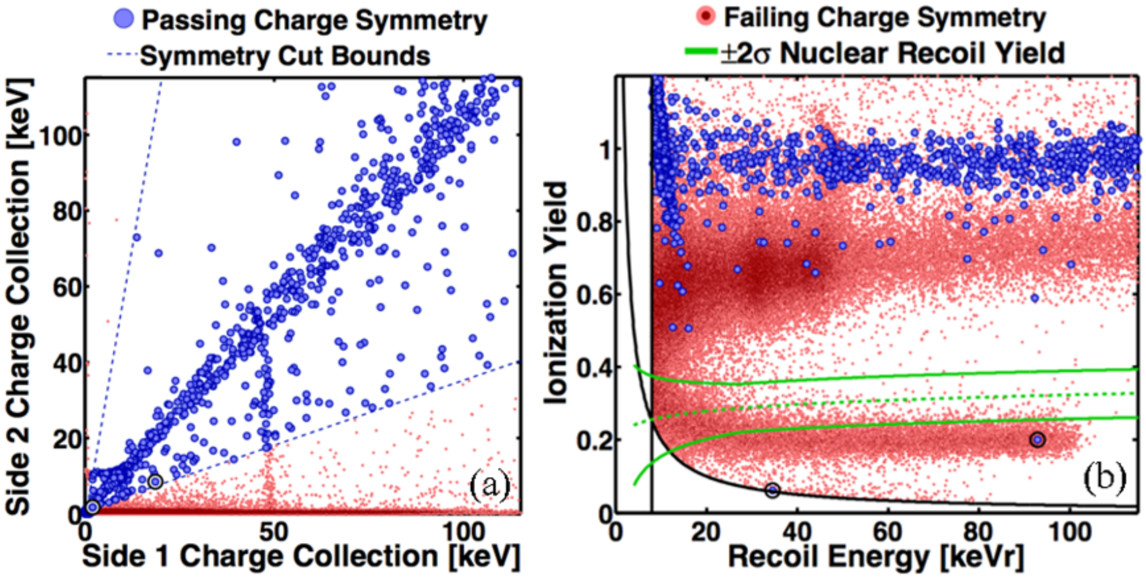

Figure 3.7: *Left:* Data from an iZIP detector irradiate on side 1 by a 210Pb source. The events highlighted in red are excluded. The 46.5 keV gamma line from the 210Pb decay is clearly visible on side 1. *Right:*. The normalized ionization yield is a function of recoil energy. The data was acquired by a ^{210}Pb source. All surface background events with a yield in the range where bulk nuclear recoils are expected are effectively removed by the surface event cut. Image source: [97]

the other hand, we lose sensitivity to the primary phonon signal (since it is now overwhelmed by the NTL signal) and thus, the ability to discriminate ER from NR background on an event-by-event basis.

The design of HV detectors, shown in Fig. 3.8, is focusing on maximizing the TES sensitivity because these detectors are not able to measure electric charges. Moreover, the design aims to have a better position reconstruction, and event fiducialization to optimize the ability of phonon-only measurement in reducing backgrounds.

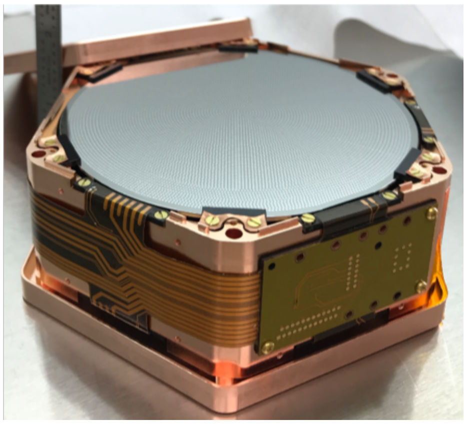

Figure 3.8: The 100 mm, HV SuperCDMS SNOLAB prototype detector.

3.6 HVeV Detectors

The High Voltage eV resolution (HVeV) detector is a gram-scale phonon sensing Si detector (a Ge version is planned for the future), developed by members of the SuperCDMS collaboration to perform nuclear recoil ionization yield measurements. Small detectors are required to achieve a good energy resolution and to minimize the rate of multiple scatters which would make the interpretation of the yield measurement difficult. These detectors were then also utilized to investigate leakage current, impact ionization[4] and charge trapping[5]. [98].

The top side of the detector is patterned with quasiparticle-trap-assisted electro-thermal-feedback transition-edge sensors (QETs). As the name suggests, the detector is operated at high voltage, to utilize the NTL effect [99], by applying a bias voltage between both faces of the detector.

---

[4] *Impact ionization*: a charge drifted through the detector by the electric field can liberate a second charge carrier originally trapped at an impurity or lattice defect, leading to an increased NTL effect.

[5] *Charge trapping*: a charge drifting through the detector can get trapped by an impurity or lattice defect, leading to a reduced charge collection and a lower NTL amplification.

Currently, the HVeV detectors are being calibrated via a laser source. This calibration technique requires the use of an optical fiber to transmit the photons from the laser to the detector. There are several attempts to find alternative calibration techniques at cryogenic temperature without the need for the installation of an optical fiber (because it is not an option for the experiment at SNOLAB due to the need for making additional holes in the shielding, which will increase the background levels at the detectors) such as the one mention in Chapter. 5 of this dissertation and in Ref. [100].

3.7 Sensor Characterization

To evaluate the detectors' performance, there are several measurements that have to be done prior to cooling down such as: the continuity check at several phases of the installation process, to evaluate the detector's operational channels and readability for the installation. On the other hand, some other measurements have to be performed to optimize the operational settings, detect failure modes, and to estimate the expected energy resolution. In this section, I will give an overview of two key measurements that has a significant role in evaluating the detector's performance.

3.7.1 IbIs Measurement

We define the current that goes into the phonon circuit and adjusted by the DCRC[6] board as I_b (bias current), and the current passing through the sensor as I_s, as shown in the circuit diagram of Fig. 3.2. The measurement of $I_b I_s$ can tell us about the best bias point for a given temperature, so we can select at what point in the transition

---

[6] Digital Control and Readout Card (DCRC): a customized electronic board for SuperCDMS used in data acquisition.

state the TES needs to be.

Here, R_p is the parasitic resistance, and R_n is the normal resistance (the value of the sensor resistance, $\mathrm{R_{TES}}$ when it goes into the normal state). Finally, R_{sh} is the shunt resistor shown (earlier) in the circuit diagram, in the right panel of Fig. 3.2. Moreover, this measurement is also used to find the values of the parasitic resistance, R_p and the normal resistance of the sensor, R_n (this is the value of the sensor resistance, $\mathrm{R_{TES}}$ when the sensor goes into the normal conducting state), by simply taking two points at very low and very high current values, respectively.

The measurement is performed by ramping up the current, to eventually force the TES into transition by the current, rather than by heat. The high current will increase the kinetic energy of the Cooper pairs, and if the kinetic energy is at or above the superconducting band gap, we can break the pairs, which will lead to a finite resistance, as shown in Fig. 3.9. The finite current and resistance will produce heat. This contributes to the measured increase in resistance (and leads to a hysteresis when ramping the current up and down).

When the bias current (I_b) is small, the TES sample remains superconducting due to the insufficient heat to change its state. In this case, all the current passing through the TES will be equivalent to (I_b) and we can determine the value of R_p, if R_{sh} is known from eqn. 3.4 (note: when the current is small, $\mathrm{R}_{TES} = 0$).

Once the current increases, the TES sample starts to be in transition, and it starts to have some measurable resistance, similar to the region I at the left of the dashed line in Fig. 3.9. Finally, if the current is high enough, the TES sample becomes warm enough (in normal mode, as in region II), and the value of R_{sh} can be used to calculate the value of R_n using eqn. 3.4.

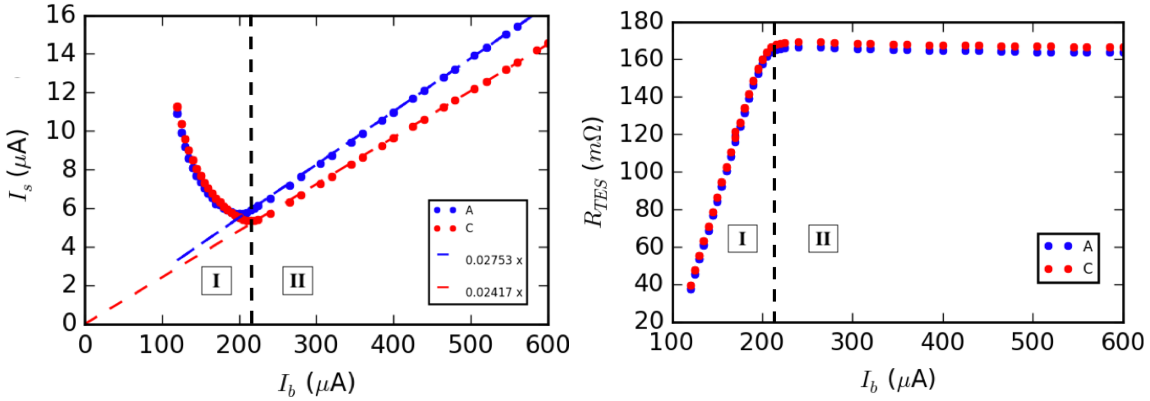

Figure 3.9: *Left*: Current through the TES (I_s) plotted versus a changing bias current (I_b) for two sensors, A and C. The region to the right of the dashed line is where the sensor reaches the normal state. *Right*: Resistance measurement from the I_bI_s curve. Image source: [85]

$$R_p + R_{TES} = (\frac{I_b - I_s}{I_s})R_{sh} \tag{3.4}$$

3.7.2 Tc Measurement

This is a fundamental measurement for the functionality of the phonon channels for two reasons: first, the T_c value needs to be in a range well above the fridge base temperature to enable a reliable detector operation, and second, the phonon energy resolution scales with the third power of T_c.

This measurement can be performed by slowly ramping up (or down) the fridge base temperature while measuring the TES resistance.

The only drawback in this method would be, the required thermalization time which greatly impacts the precision of the measurement.

3.8 Detector Calibration

Detector calibration is necessary to quantify the amounts of energy deposited into the detector and to be able to interpret the collected data. Calibration measurements have to be repeated on a regular basis to monitor the gain stability of the detectors.

In the previous generation of the SuperCDMS experiment at Soudan, large data sets with a variety of calibrations methods (neutron and gamma) have enabled the process of data selection to be finely tuned for a precise measurement of signal efficiencies.

3.8.1 Calibration using Gamma Source

Gamma sources of energy range of a few hundred keV, were utilized in the SuperCDMS experiment at Soudan, for calibrations in the germanium detectors.

On one side, the use of similar sources will be hard to employ at the new experiment at SNOLAB due to the many shielding layers around the cryostat. On the other side, the new detectors will have to be calibrated at a lower energy range, because the new experiment is designed to have much lower energy thresholds (compared to SuperCDMS, Soudan). An example of gamma photons emitted from the decay of a ^{133}Ba source for data taken at Soudan is shown in Fig. 3.10.

Another gamma source we use for calibration purposes is the ^{241}Am, with a half-life time of $\sim$432 years. The ^{241}Am emits an intense gamma-ray at 59.5 keV [101]. These gamma rays can be easily shielded and hence, this source can only be used at the surface test facilities, where the source can be installed near the detector.

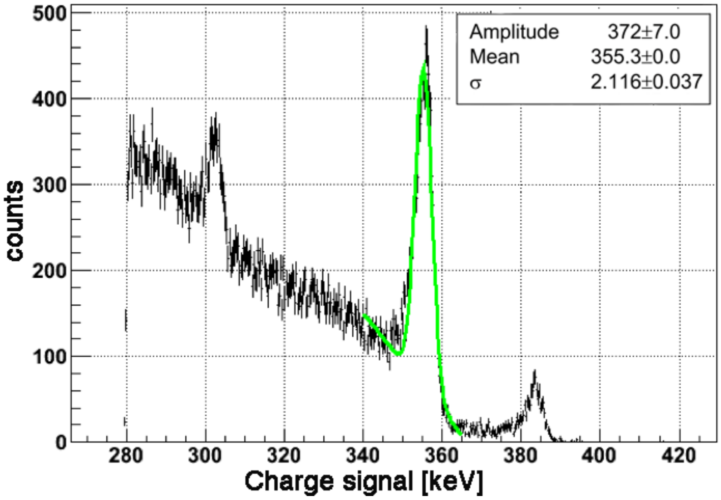

Figure 3.10: Spectrum of ^{133}Ba source used in SuperCDMS Soudan. It provides gamma lines at 303, 356 and 384 keV.

3.8.2 Calibration using Neutron Source

Neutrons in the MeV energy range will cause elastic scattering interaction with the target nuclei and as such, mimic dark matter interactions. Data from a neutron calibration, where the neutrons came from a ^{252}Cf source (plot from the SuperCDMS experiment), is shown in Fig. 3.11 [102]. The SuperCDMS experiment at Soudan had a guide tube along the E-stem and another one along the C-stem to deploy the source during the calibration periods.

The source deployment at SNOLAB will be the same as the former experiment. This approach aims to minimize the exposure of the detectors to external radioactive sources, and other approaches would require a much more complex design to introduce holes at shielding material surrounding the cryostat.

Germanium detectors can be activated by neutrons through the production of ^{71}Ge. This isotope decays by electron capture (EC), generating spectral lines at

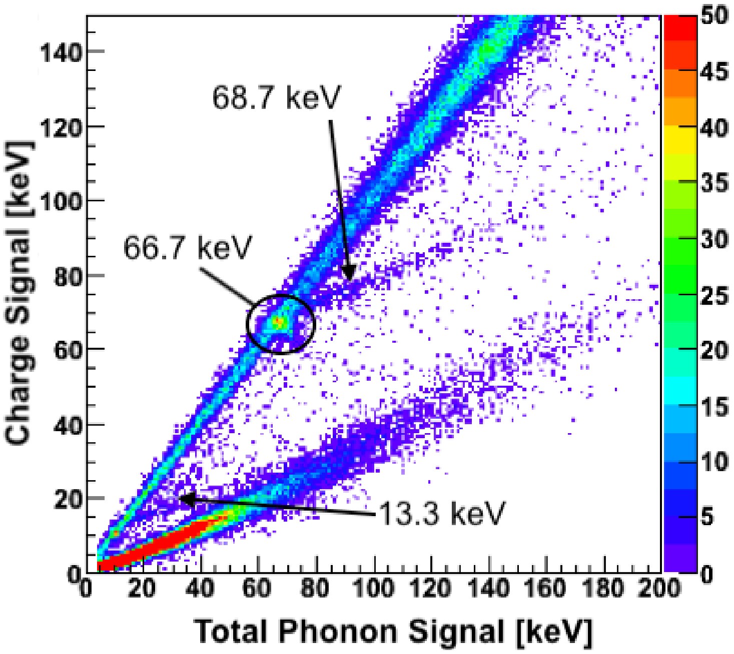

Figure 3.11: The charge vs. the phonon signal showing ER events populate the upper diagonal. The bottom band is NR events and the two bands coming out of the gamma band (diagonal) at 13.3 and 67 keV are from inelastic nuclear interactions. This data is taken from the ^{252}Cf source while being used in SuperCDMS Soudan. Figure produced from SuperCDMS Soudan neutron calibration data by Lauren Hsu [102].

10.37, 1.30, and 0.16 keV for K-, L- and M-shell captures respectively, as shown in Fig. 3.12. These peaks are suitable to calibrate the SuperCDMS SNOLAB germanium detectors because they are within our energy range of interest for low-mass dark matter detection. And they were previously used in the CDMSlite. The disadvantage of this method is that it will have a relatively long-term effect on detectors. The effect results when the Ge crystal gets activated by the neutrons and the activation decays with a half-life of ∼11 days [103]. For this reason, the former experiment at Soudan has performed the neutron calibration every few months.

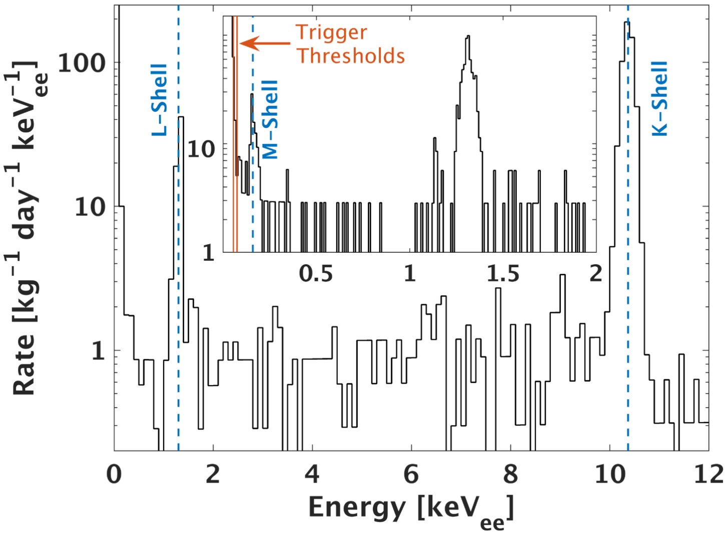

Figure 3.12: The EC decay spectrum from ^{71}Ge. The blue dashed lines correspond to the K, M & L shells at 10.37 1.3 & 0.16 keV$_{ee}$ from CDMSlite run 3 data. Image source: [66]

3.9 Conclusion and Future Work

The new generation of SuperCDMS detectors was developed to meet the future science goals of the experiment at SNOLAB [76]. Extensive studies were performed and several proposals were made for the phonon sensor layout to optimize the phonon collection efficiency and energy resolution.

Several measurements are necessary to determine each detector's physical parameters and most of these measurements are currently either automated or automation is still under development to be ready for the experiment operation at SNOLAB.

Radioactive sources are necessary for calibration of the energy scale, monitoring stability, and (in iZIP detectors) to determine the nuclear recoil yield band. The utilization of a neutron source is required for the latter and useful for the calibration of Ge detectors at low energy, but it also contributes to the background for the dark matter search. A scheme for the use of the neutron source needs to be developed that balances the benefits against the increase in the background.

On the other hand, the utilization of a neutron source in a Si detector is not possible because there are no internal activation lines. Therefore, we need ways to confirm the low-energy response of our silicon detectors. We have started, and we are currently still developing new methods that can be applied in-situ and without hardware upgrades as will be discussed in Chapter 5 of this dissertation.

Chapter 4

Cryogenic Underground TEst (CUTE) Facility

4.1 Introduction

The CUTE facility is currently located at SNOLAB near Sudbury, ON. While awaiting the delivery of the new SuperCDMS detectors, CUTE is operating a variety of devices to commission and characterize the facility. The background level between 15 and 50 keV was recently measured to be about 7 dru. At lower energies, the measured background is believed to be limited by the detectors used.

This chapter will give an overview of the CUTE facility and its subsystems. I will also be listing the major goals of each measurement, detectors, and apparatus used for a series of measurements performed while the cryostat on the surface, at Queen's Test Facility, and underground at SNOLAB, in addition to a summary of results. CUTE is the facility for many proposed tests suggested in this dissertation. Moreover, many preliminary noise studies reported in this chapter are essential for a full detector operation that is required by the tests suggested in Chapter 5. Finally, I will suggest future measurements to further understand the CUTE environmental noise.

4.2 CUTE Facility - Overview

The dilution refrigerator is surrounded by several shielding layers: a 3 m diameter water tank, two layers of lead and covered by ∼20 cm of Polyethylene shield, and a cylindrical block of lead fixed inside the fridge, at the Still stage (above the detector's location) to minimize the background level at the detectors.

The CUTE facility, shown in Fig. 4.1, has a dry dilution refrigerator (from CryoConcept) that is designed to reach a base temperature of ∼10 mK. The cooling power is provided by a two-stage Pulse Tube (PT) cryo-compressor. The dilution refrigerator has several isolated thermal stages starting from room temperature, 60 K, 4 K, Still (ST), Cold Plate (CP), and finally the Mixing Chamber (MC). When the cooling process starts, the PT cooling power is expended to cool down the 60 and 4 K stages and is able to bring the temperature of the three lower stages (ST, CP, and MC) down to ∼4 K through circulating a mixture of ^{3}He and ^{4}He gas in fast circulation pipes called, the fast injection and pumping lines.

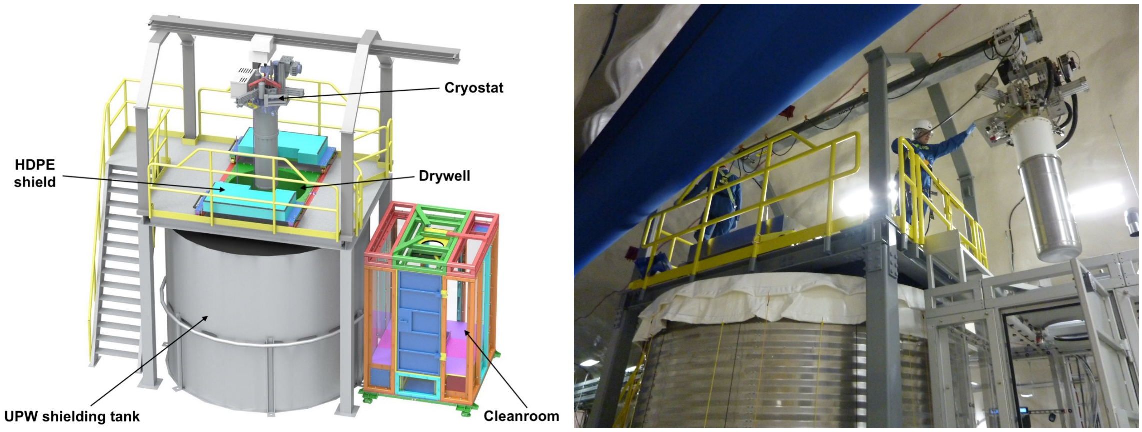

Figure 4.1: *Left*: CUTE Facility at SNOLAB showing major sections. *Right*: The actual facility while transferring the cryostat from the Drywell to the clean room for a payload change.

.

Once the MC temperature reaches ∼4 K, the fridge is automated to collect the gas from circulation lines back into the mixture tank, then to start the condensation process. The condensation includes other peripheral components such as the roughing pump, compressor (which are the major components of the Gas Handling System (GHS), shown in Fig. 4.2) and the condensation process finally engages the mixture turbopump to maintain the flow rate of the mixture at the fridge's operational values.

When the concentration of the ^{3}He inside the mixing chamber reaches about 67% at ∼8450 mK (the Lambada point), the phase separation process occurs [104]. The denser phase (^{4}He) is separated from the less dense phase (^{3}He) by gravity. The difference in the enthalpy between the two phases keeps the diffusion of ^{3}He from the concentrated to the diluted phase. This increases the entropy and heat are absorbed from the surrounding. Afterward, the ^{3}He diffuses back through the counter flow heat exchangers, which cools down the incoming gas and vaporizes it as it reaches the Still stage. The dilution refrigerator's pumps at room temperature keep the pressure at the Still stage low enough for the process to continue.

4.3 Facility Subsystems

Several subsystems are required to work in parallel for the full operation of the facility. In this section, I will be listing the facility's major subsystems along with a brief description.

4.3.1 The Chiller

The water chiller from LYTRON, model RC095 is a manually controlled, water-cooling device, with operating temperature set at 9° C used to provide the cooling power for the Helium Pulse Tube Cryo-compressor.

4.3.2 Pulse Tube Cryo-compressor

The Pulse Tube Compressor from CryoMech is a standard two-stage, closed-loop He expansion cooler, with a cold head (the expansion device), and has a cooling power of ∼25 W at the 60 K stage and ∼2 W at the 4 K stage.

4.3.3 Gas Handling System (GHS)

The GHS is an aluminum cart that includes the following units:

- Control units of the pneumatic valves
- The ^{3}He and ^{4}He mixture tank

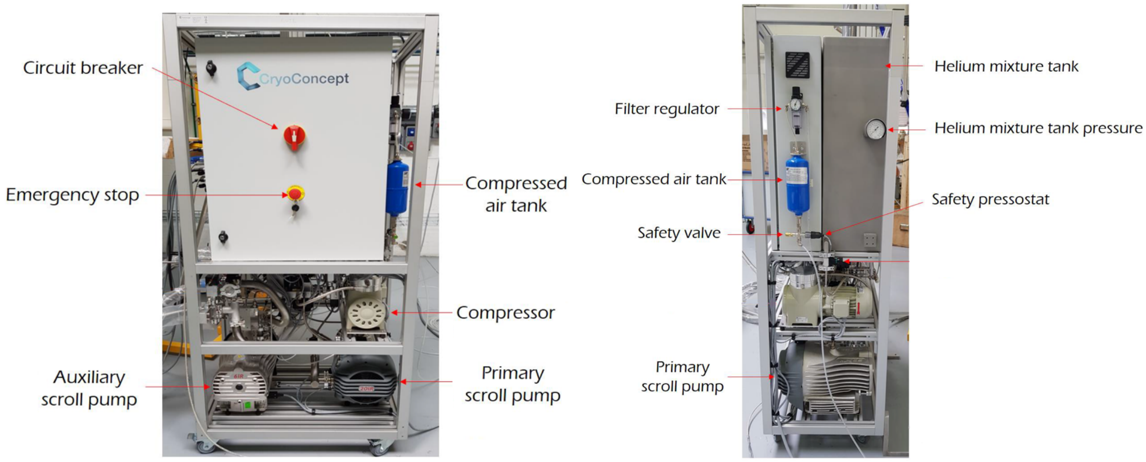

Figure 4.2: *Left*: A front view for the GHS showing the major components. *Right*: A side view to show the He mixture tank.

.

- Primary scroll pump (nXDS20iR): it maintains the necessary mixture flow for a proper fridge operation

- Auxiliary scroll pump (nXDS6iR): used to pump on the OVC[1] and can bring the pressure down to $\mathcal{O}(10^{-2})$ mbar, before the OVC turbopump (directly attached at the fridge) can engage
- Compressor: attached to the mixture line and it only runs when needed to control the mixture flow. In normal operating conditions, the pump will be by-passed to reduce vibrations in the GHS
- Compressed air tank: a back-up air tank to be able to control the pneumatic valves in the case of any power outage. The capacity of the tank is enough to bring the fridge back into a safe state (where the mixture is safely stored back in the tank)

4.3.4 Suspension System

The cryostat is designed to be mechanically and electrically decoupled from the PT cold head, which makes the cryostat floating while it is in operations (to reduce vibrational noise). The cryostat is designed to be mechanically and electrically decoupled from the PT cold head balanced between soft bellows under vacuum holding it from the top and polymer dampers underneath, to reduce vibrational and electrical noise. This design makes the cryostat susceptible to varying air pressure at the SNOLAB facility. If unmitigated, pressure changes lead to a change in cryostat position which affects the temperatures inside the cryostat, and thus the detector response, and if the maximum range of the bellows or the dampers is reached, it would not be decoupled anymore. Therefore, the dampers are mounted on movable stages to maintain a fixed vertical position for the cryostat.

---

[1] Outer Vacuum Can (OVC): is the vacuum-tight outermost can of the cryostat.

In fig. 4.3, we show the three supporting beams which rest on three movable lab jacks, driven by three stepper motors and controlled by an optical sensor.

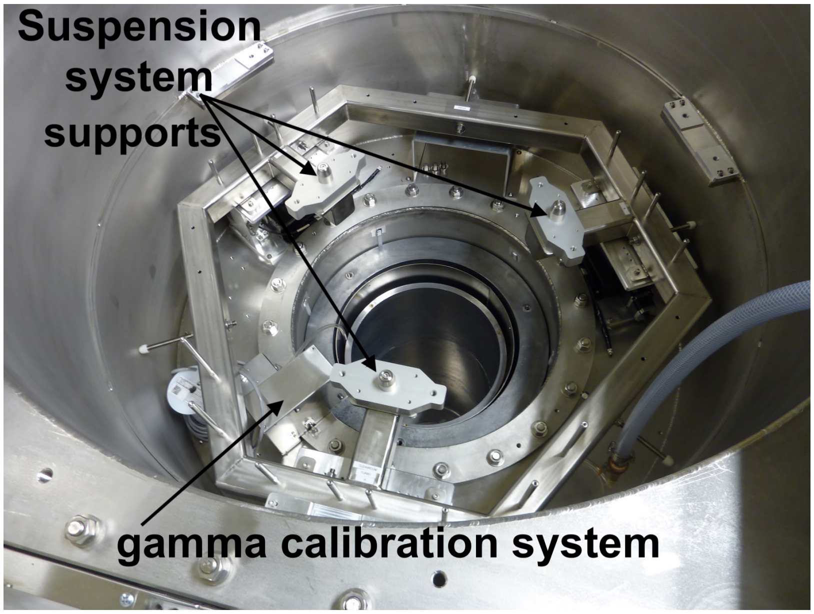

Figure 4.3: An overview on the drywell at the CUTE facility, showing the suspension system hex beam resting on three lab jacks. The arrows are pointing at the support beams where the dilution refrigerator is mounted.

.

4.3.5 Slow Control

The slow control rack contains several components: the main power supply for the rack, control unit of gamma and neutron calibration systems, an Ethernet switch, the fridge thermometry control units, the suspension system analog sensor box, the Peltier cooler power unit, and the lab jack power supply.

4.3.6 Purge Gas

The compressed air system is utilized at the CUTE facility in two areas: First, inside the cleanroom, where the work on detectors and payload change is performed. Second, inside the drywell, where lead is used to shield the fridge.

The SNOLAB environment has a challenging radon concentration of ∼130 Bq/m^3, to mitigate this high concentration, the space between the cryostat and external lead is continuously flushed with pressurized air from the surface with a lower radon concentration of ∼3 Bq/m^3.

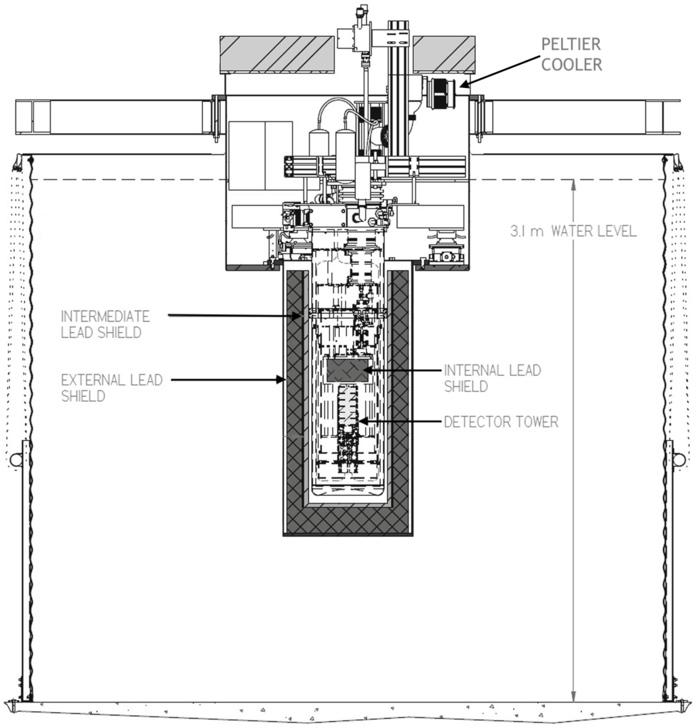

Figure 4.4: A sketch for the fridge layout showing the different layers of shielding lead, the location of the cryostat in the drywell and surrounding water tank (modified from [105]).

.

4.3.7 Calibration Systems

The calibration systems at the CUTE facility are divided into two types: gamma and neutron calibration. See section 3.8 of this dissertation for more details about the use of calibration sources in the experiment. Currently, the neutron calibration system is still under development while the gamma calibration system is fully deployed and functional.

The gamma source at the CUTE facility, ^{133}Ba, is always kept at the storage position, as long as the measurements do not require a calibration source. When deployed, a stepper motor will be remotely controlled, and gravity will pull the source down through the guiding copper tube between the OVC and the internal layer of lead, as depicted in Fig. 4.5.

4.4 Special Noise Sources of the CUTE Facility

Due to the complexity of our facility, there are many possible sources of noise. These sources can be classified into either mechanical (vibrations) or electrical sources (which can add current noise to the TES readout circuit). In this section, I will be focusing on the sources we found - so far - at CUTE to finally be able to optimize the fridge performance and start taking science data using the new generation of detectors.

4.4.1 Pulse Tube Vibrations

The vibrations from the Pulse Tube (PT) cryo-compressor are transmitted through the hoses and cause the fridge to vibrate at a low frequency. This is noted by the rise in current noise at the low-frequency range when comparing the PT-on with PT-off data.

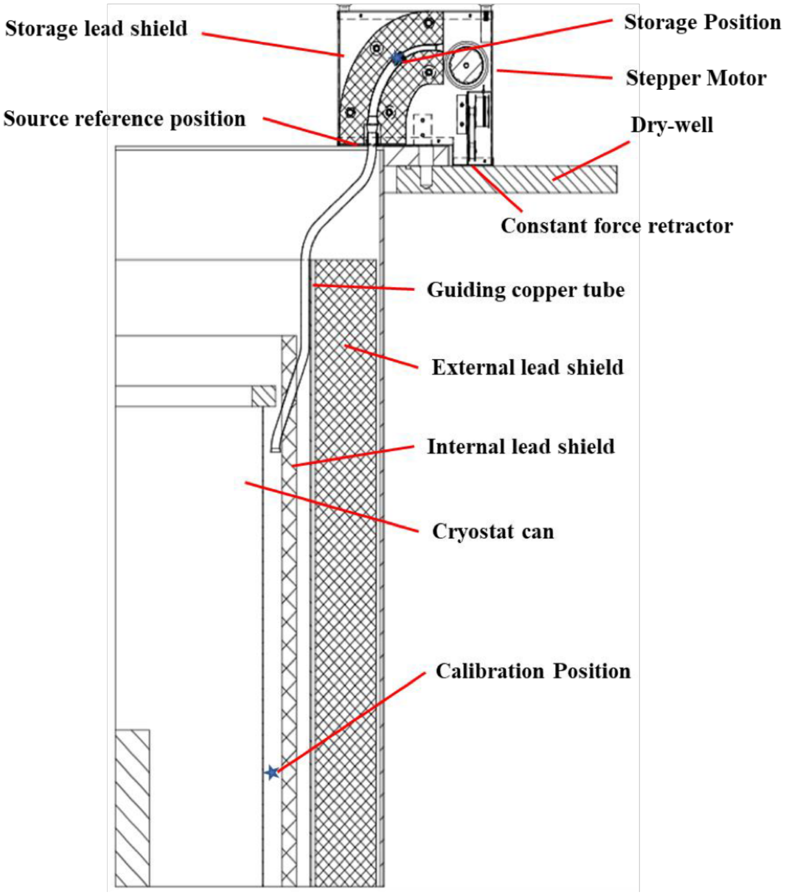

Figure 4.5: Cross-sectional view of the gamma calibration system at CUTE facility.

.

To investigate the PT effect, initial noise measurements started while the cryostat being coupled to the chassis, afterwards, the suspension system was activated, which allowed improving the noise levels at low frequencies, as will be shown in the following sections.

4.4.2 Purge Gas Vibrations

The flow of pressurized air around the cryostat is causing significant vibrations, which in turn increases the noise level in the detectors. Measurements of such vibrations, taken with an accelerometer mounted at the top of the cryostat are depicted in Fig. 4.6. The accelerometer setup (hardware and software) was developed and operated by R. Germond.

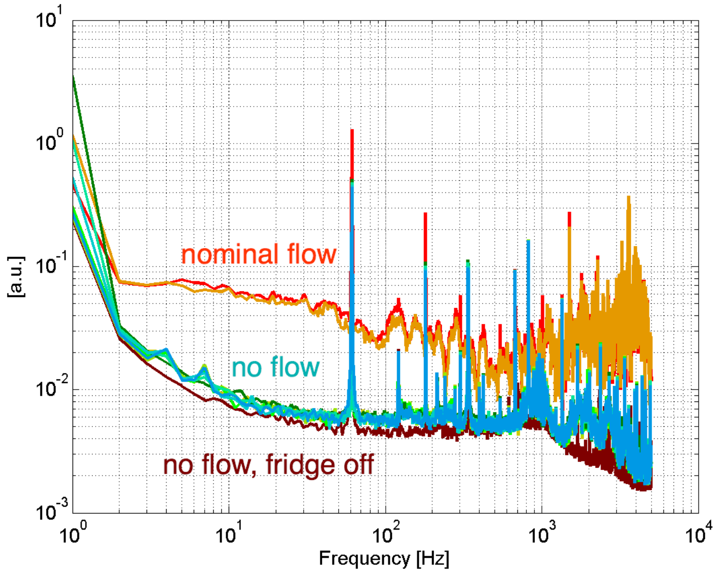

Figure 4.6: A noise PSD from accelerometer data at different purge-gas flow rates. The nominal flow was achieved by tuning the pressurized gas valve to a point where no more airflow can be audible.

.

The calibration of the pressurized airflow is still under study and currently, the plan is to introduce an additional flow meter to improve the estimate of our flow measurements to finally optimize a nominal flow rate with the noise level in our detectors.

4.4.3 Other Noise Sources

The slow control rack at CUTE contains several control units, as discussed earlier. Some of these units were found to induce significant noise into our signal. One example is the controller for the Peltier cooler which is used to cool the mixture turbo-pump and is attached to the pump at the top of the cryostat, as indicated in Fig. 4.4. The controller switches a high-current power line at a rate of 338 Hz, which generates electromagnetic interference that is picked up by our detector readout electronics.

4.5 Deployment of the Soudan Tower

The dilution refrigerator for CUTE was initially delivered and tested at Queen's Test Facility (QTF), where several cryogenic tests took place during the period Dec 2017 - May 2018 to optimize the temperature of the mixing chamber to ∼11.5 mK by adjusting the ratio of ^{3}He to ^{4}He in the mixture lines. In addition, we designed and produced various parts to be able to fit the former SuperCDMS tower and detectors. In Fig. 4.7, I show a road map for the tests performed in each detector at QTF.

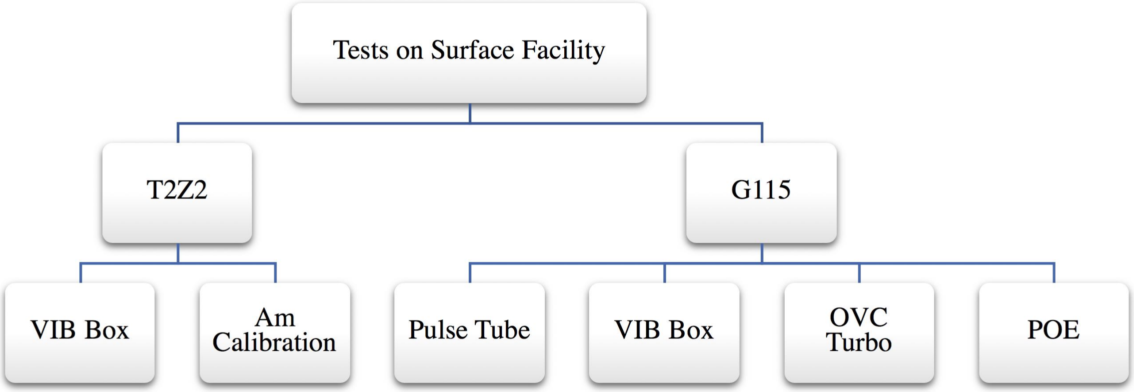

Figure 4.7: A diagram for the tests performed at QTF. The second level of the diagram is the detector name and the third is the study type.

4.6 Experimental Setup: T2Z2

The first run for the dilution refrigerator on the surface had several goals such as measuring the transition temperature (T_c) for the phonon sensors of a 3-inch germanium detector (T2Z2), and for a set of TES samples (ZB1T-19), shown in Fig. 4.8. The TES chips were produced at SLAC and measured at Stanford before being sent to Queen's for comparison. In this run, we had connection problems with the TES samples and hence could not use them for these tests. A summary of the previous T_c measurements is listed in Appendix. A.

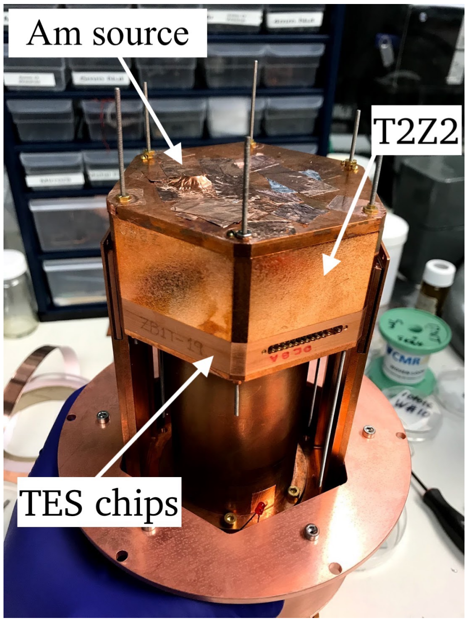

Figure 4.8: Soudan-type tower holding T2Z2 (Ge detector) at the top of a 1 cm housing containing 8 TES samples.

To be able to reach optimal noise levels, we used the latest DCRC board available at that time (Rev.D, SN11 - which was modified by Tsuguo Aramaki to reduce the telegraph noise). To calibrate the energy scale, an ^{241}Am source was installed at the detector's top lid to shine at the top of the surface of the detector.

4.7 Tower Adaptation

Major parts have been purchased or designed, then produced to be able to fit the tower and to heat-sink it at the different thermal stages of the dilution refrigerator as detailed below:

- 4K heat-strap: an OFHC that is 10-inch long and 1-inch wide, to thermally heat-sink the 4K stage of the tower to the 4K can, as shown in Fig. 4.9.

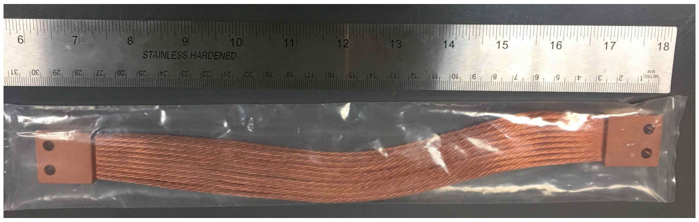

Figure 4.9: 4K Heat strap

- CP heat-strap: connected between the CP rod and CP stage of the tower, shown in Fig. 4.10.

Figure 4.10: Cold Plate heat strap

- MC adapters: Top adapter, is used to hold the tower to the MC plate. The bottom adapter is used to hold the MC stage of the tower to the MC tube. MC tube is used to connect the pieces together while forming an IR tight environment to the detectors. The MC adapters are shown in Fig. 4.11.

Figure 4.11: Left to right: MC top adapter, bottom adapter and tube.

- Tower IR shield: used to optically isolate and to block any IR radiation, might be coming from the higher thermal stages, from reaching the detector stack. The tower shield is shown in Fig. 4.12.

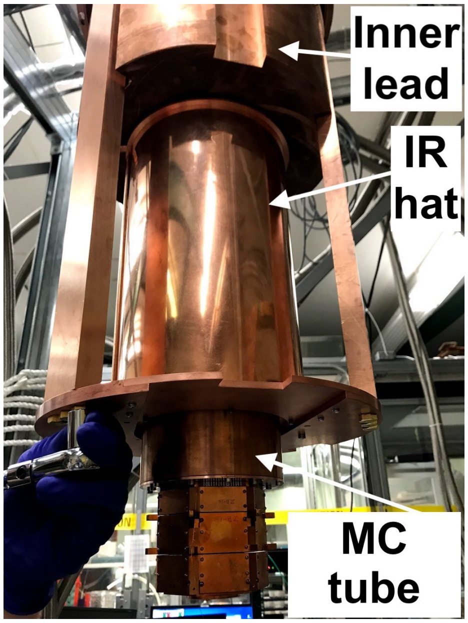

Figure 4.12: The tower IR shield after being attached to the MC plate.

- Still adapter: designed to be IR tight to block any IR radiation from the 4K stage from reaching the detectors, and to thermally connect the Still stage of the tower with the Still membrane, as shown in the left panel in Fig. 4.13.

- Still membrane: used to thermally link the Still stage of the tower to the Still can and to block IR radiation from the 4K stage, as shown in the right panel in Fig. 4.13.

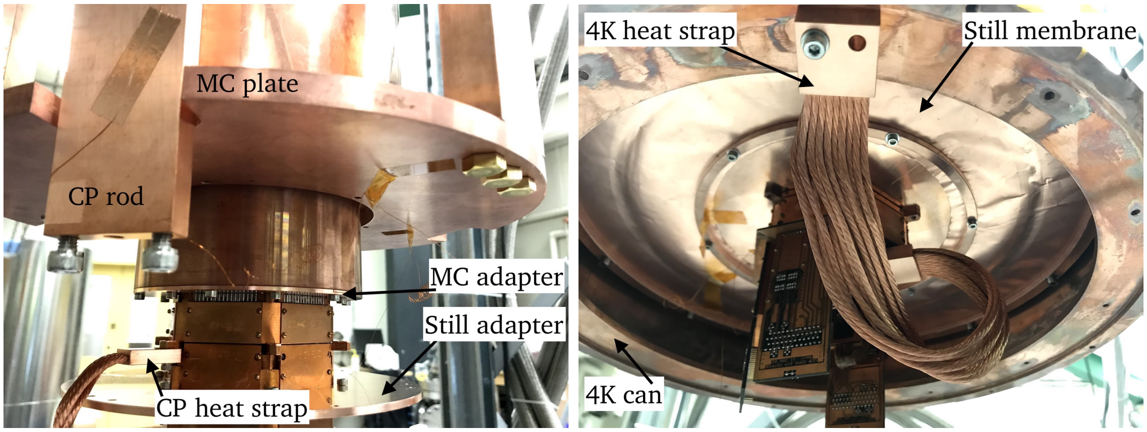

Figure 4.13: *Left*: Soudan tower post-installation at CUTE for the first time. *Right*: The bottom of the tower showing the Still membrane and 4K heat-sink after being attached to the 4K can.

Additional necessary parts and systems were also produced and installed at different times during the installation process, such as the Vacuum Interface Board (VIB) box, Stripline-to-100 pin adapter (to be able to connect the Striplines to the VIB), and pi filters (with a cut-off at 3.2 MHz). However, the calibration and suspension systems in addition to some other peripherals devices were installed only after the fridge has moved to SNOLAB. Fig. 4.14 shows the full dilution refrigerator, before adding the cans, after a successful and full implementation of the Soudan tower at QTF.

4.8 Noise Studies Using Detector T2Z2

Studying noise sources is important in our data collection as it assists in quantifying the sensitivity of the sensors. For our studies, we will focus on TES circuit-related

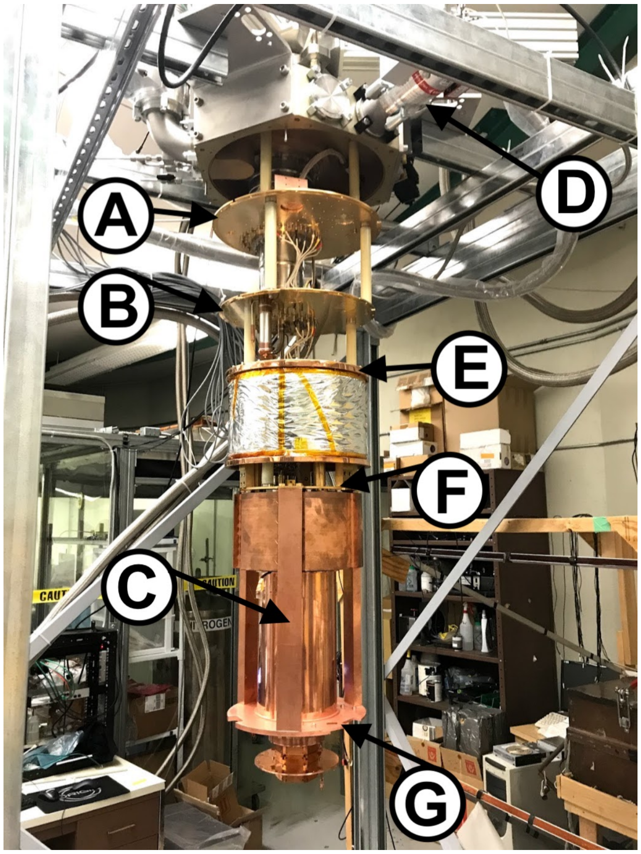

Figure 4.14: The CUTE dilution refrigerator prior to closing the cans. A: 60K plate. B: 4K plate. C: MC rods holding the top MC plate with bottom one. D: OVC turbo pump. E: Still plate. F: the top MC plate. G: the bottom MC plate.

noise, because the noise in the readout circuit is expected to be fixed and negligible.

After a successful payload installation and cool down, the fridge has reached a base temperature of ∼17 mK in about 4 days. Then, the first task was to tune the Superconducting Quantum Interference Devices (SQUIDs). Once the SQUIDs were tuned at a good responsivity (about 1000 mΩ), we tried several settings to tune the SQUET[2] cards in order to minimize the noise to the level, as depicted in Fig. 4.15.

To study the noise levels and evaluate the fridge performance with the current

---

[2] SQUET card: consists of both, the SQUID card and the FET (Field Effect Transistor) cards.

setup, several datasets were taken while changing the following parameters:

- Feedback gain value (2, 5 and 10)
- Polarity (inverted, non-inverted)
- TES state (Superconducting, Transition and Normal)
- RF shield added to the VIB (room temperature electronics)

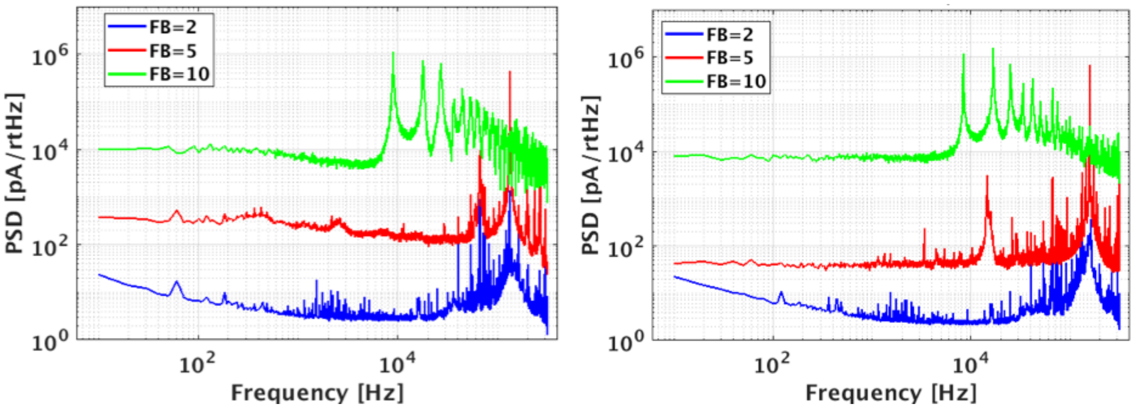

Figure 4.15: *Left*: Normal noise PSD at different feedback gains and non-inverted (left) and inverted (right) polarity. At the lowest feedback gain, the noise levels are approaching the expected level.

Initial tuning tests have allowed us to optimize the polarity and feedback gain, then to record several noise traces in superconducting, transition, and normal modes, and took some preliminary data using T2Z2.

To be able to diagnose the phonon readout circuit and set each of the TESs at the desired transition level, we measured the normal (R_n) and parasitic (R_p) resistance for each phonon circuit, as summarized in Table 4.1. Using the information in Table 4.1, we adjusted the current through the sensors of T2Z2 to be at 40% in transition and recorded the PSD. The superconducting (SC) and normal (N) noise levels were found to be comparable to that measured in Berkeley for normal and superconducting. The noise levels are shown in Fig. 4.16.

Sensor	R_p [mΩ]	R_n [mΩ]
PAS1	9.1	621.9
PBS1	13.1	622.9
PCS1	9	568
PDS1	10	660
PAS2	9.5	600.5
PBS2	9.7	536.3
PCS2	8.8	413.2
PDS2	9.8	526.2

Table 4.1: The measured resistance values for the readout electronics during the first run for CUTE.

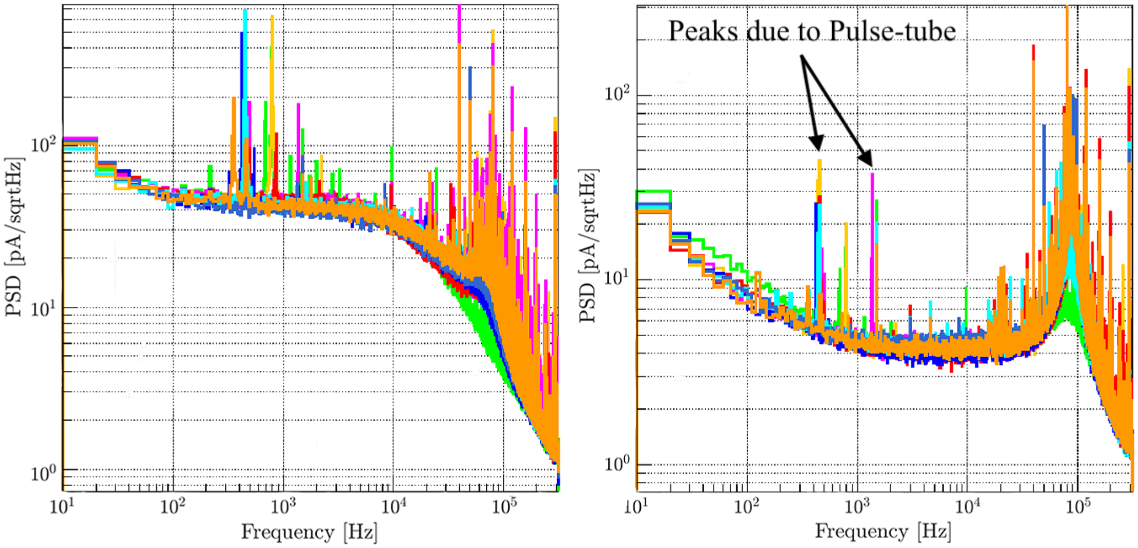

Figure 4.16: *Left*: PSD as a function of frequency for phonon sensors of T2Z2 while operated in SC mode. *Right*: PSD in N mode. The peaks have been verified to result from the PT vibrations.

In terms of the TES samples, we could not utilize them for our studies of this run because the connection for three out of the four connected channels was lost after cooling down. Moreover, the fourth TES channel never went superconducting which might be related to a temperature gradient between the MC plate and the TES samples.

4.8.1 VIB Box Effect

A PSD was recorded for the T2Z2 sensors while being set at 40% in transition, and we observed a high noise at the low-frequency range. The noise level is comparable to that recorded at SLAC with detector G124. We were able to eliminate some of the peaks by covering the DCRC with a metallic box. The effect on the noise level is depicted in Fig. 4.17. Although this is true for this run, the effect of the DCRC box was less evident in later runs.

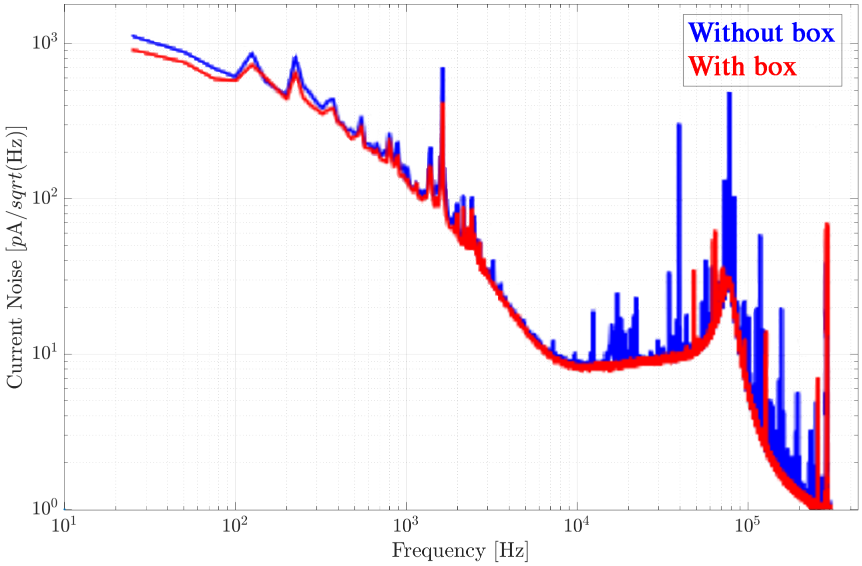

Figure 4.17: Covering the DCRC with a metallic box had a significant effect in reducing the high-frequency noise in T2Z2.

4.8.2 Detector Calibration: Am Source

In an attempt for utilizing the ^{241}Am source to calibrate the energy scale of T2Z2 and take threshold data. It turned out that the source was shining too close at the detector, on mostly one phonon channel, as depicted in Fig. 4.18 and the events rate was extremely high (more than 100 HZ).

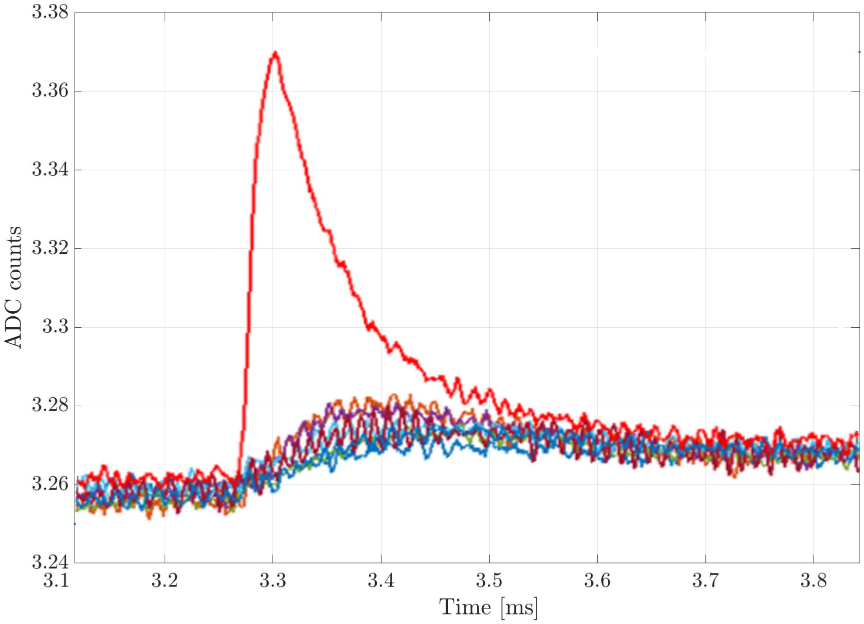

Figure 4.18: Pulse shape for the phonon sensors in T2Z2, resulting from an ^{241}Am source shining mostly on a single phonon sensor at a very high rate.

4.8.3 Conclusions and Future Work

Although this was a relatively short run (4-5 days), we managed to achieve most of the goals, and most importantly, we confirmed the compatibility of all produced parts with the tower and fridge. We were also able to measure the noise levels and compare that with measurements from SuperCDMS test facilities at the University of California, Berkeley (UCB), and SLAC.

Since there is a series of thermal connections between the thermometer at the MC plate and the tower, it was recommended to install a thermometer at the MC stage of the tower to determine if there is any thermal gradient. Such a gradient would be a concern for testing the new SuperCDMS detectors since they have a lower superconducting transition temperature than the detector tested here and thus might not get cold enough for the operation. Moreover, it is also recommended to collimate the Am source to reduce the event rate down to ∼5 Hz.

4.9 Experimental Setup: G115

The use of detector G115 aimed to continue the noise studies to better determine the factors affecting the noise environment and evaluate the fridge performance. It also aimed to confirm that the actual temperature at the MC stage of the tower is close to what we can measure on the MC plate.

Similar to the setup in section 4.6, TES samples were installed in addition to detector G115[3] as our run payload. A new collimator was designed and produced to reduce the event rate from the ^{241}Am calibration source. We have also installed a magnetic-field-fluctuation thermometer (Noise Thermometer) [106] at the MC stage of the tower to measure the exact temperature of the detectors, as shown in the setup in Fig. 4.19.

4.10 Noise Studies Using Detector G115

Several variables were changed to test their effect on noise levels. Only major sources of noise will be listed in this section.

---

[3] G115: is 4mm x 3 Mercedes-like, Ge crystal with four phonon sensors having the new SuperCDMS HV QET.

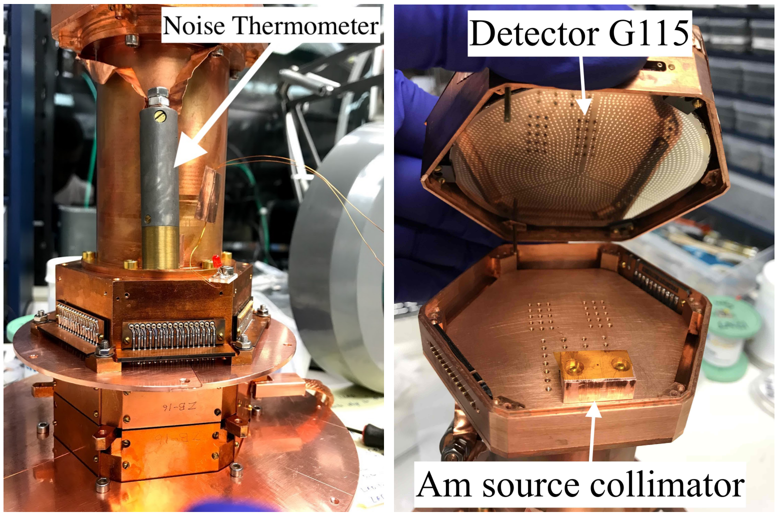

Figure 4.19: *Left*: The Noise Thermometer attached to the MC stage of the tower. *Right*: A collimator for the ^{241}Am source facing detector G115.

4.10.1 POE Effect

The single-port POE[4] turned out to introduce significant noise at high frequencies, but once we switched to the new POE (the one to be used for CUTE at SNOLAB), many of the peaks at the high-frequency range have disappeared, as depicted in Fig. 4.20.

4.10.2 Pulse Tube Effect

The test for the PT effect on noise level indicates that the PT introduces a noise peak to the signal at ∼750 Hz, in addition to several smaller peaks on the order of 10 kHz, as depicted in Fig. 4.21.

---

[4] Power Over Ethernet (POE): is used to power our DCRC boards through Ethernet port.

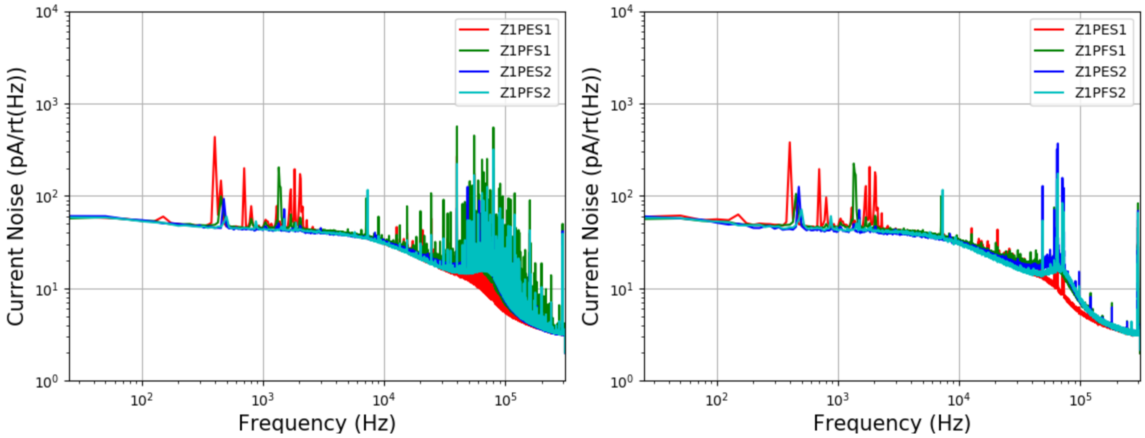

Figure 4.20: *Left*: Superconducting noise PSD for detector G115 when the DCRC board is powered via an old version POE. *Right*: Noise PSD for the same phonon channels and at the same settings, but using a newer version POE. (PSD plots were generated by the CUTE operations team, at Queen's).

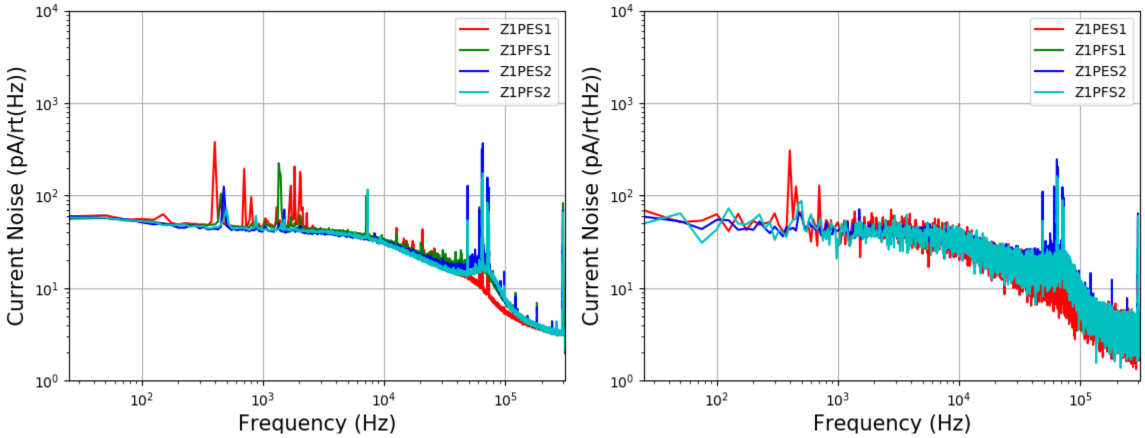

Figure 4.21: *Left*: Superconducting noise PSD from four sensors in detector G115 while running the PT. *Right*: Noise PSD was taken while the PT was off for the same sensors. (PSD plots were generated by the CUTE operations team, at Queen's).

4.10.3 VIB Box Effect

The use of the VIB box aims to shield the DCRC boards from radio-frequencies. Similar to what was concluded in section 4.8.3, we verified that the box reduces the high-frequency noise, as depicted in Fig. 4.22. It also seems to mitigate the peak at $\sim$ 10 kHz.

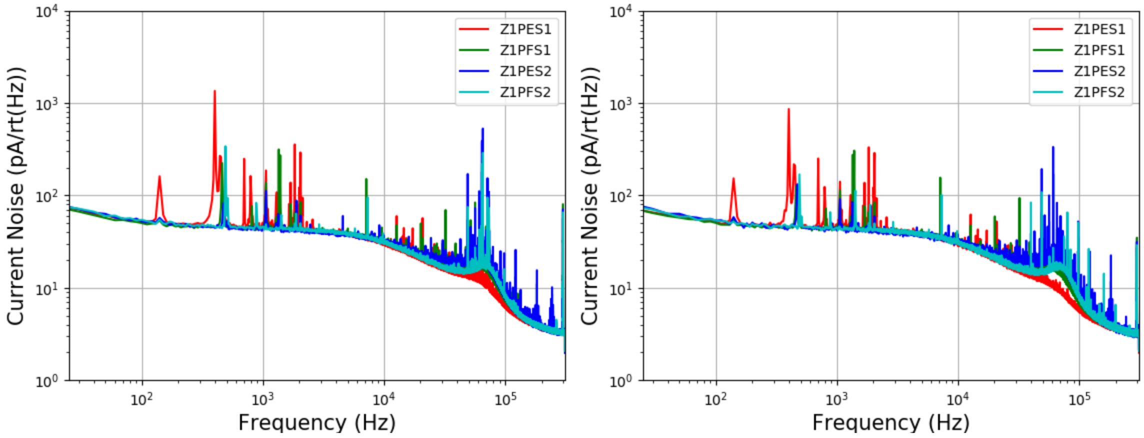

Figure 4.22: *Left*: Superconducting noise PSD while having the VIB box installed. *Right*: Superconducting noise PSD after removing the VIB box. (PSD plots were generated by the CUTE operations team, at Queen's).

4.10.4 Environment and OVC Turbo Effect

The results from the final few tests in this run were about the effect of laboratory lights and fans on noise levels. Once they were all turned off, there was no significant observable change in the noise level compared to the state when they were on. On the other hand, when we turned the OVC turbopump off, we observed a drop at the $\sim$3 kHz peak, as depicted in Fig. 4.23.

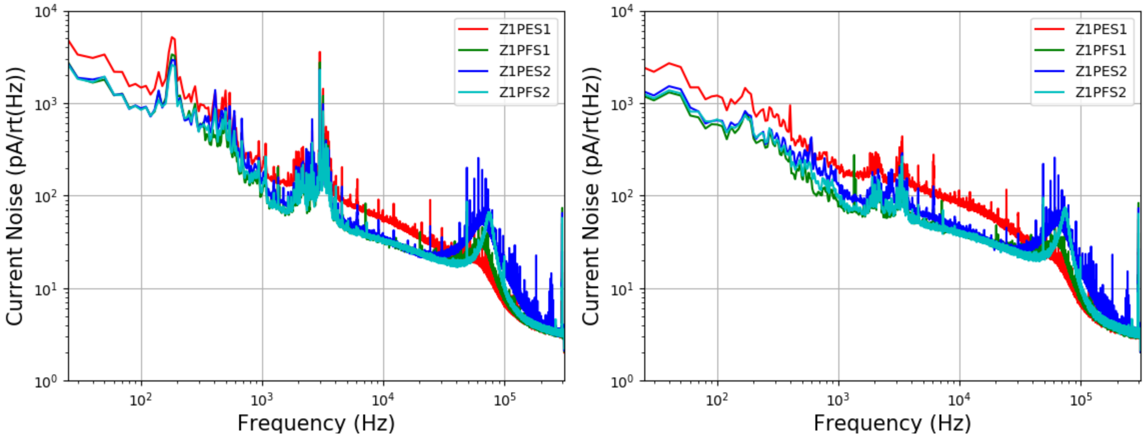

Figure 4.23: *Left*: Transition noise PSD while the OVC turbo is running. *Right*: Transition noise PSD when the OVC turbo is off. (PSD plots were generated by the CUTE operations team, at Queen's).

4.11 Underground Tests at CUTE Facility

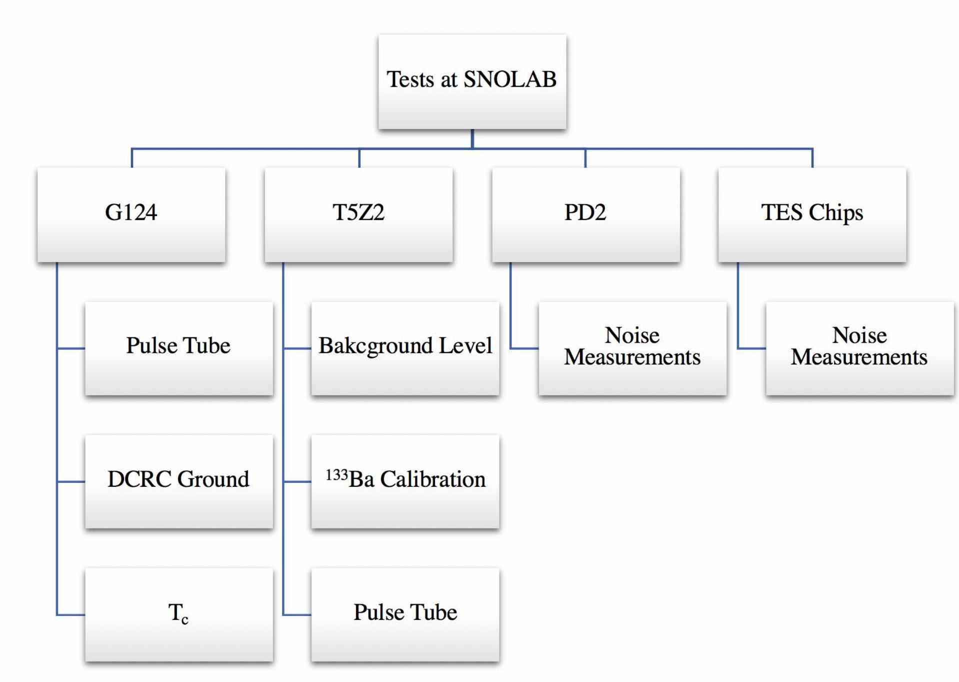

Figure 4.24: A chart summarizes the tests performed at SNOLAB. Level two in the chart is the detector name. Level three is the test type.

In the remaining sections of this chapter, I will introduce the measurements performed at the CUTE facility after the installation was completed underground at SNOLAB. The measurements will utilize a variety of detectors to study the fridge performance and to identify the sources of noise as shown in the road map in Fig. 4.24.

During one of the underground runs, I have also performed a test on the e-gun (a prototype for low-energy detector calibration), which is described in detail in section 5.7.

4.12 The New Tower of SuperCDMS at CUTE

As a first underground test for the dilution refrigerator at CUTE while holding the new tower designed for the new generation of the SuperCDMS experiment, shown in the left panel of Fig. 4.25. Several parts were necessary to make sure that we can fit and operate the new detector. For that, we installed a new readout cable from RT down to the 4 K stage in addition to the tower package (provided by SLAC). A new version of the HV VIB and two Rev.E HV DCRCs (SN18 and SN20), were provided by Fermilab, which is shown in the right panel of Fig. 4.25. A Vertical Flex Cable (VFC) was used to connect between the DIB at the MC stage and the readout cable at the 4 K stage of the tower, shown in the left panel of Fig. 4.25. Due to a break in two of the VFC traces, we will be able to readout only ten out of twelve sensors during the following tests.

The HV - G124 detector has already been described in section 3.5. In this run, we will make the first attempt to operate the new generation of detectors in HV mode. The SuperCDMS tower is able to fit a stack of six detectors and should be provided with six VFCs, each is at a specific length. To be able to connect the only

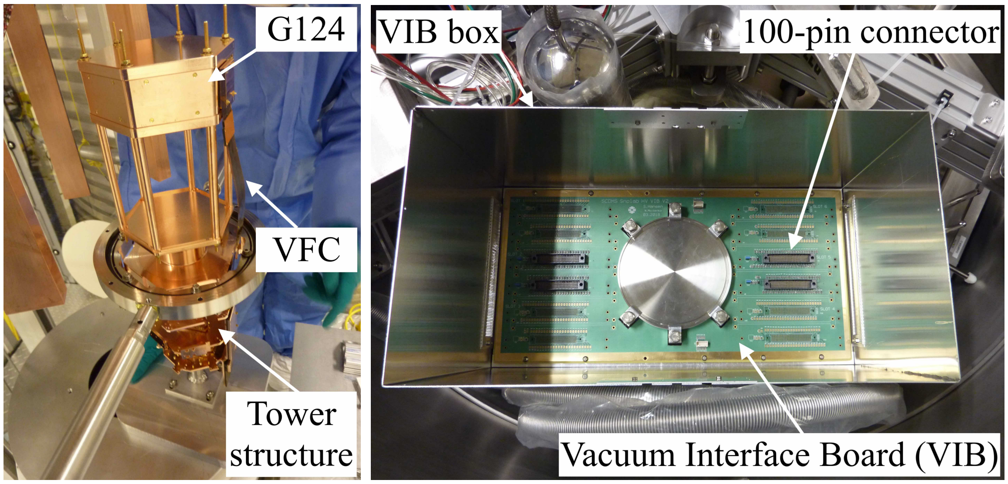

Figure 4.25: *Left*: Detector G124 attached to the tower and readout through the VFC. *Right*: The first HV-VIB board to be tested along with the VIB box (without the lid) after installation at CUTE.

VFC we have without bending (the cable can only tolerate limited bending without breaking), we added supporting rods, as shown in the left panel of Fig. 4.25, to elevate the detector to the proper height.

Although CUTE is equipped with a vibration isolation system, it was not yet ready to be activated for this run. This will increase the impact of the local seismic activity and other vibrational noise sources on our noise levels because the fridge will be rigidly fixed to the frame.

4.12.1 Initial Experimental Setup: T5Z2 & PD2

Detector T5Z2 (the fifth detector tower T5, which includes detectors Z1, Z2 Z3) is a 3-inch germanium detector, similar to that used in section 4.8, reused from the former SuperCDMS experiment at Soudan. PD2 is ∼11 g silicon detector (1 mm thick and 3-inch in diameter) with a single phonon sensor, shown in the left panel of Fig. 4.26. In addition, we installed a small Si substrate with 3 TES samples of different sizes

(800 μm×200 μm, 400 μm×100 μm, and 200 μm×50 μm). The substrate is the dark square at the bottom of the middle panel in Fig. 4.26.

The samples are useful because they can provide information about the intrinsic noise sources and they allow us to measure the total noise. On the other side, the combination between detector PD2 and the TES samples can help in differentiating between the power-coupled noise of the Electromagnetic Interference (EMI) along the bias line or EMI picked up by the antenna structure, while T5Z2 and PD2 can provide information about facility backgrounds in different energy ranges.

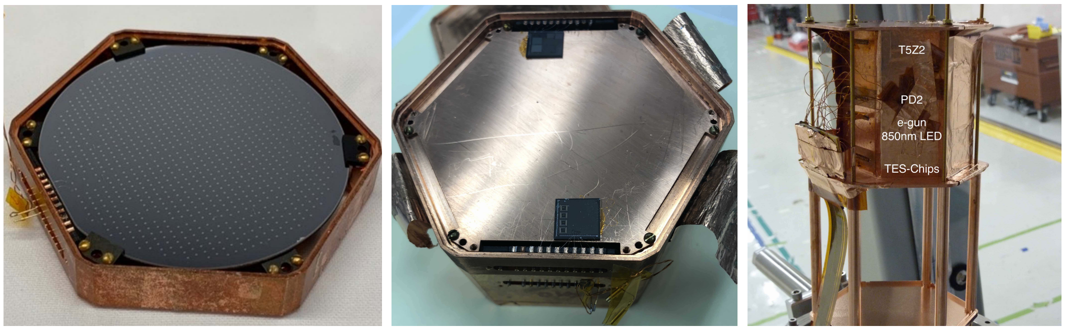

Figure 4.26: *Left*: Top face of detector PD2 in a 3-inch detector housing. *Center*:TES samples patterned on a Si waver (bottom dark square), mounted in a 3-inch detector housing. *Right*: The detector stack (top to bottom): T5Z2, PD2, e-gun and TES samples.

4.12.2 Modified Experimental Setup: G124, T5Z2 & PD2

To give a comprehensive review of the underground run outcomes, I will list in this section some modifications made to the previous setup before going through the combined results.

First, we removed the e-gun from the detector stack, due to the suspicion that radioactive contamination of some components of the e-gun could have contributed to the high event rate in PD2. Second, we installed the Noise Thermometer at the detector stack to confirm the temperature of the MC stage of the tower, because two of the TES samples did not go superconducting in the previous run. Third, we improved the isolation of PD2 to prevent IR radiation from reaching the detector. This was done by adding flat Cu plates on both sides of PD2. In this setup, we have also placed PD2 below T5Z2 to provide PD2 with some extra shielding from the potential background from above. The combination of detectors G124 and PD2 will help us to differentiate between vibrational (more obvious in G124) coupling and Radio Frequency (RF) heating. The full payload is shown in Fig. 4.27.

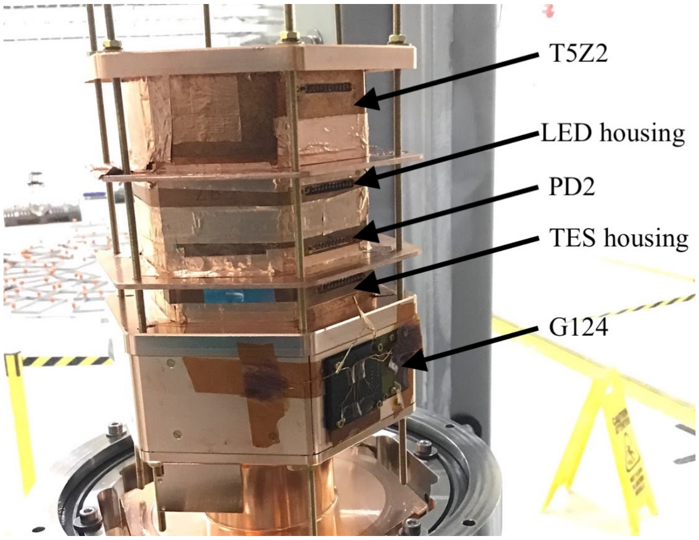

Figure 4.27: Modified setup for further noise studies in a later run.

4.13 Studies Using Detector G124

This detector is more sensitive to vibrations than the other detectors because it's more massive. Therefore, we are using this feature to perform the following vibration tests.

4.13.1 Pulse Tube Noise

Although the suspension system was activated during this run, the effect of turning off the PT on noise levels was significant, as depicted in Fig. 4.28. This was a clear indication that the suspension system was not actually isolating the cryostat and further investigation was necessary to confirm that.

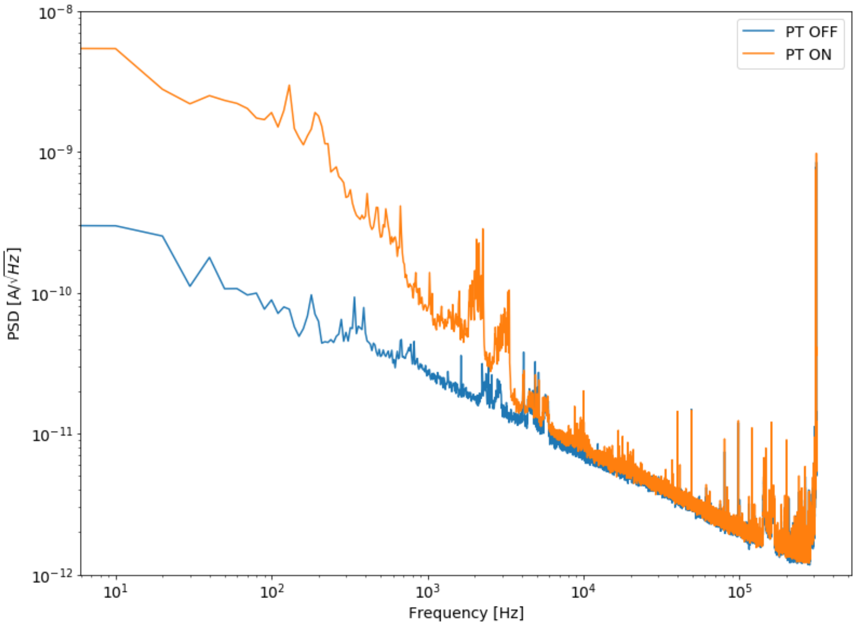

Figure 4.28: Vibration effect on a transition noise PSD for one of the sensors in detector G124 before, and after turning the PT off. Source: CUTE operations team.

4.13.2 Grounding the DCRC Board

In an attempt to record the effect of grounding the DCRC boards to the cryostat chassis, we added a grounding cable between the analog ground of the DCRC board and the chassis. However, the grounding connection resulted in increasing the overall noise level, as depicted in Fig. 4.29. Besides the results from the PT measurement in section 4.13.1, this test was another indication of possible electrical contact between the cryostat and the chassis.

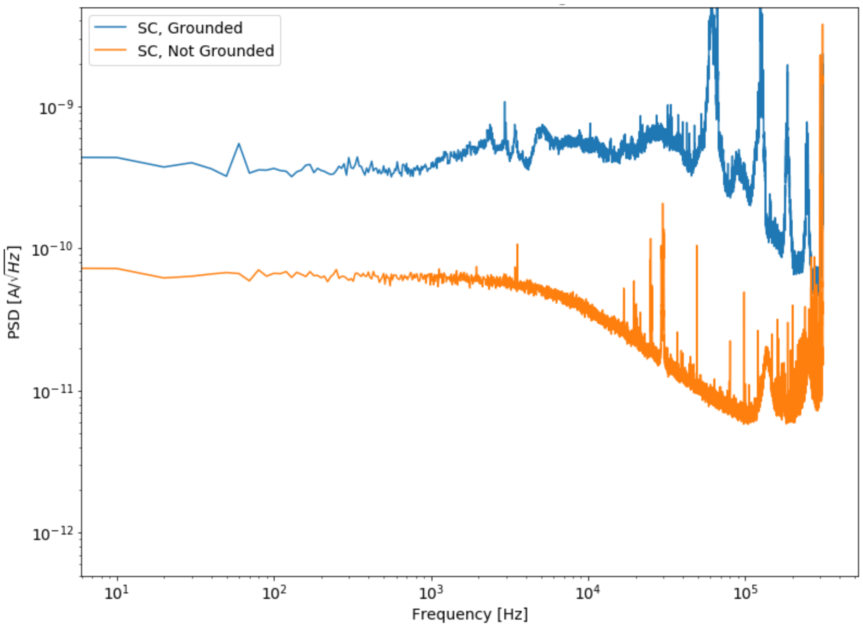

Figure 4.29: A significant increase in noise level results from connecting the analog ground of the DCRC board to the fridge chassis. Source: CUTE operations team.

4.13.3 Tc Measurements

This measurement was performed using the nine working sensors of detector G124. We measured the change in the operational QET bias and the stability of the sensors over the course of the run. The QET bias was set at 50% of the normal resistance (R_n). On average, the QET power has increased over time, as shown in Fig. 4.30. This increase may indicate that the detector is getting colder over time. Thus, more power is required to keep the QET at the same transition point.

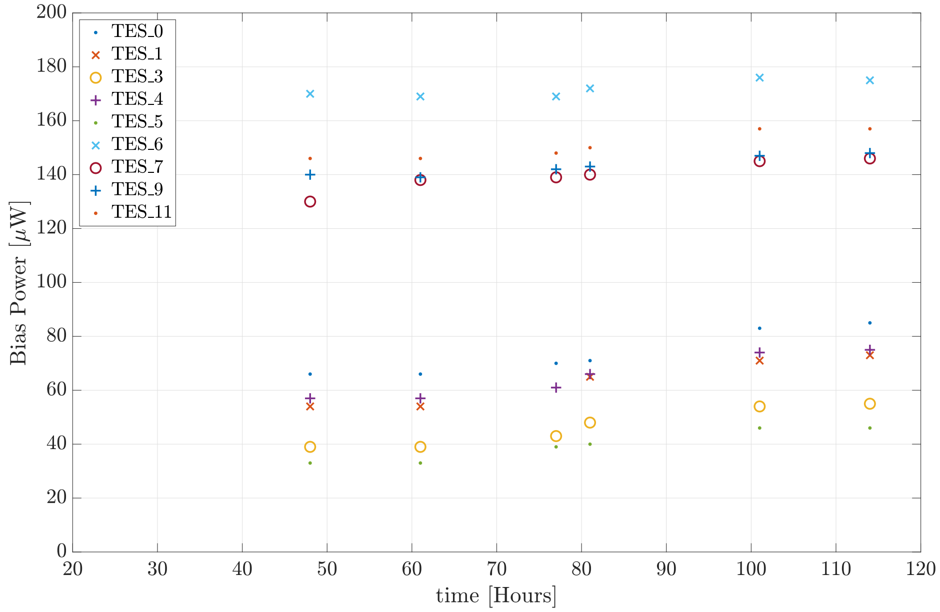

Figure 4.30: The change in bias power in each TES over time since the MC reached base temperature, for the sensors of detector G124. Source: CUTE operations team.

4.14 Studies Using Detector T5Z2

The vibrational measurements with G124 in the previous run indicated a problem with the alignment of the suspension system; this finding was supported by the lack of response of the fridge position to air pressure changes and confirmed by electrical contact between the PT cold head and the fridge (if properly aligned there should not be a contact). Before the next run, the PT cold head was aligned and the mechanical and electrical isolation was confirmed. Afterward, the payload was changed to perform the tests and measurements listed in the following sections.

4.14.1 Background Level

Background data was taken for several days using detector T5Z2. The energy scale was calibrated via the 10.36 keV line resulting from Ge activation, as depicted in Fig. 4.31. A background rate of $\sim$ 7 dru was determined from the same spectrum for the energy range from 15 to 50 keV. The steep rise of the event rate below 8 keV has not been studied in detail, but maybe a combination of cosmogenically produce tritium and the onset of readout noise.

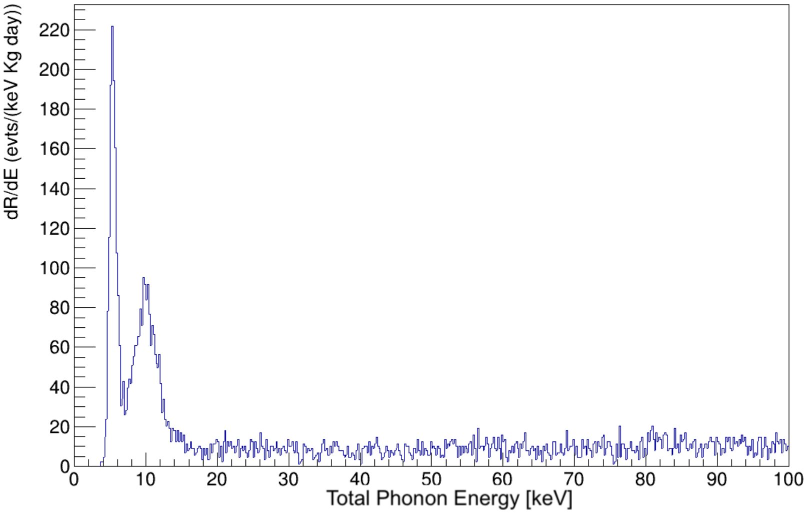

Figure 4.31: Low background data from detector T5Z2. The peak at low energy is background noise. Source: CUTE operations team.

4.14.2 Ba Calibration

To confirm the calibration factor that we used in the low background data from Ge activation peak at 10.36 keV, a ^{133}Ba source was deployed and resulted in the following three peaks shown in Fig. 4.32.

Although the measured mean value of the three peaks does not exactly match with the expected one, this shows that the calibration factor we used from the Ge activation line was acceptable, more statistics are required in future runs.

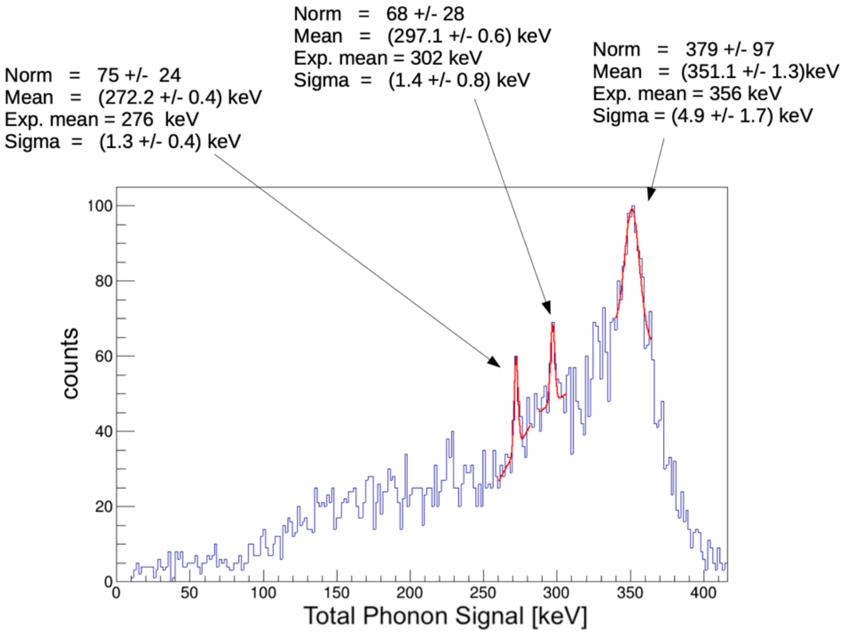

Figure 4.32: Ba data taken in detector T5Z2 after calibrating the energy scale via the germanium activation line at ∼10 keV. Source: CUTE operations team.

4.14.3 Pulse Tube Effect

With the now properly aligned PT cold head, the suspension system was now working as designed. Data were taken using T5Z2 with the sensors in transition (50% R_n). In Fig. 4.33, noise PSDs with PT on and PT off are shown for each sensor, with no significant difference between the two states.

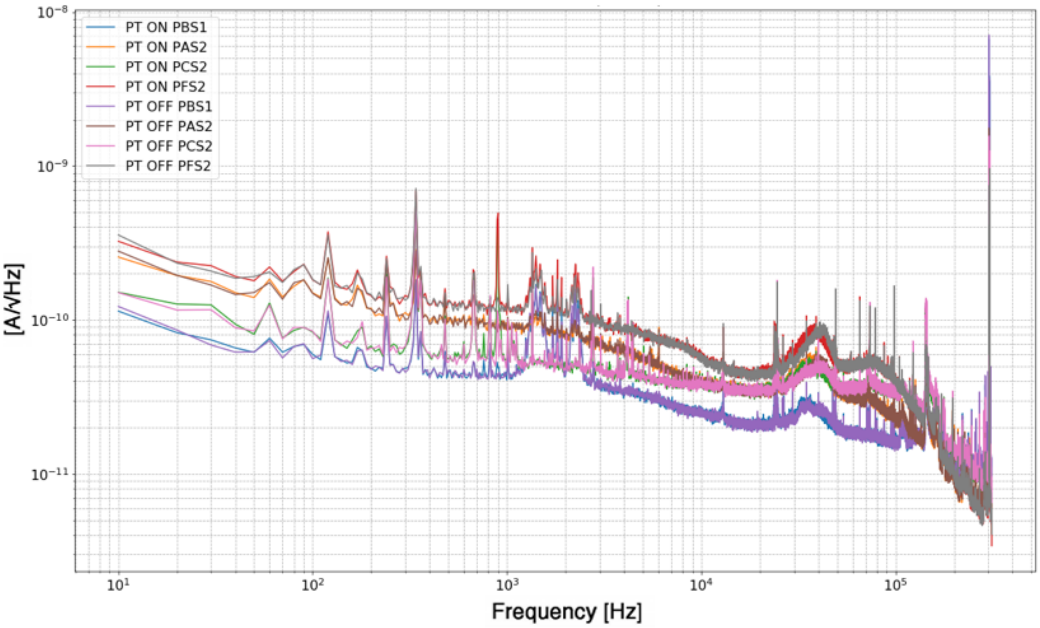

Figure 4.33: Transition noise PSD for detector T5Z2 when turning the PT on and off. The sensor name shown in the legend follows the following name convention: “Phonon”+“Sensor Name”+“Detector Side Number”,i.e. “P”+“B”+“S1”.

This is a key observation for two reasons: First, we were able to confirm the functionality of the suspension system, i.e. it keeps the fridge floating. Second, it helps in mitigating the noise sources at the facility.

4.15 Noise Measurement Using Detector PD2

A significant effort was undertaken at SLAC to study various noise sources at their dilution refrigerator. Knowing that detector PD2 has already been utilized in their noise studies, gives us a reference to compare with our results, and to estimate how close the CUTE facility has reached in mitigating its noise sources for achieving the best energy resolution in our detectors. By comparing the noise levels in PD2, as shown in Fig. 4.34, we can see that it is slightly higher in CUTE than SLAC. This result pushes the CUTE operations team in specific, and the SuperCDMS collaboration in general, to put more effort towards hunting more noise sources as well as mitigating the known ones even more.

4.16 Phonon Energy Resolution of Detector PD2

Detector PD2 was installed in the dilution refrigerator of the CUTE facility in two separate runs and the phonon resolution was measured at each time (the setup was described in sections 4.12.1 and 4.12.2). The phonon resolution was found to be significantly different at each time. In the first, it was about 7.4 eV while in the second was $\sim$4 eV. Moreover, it was also different than that measured at SLAC ($\sim$2.8 eV). We currently think that a few major reasons may have contributed to the difference in these measurements: First, the difference in the optical isolation of the detector (it was better in the second run). Second, a better tower shielding for IR at the MC stage in the later run. Third, the difference in noise levels between the two facilities. Consequently, more investigation is required to verify these hypotheses.

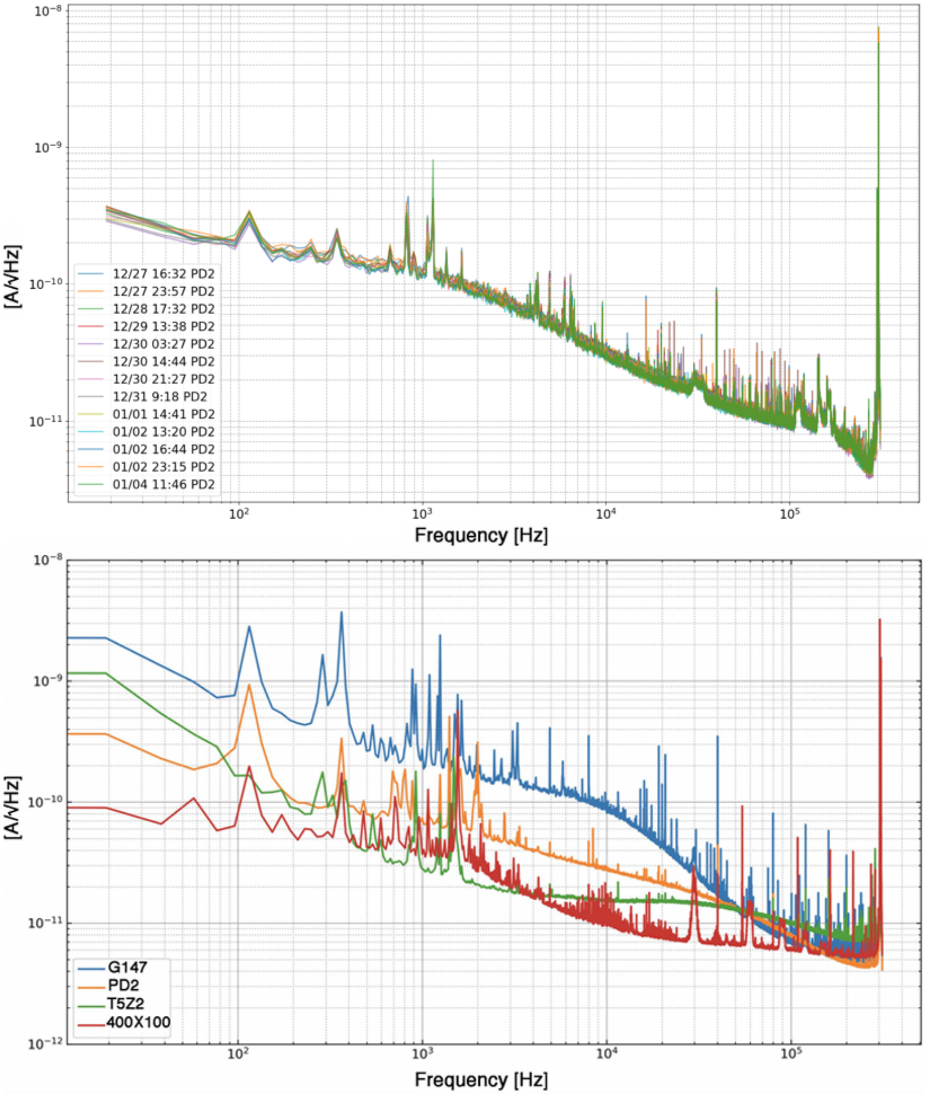

Figure 4.34: A comparison of noise levels in detector PD2 at CUTE in the *Top* panel and that for the same detector at SLAC in the *Bottom* panel.

4.17 Summary and Future Work

The work on getting the CUTE facility ready for taking science data is still in progress. We are currently at the phase where we try to understand the fridge environmental noise sources and scientific capabilities. For that, several analyses were performed and some are still in progress to compare the results from CUTE, with those from other test facilities within the SuperCDMS collaboration.

Achieving a good noise level at CUTE is currently the main task of the operations team. To mitigate the currently identified sources, listed in section 4.4, more effort needs to be done, and further investigation for other sources is required in future runs. The list in Table. 4.2, summarizes the currently identified sources along with the current work status.

The work on the purge gas flow is still in progress, but we think that we found a limit that we can apply to the flow rate to gain the best acceptable noise levels. However, this can not be tested before the experiment goes back online (currently, the work at SNOLAB is prohibited due to global health concerns and travel restrictions).

The detectors installed and tested at the CUTE facility have enabled the operations and data analysis teams, to perform preliminary studies about background rates in these detectors. Unfortunately, the run has suddenly ended due to a blockage in the circulation loop (due to operations error). In future runs, more statistics for extended periods will be required to further understand the decrease in the background level over time, and to investigate the difference in background rates between the various runs.

In some studies, it was also noticed that when data was taken at a high rate, telegraph noise became more prominent in some detectors. Therefore, more investigation

Noise source	Current work status	Future work	Related sections and analyses
Pulse Tube	Suspension system has been aligned, which significantly reduced the effect of PT vibrations	Further investigation for additional noise mitigation	4.3.2, 4.4.1, 4.10.2, 4.13.1, 4.14.3, [107]
VIB box	The box has reduced the amplitude of high frequency peaks	Adding VIB struts to properly attach the DCRC board. Further investigation for induced telegraph noise once the box is attached	4.8.1, 4.10.3
Peltier cooler	The Peltier cooler is currently attached to the turbopump	Electrically isolate the Peltier Cooler from the fridge and replace its temperature controller	4.4.3
Compressed gas	Mitigating the effect of purge gas by optimizing the gas flow	Acquiring a new flow meter for adjustable to lower flow rates	4.3.6, 4.4.2, [108]
Slow control rack	Work is in progress to electrically isolate the slow control rack components and control units from the fridge	More testing for possible electrical contact between the slow rack components and the fridge chassis	4.3.5

Table 4.2: Summary of the major noise findings at CUTE facility.

is required to identify the sources of such noise and to try to eliminate those sources.

Chapter 5

LED-based Calibration Studies

5.1 Introduction

Two of the main purposes of detector calibration in SuperCDMS experiment are: Testing the detector stability over time and establishing the detector energy scale at our region of interest (see section 3.8 for more details about calibration in SuperCDMS).

The new SuperCDMS detectors are optimized for low energy interactions, where gammas from external radioactive sources would not penetrate the cryostat walls. Neutron activation would still work, but it is only applicable to germanium and not silicon and it produces a persistent background (half-life of ^{71}Ge is 11.43 days) [103]. In addition, any calibration with a radioactive source requires an extended acquisition time to acquire enough statistics to identify the relevant peaks.

In this chapter, I will discuss in detail several studies investigating the feasibility of using LEDs for detector calibration, which would overcome the drawbacks listed above.

5.2 Band-gap Change in Semiconductors at Cryogenic Temperatures

5.2.1 Introduction

The SuperCDMS collaboration has started to perform studies to probe the use of LEDs. Consequently, those studies have led to some questions, such as: What is the exact emitted wavelength for the LEDs when used at cryogenic temperatures? What type of event will the photon produce in the detector (bulk or surface)? What is the quantum efficiency for these photons? In addition to many other questions.

To provide answers to some of these questions, I will present measurements for the shift in the Current versus Voltage (IV) curves and spectral peak emission as a function of temperature. This shift results from the inter-atomic characteristics that affect the band-gap energy. I will also present the results for changing the LED operation parameters on the emission spectra and finally, will show an estimation for the penetration depth of a selected wavelength into our germanium detector. The measurements were performed for two LEDs of wavelengths 1650 nm and 1200 nm at temperatures between 300 and 7 K. This chapter will only focus on the 1650 nm wavelength while a sample of the results for the other wavelength is reported in Appendix B to avoid the repetition of similar results here.

5.2.2 Background

We selected an LED of wavelength 1650 nm (0.75 eV) so that the energy of emitted photons is between the direct and indirect band-gap of germanium. Fig. 5.1 shows the germanium band structure for reference [109]. The 1650 nm photons are expected to have a relatively high penetration depth in the germanium crystal, and most interactions are expected to be away from the surface. Initial tests using the 1650 nm

LEDs revealed a discrepancy between the expected penetration depth of 17 cm [110], and the measured one at less than 1 cm in our germanium crystal. Therefore, we decided to measure the actual emission spectrum at cryogenic temperatures - close to our detector's operating temperature.

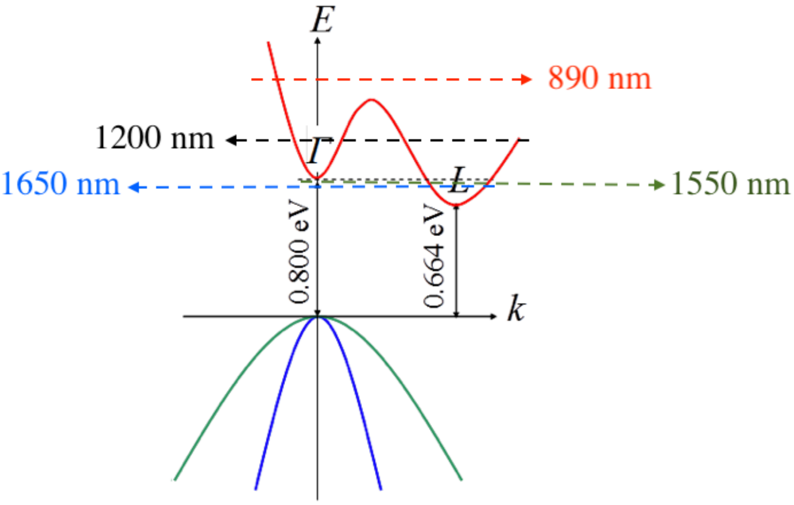

Figure 5.1: Germanium band structure at room temperature. Image modified from the source by adding the projections of various LED energies [111].

5.2.3 Dependence of Energy Gap on Temperature

Similar to other semiconductors, the dependence of the energy gap in InGaAsP on temperature, is expected to follow Varshni's formula:

$$E_g(T) = E_o - \frac{T^2\alpha}{T+\beta} \tag{5.1}$$

where α and β are constants determined experimentally, $E_g(T)$ is the energy gap as a function of temperature, and E_o is the energy gap at 0 K [112]. So, as the temperature change, the lattice constant changes, which will cause a change in the energy gap [113, 114]. The photon energy is determined by the bandgap energy and hence, the emission wavelength $\lambda = \frac{h \times c}{E_g}$ (where h is Plank's constant and c is the speed of light) decreases with an increase in the bandgap energy.

5.2.4 Experimental Setup

The measurements reported in this section were performed using an optical cryostat and other peripheral devices located at Prof. Philippe Di Stefano's Laboratory - Queen's University. A block diagram of the setup is shown in Fig. 5.2. The closed-loop ColdEdge cryostat is able to cool down to ~7 K. The temperature is monitored, and two built-in heaters are controlled, via a temperature controller (CRYO.CON 22C).

A shielded single-mode optical fiber of type VIS-NIR with a diameter of 600 μm along with a NIR Spectrometer, model NIRQuest-512-2.5 was provided by Gamble Technologies Ltd. The spectrometer has an InGaAs linear array detector that covers wavelengths between 900-2500 nm, with an integration time of 1-200 ms [115]. The optical fiber was attached on one end to the cryostat's transmission windows after we confirmed that the window is able to transmit at least 90% of the desired wavelengths [116]. The other end of the fiber was connected to the spectrometer.

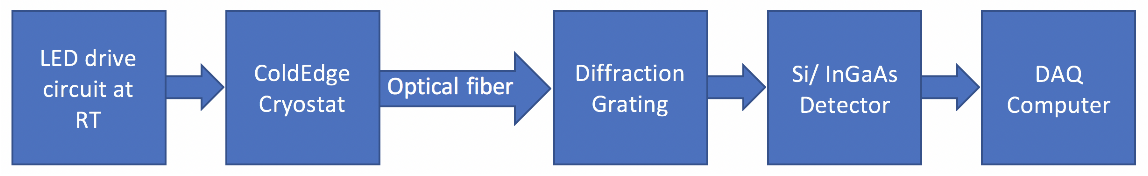

Figure 5.2: A block diagram for the experimental setup.

The LED chips were mounted on a ceramic holder and sealed with epoxy resin [117]. Two LED packages were mounted on a 1×1 cm^2 PCB, which in turn was attached to a gold-plated copper disk, as shown in Fig 5.3. This disk was attached to the cryostat cold head using four 10 cm long copper rods which brought the LEDs as close as possible to the top window, maximizing the number of photons collected by the fiber.

On the DAQ computer, we used Oceanview software to collect data and subtract the IR background radiation. The integration time was set to 150 ms to keep our signal below 85% (to avoid saturation) of the maximum amplitude signal that the spectrometer can receive. We have also chosen to take an average of three measurements to increase the stability of the spectrum.

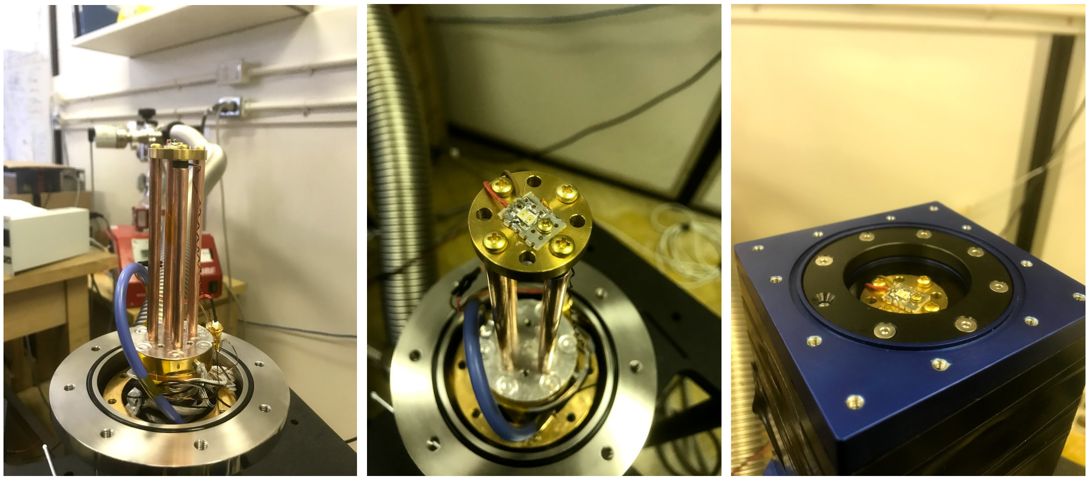

Figure 5.3: *Left*: Four copper rods are attached to the cryostat's cold head to elevate the LED to a position near the top window. *Middle*: Top view showing the two LEDs attached to the PCB and screwed to the cold head. *Right*: The cryostat top window before attaching the optical fiber.

5.2.5 Apparatus - IV Measurement

An Elegoo Uno (Arduino) was used to simultaneously apply a voltage across the LED and measure the current passing through it. The Arduino circuit is depicted in Fig. 5.4. A code to increase the voltage across the LED from 0 to 5 V in several increments was implemented by Matthew Peterson-Galema. RC low pass filters were added to the circuit to change the output signal into a DC on either side of the circuit to operate two LEDs during the same run (in opposite polarity, one LED can work at a time). The code is designed to record a maximum of 50 increments (steps) of the current, voltage, and their standard deviations separated by 5 ms at each step.

Table 5.1 summarizes the purpose of each component and readout pin in the Arduino circuit.

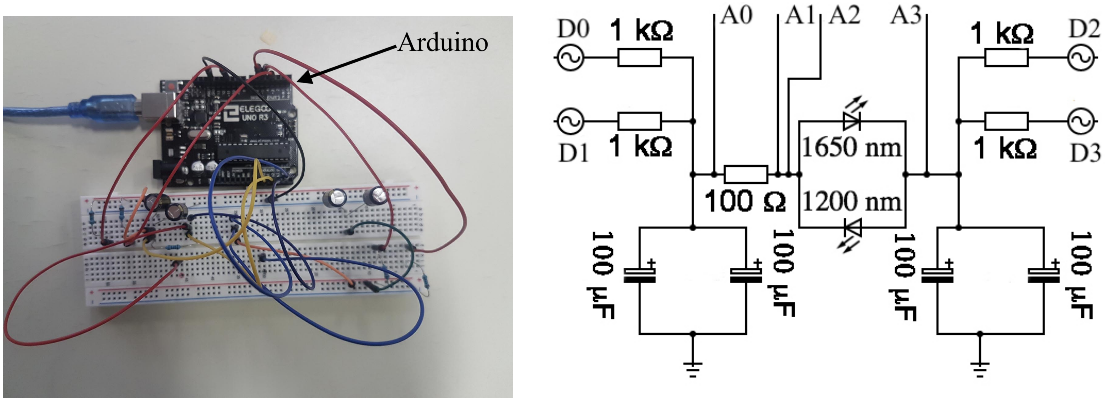

Figure 5.4: *Left*: The Arduino connected to an Ethernet readout cable and a breadboard to operate the LED. *Right*: Schematic diagram for the components on the breadboard showing the pins used to measure the current and voltage across the LED.

5.2.6 Methodology

Starting from base temperature (∼7 K), we had two types of measurements to perform at each temperature point. First, we controlled the applied voltage for the whole circuit and measured the LED current (using pins A0 and A1) and the voltage drop across the LED (using pins A2 and A3). This measurement provided us with the

Component	Value	Function
Resistor	100 Ω	To calculate the current passing through the LED
	1000 Ω	Low-pass filter to convert the current into a DC
Capacitor	100 μF	Total of two capacitors connected in parallel with $C_{equivalent} = 200$ μF to have the DC as flat as possible
D0, D1		To turn the 1650 nm LED on while D2, D3 is set to the ground
A0, A1		To measure the current passing through the LED
A2, A3		To measure the voltage-drop across the LED
D2, D3		To turn the 1200 nm LED on while D0, D1 are set to the ground

Table 5.1: List of the circuit components and pin assignment.

required data for the IV curve studies. Second, we recorded the emission spectrum at two different current values, 1 mA and 3.3 mA (where the latter is the maximum output current that could be achieved with our LED drive circuit).

To change the base temperature, we adjusted the temperature controller, which in turn controlled the power of the built-in heaters at the cold head. The heaters were able to increase the temperature from the base to 300 K with 0.1 K increments.

Eventually, an IV curve and spectral emission were recorded at each temperature point for each LED, after giving enough time for the LED to thermalize, and making sure we have stable temperature readings for at least 15 min.

5.2.7 Results and Discussion

The results in this section are divided into two categories: The first is related to the IV measurements for the 1650 nm LED. The second focuses on the emission spectra. A sample of the results is also reported in Appendix B for the 1200 nm LED.

5.2.8 IV Characteristic Curve

As the temperature decrease, the lattice constant decreases [113] and the band-gap increase [114]. Fig. 5.5 shows the measured IV curves for a set of temperatures; as expected, the current onset (corresponding to the internal work function) shifts to higher voltages with a decrease in temperature.

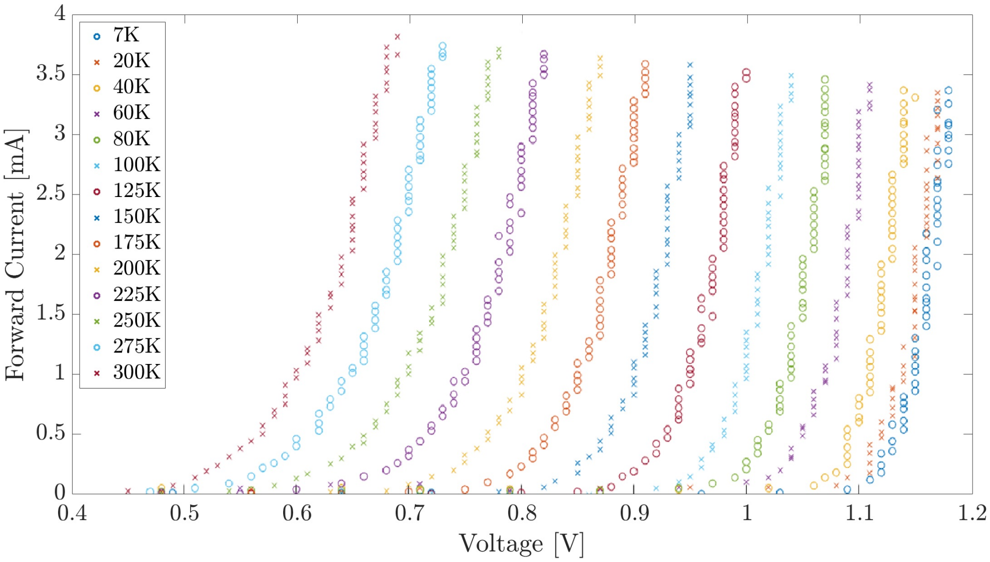

Figure 5.5: IV curve for the 1650 nm LED as a function of temperature.

To calculate the cut-in voltage[1], we excluded the data points where the current is less than 0.75 mA to only include the "linear" portion of the IV curve, then fitted the data to a line, as depicted in the left panel of Fig. 5.6. This figure shows the measurements at 7 K in green, 125 K in blue, and 300 K in red (a sample of three curves was selected for better visual comparison). The intersection between the fitted line and the x-axis is the value of the cut-in voltage reported in the right panel of Fig. 5.6 for all measured temperature points. Theoretically, in semiconductors such

---

[1] The cut-in voltage is defined in this case as the x-intercept value for the fitted line to the upper part of each IV curve (current above 0.75 mA).

as silicon, the change in cut-in voltage as a function of temperature is $dV/dT = -2.5\ mV/K$ [118]. The experimental value for our 1650 nm LED alloy of In, Ga, As and P found to be close to that and equals to -1.91 ± 0.18 mV/K.

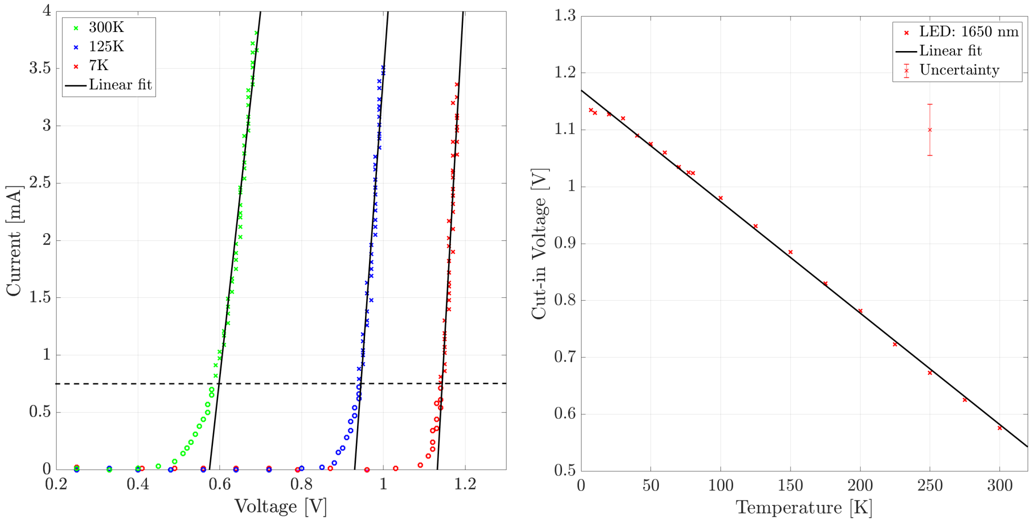

Figure 5.6: *Left*: Examples of the linear fit applied to calculate the cut-in voltage in the 1650 nm LED. Only 7, 125, and 300 K were selected for better visibility. *Right*: Cut-in values for the 1650 nm LED as a function of temperature. The error bar shown is the systematic uncertainty.

The slope of the linear part of the IV curve is the inverse of the diode's resistance, as depicted in the left panel of Fig. 5.7 [119]. The dependence on the duty cycle was investigated to understand its effect on possible self-heating of the LED at a temperature of 7 K [120].

When the duty cycle is low (at 5%, shown in red in the right panel of Fig. 5.7), the LED turns on while having enough time to thermalize between the on-times, and the effect of self-heating is minimal.

When the duty cycle is high (at 95%), the LED temperature is the nominal temperature when it turns on, but as the current continues to flow, the LED self-heats and the measured current averages over a range of temperatures; in contrast at a low

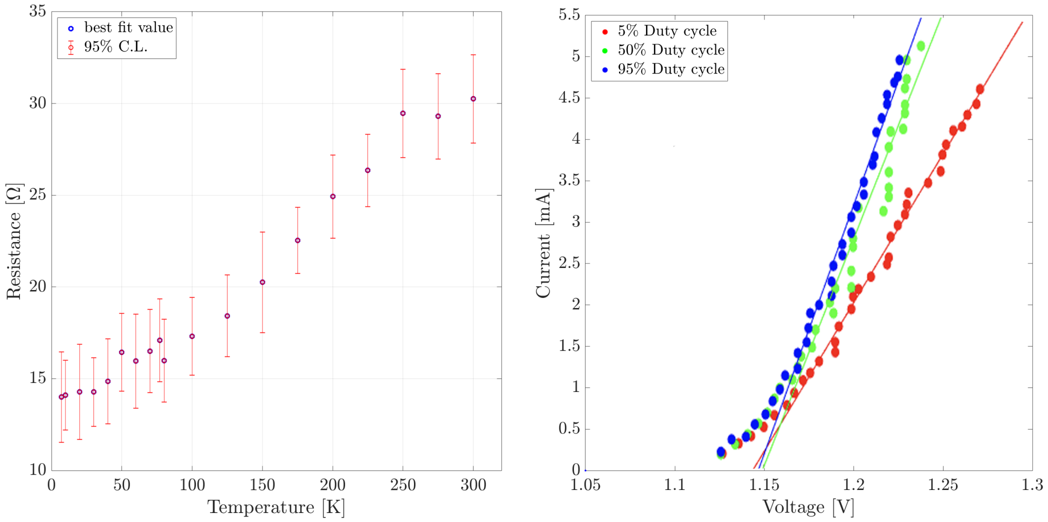

Figure 5.7: *Left*: The resistance values of the 1650 nm LED as a function of temperature. Points below the dashed line are excluded from the fit. *Right*: The line of best fit for IV curves at different duty cycles at 7 K.

duty cycle the self-heating effect is minimal. This effect can be seen in the right panel of Fig. 5.7, where the measured resistance decreases with an increasing duty cycle. This confirms that self-heating plays a significant role in the resistance measurements and the steepness of the line can not be interpreted (in this case) as the inverse of the resistance due to this effect.

5.2.9 Emission Spectra at Low Temperature

5.2.9.1 Spectra at Fixed Current

The LED spectra were recorded at each temperature point for two current values, 1 mA and 3.3 mA through the LED, as measured from the Arduino circuit. The 1 mA value was chosen as a random point where the LED is definitely on while the 3,3 mA value was the maximum current the Arduino circuit can provide. Moreover, another spectrum was also recorded at each temperature point while operating the

LED using a function generator putting out a pulse width modulated square-wave. LEDs were observed to emit shorter wavelengths as the temperature decrease.

For the 1650 nm LED with a continuous 1 mA and 3.3 mA current through the circuit, we observed a wide distribution of wavelengths covering a range of ∼350 nm at RT; there was a clear peak position, but the shape was non-Gaussian, with a long tail to shorter wavelength and the curve was fitted by two Gaussians. A similar spectrum was observed at low temperatures as well. A selection of spectra at four temperature points is shown in Fig. 5.8. The peak position reported here is the mean value of the first Gaussian. The standard deviation is shown as the error bars in Fig. 5.9. At RT, the recorded mean value was 1661±1 nm for both current values. After cooling down to 10 K, the measured value at the 1 mA current was 1542±1 nm, which corresponds to a change of 119±2 nm. The peak position for the maximum current measurement at 10 K was 1536±1 nm giving a difference of 125±2 nm from room temperature.

One interesting feature was observed when comparing the peak position at different temperatures. We saw a significant change in the peak emission between room temperature and 60 K, as shown in Fig. 5.9. However, the change is less evident at temperatures below ∼60 K, which suggests that for the LED to turn on, it has to reach a minimum temperature of about 60 K. So, cooling-down beyond this point has a minimal effect on the emission spectra.

5.2.9.2 Spectra in Pulsing Mode

We operated the LED in pulsing mode using a function generator, by sending a pulse width modulated square-wave and varied the pulse width and frequency, one at a time for the same temperature point, to study their effect on the emission spectra.

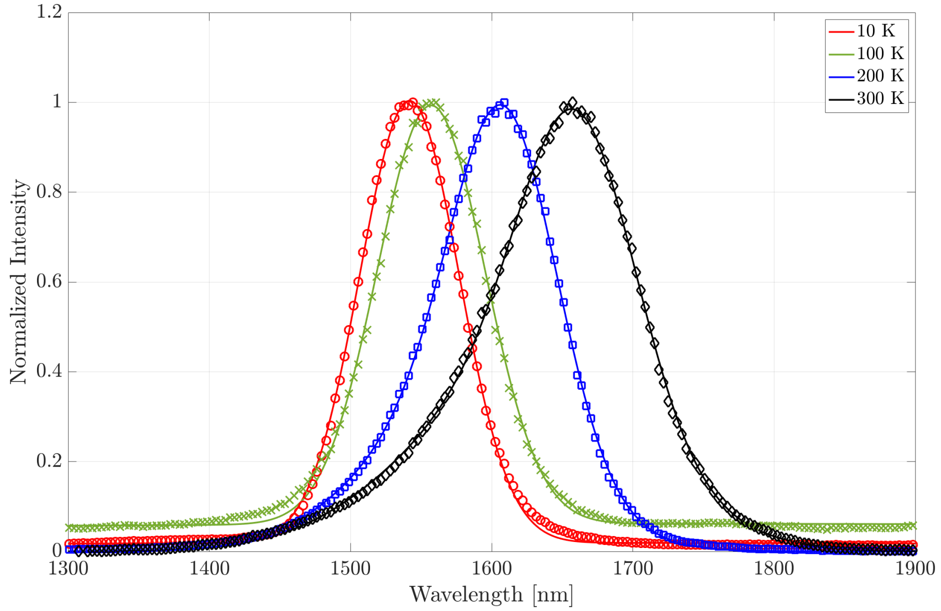

Figure 5.8: Example of the change in emission spectra from the 1650 nm LED when operated at 1 mA and various temperature points.

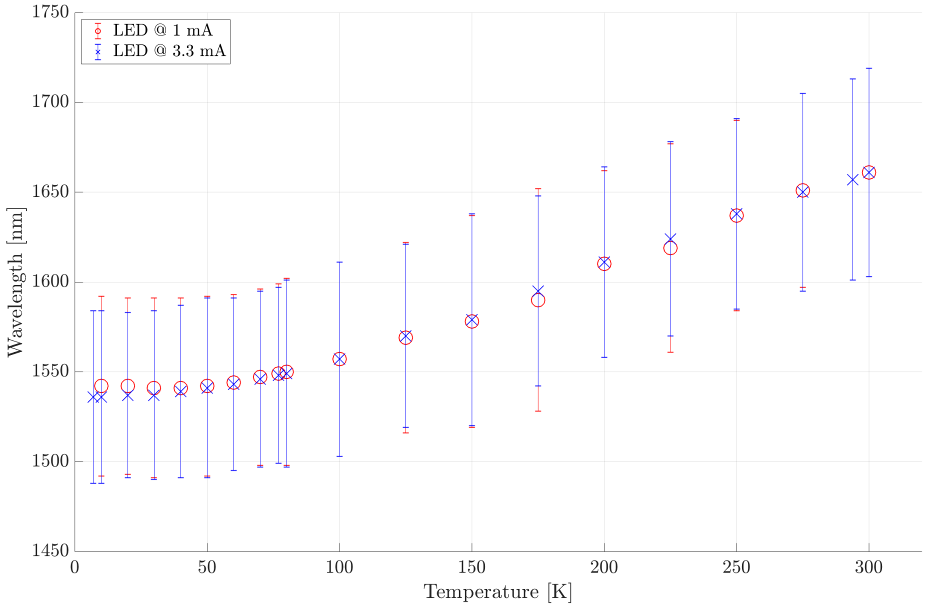

Figure 5.9: The change in peak emission of 1650 nm at various temperatures. Error bars are the standard deviation (width) of the first Gaussian.

First, the emission spectra were recorded at 7 K for three different pulse width values: 60, 70, and 80 μs while keeping the frequency at 100 Hz and V_{pp} at 1.5 V, as shown in the left panel of Fig. 5.10. Second, using V_{pp} at 1.5 V, we recorded the emission spectra for three frequency values: 50, 100, and 200 Hz, as depicted in the right panel of Fig. 5.10.

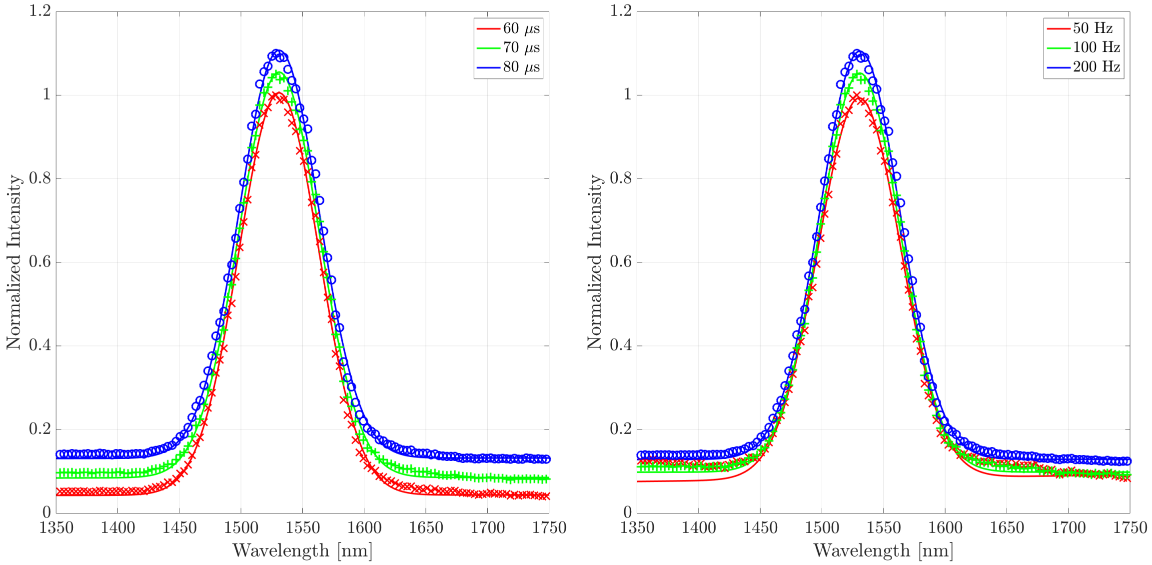

Figure 5.10: *Left*: Normalized spectra for the 1650 nm LED when operated in pulsing mode at 7 K for three different pulse width values and at fixed current and frequency. *Right*: The same LED when operated at fixed current and pulse width but changing the frequency at 7 K. In both plots, the data are shifted vertically for green and blue curves for better visual comparison.

5.2.10 Conclusion

The dependence of the energy gap on the temperature in semiconductors follows Varshni's formula and it has been reported earlier, e.g., in Ref [121]. We were interested in performing the IV and spectrometry tests on an LED of 1650 nm peak emission at cryogenic temperature because we wanted to find the exact peak emission at the low-temperature range. We were able to record the emitted spectra and to find the emission peak at various temperature points. These results will be further utilized in the measurement of the following sections in this chapter.

5.3 Internal LED - Quantum Efficiency Tests

5.3.1 Introduction

The term "Internal LEDs" refers to the standard 940 nm LED chips attached to the DIB (see section 3.5 for more details about detector packaging), while "External LEDs" refers to the ones being attached to the setup, as will be discussed later in section 5.4. We are planning to test the possibility of utilizing LEDs in performing detector stability tests as an alternative for the radioactive sources. Therefore, we started by measuring the energy and quantum efficiency[2] of IR photons then, compared that with well-known gamma sources in our setup. Afterward, we measured the amplification in IR signal when detectors were operated at a High Voltage (detectors are discussed in sections 3.5.2 and 3.5.1). LEDs have never been reported to be used in cryogenics for this purpose before, hence the stability of LED emission and pulsing near the emission threshold has never been reported and this study is the first to do that in SuperCDMS collaboration. In this section, we will list the key findings and propose several future tests.

5.3.2 Experimental Setup

After the conclusion of SuperCDMS operations at Soudan, the second detector tower, T2 (which includes detectors Z1, Z2 & Z3) was transferred to Queen's University to

---

[2] The quantum efficiency of a semiconductor can be defined by the average number of e^-/h^+ pairs resulting from the absorption of one particle at a given energy.

be used for detector studies and other R&D activities, such as the one described here.

In earlier preliminary tests, we found interference between the LED drive circuit and the phonon readout circuit when trying to operate the LED using the DCRC RevC board. In this test, we have the LED connected to isolated wiring throughout the fridge. At room temperature, we used an arbitrary-waveform function-generator, model Agilent 33210A, in pulsing mode, in addition to the simple circuit shown in Fig. 5.11 to operate the LED. Having those resistors in-line with the LED will reduce the current down to an acceptable range while the circuit is biased at the required operating voltage for low-temperature operation (between 6 and 8 V at 45 mK).

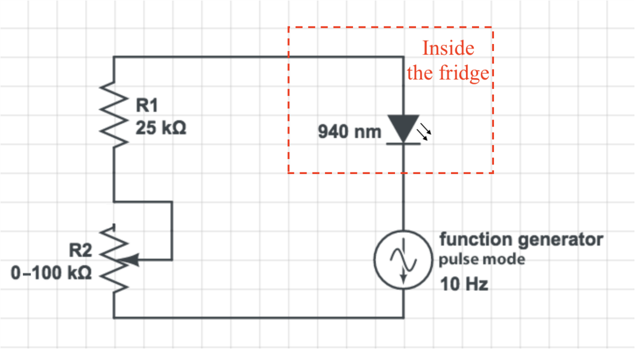

Figure 5.11: A simple circuit diagram for operating the internal LED.

The detector was operated in “a flat”[3] HV mode. This operation mode requires making some modifications to the phonon and charge channels for one of the two detector sides. These modifications are detailed in Appendix C.

---

[3] Flat E-field: is referred to the configuration when all sensors on one side were put at voltage while those on the other side were at the ground.

5.3.3 Methodology

The procedures followed during taking data were similar at each run; it started by flashing the detector for about a minute, then pre-biasing[4] for about 90 s before starting to take data. During regular flashing, the detector warms typically up to a few hundred millikelvins. For the tests here, the LED operating parameters were carefully adjusted to avoid any increase in the steady-state temperature of the detector, while still providing enough energy so the energy deposition in the detector could be measured.

The data reported in Table 5.2 were taken at the following settings: Function generator set in "Pulse" mode with frequency at 10 Hz, a pulse width of 100 μs and voltage of 8 V_{pp}. The value of the phonon signal resulting from NTL amplification for the γ photons in this data is calculated using $E_{total} = E_{recoil}(1 + \frac{eV_{bias}}{\epsilon})$, similar to Eqn. 3.1, where E_{recoil} is 60 keV for the ^{241}Am source and ϵ is 3 eV for germanium.

Fixed LED Settings				
V_{bias} [V]	$\gamma_{calculated}$ [keV$_t$]	$\gamma_{measured}$ [keV$_t$]	IR$_{measured}$ [keV$_t$]	$(\mathrm{IR}/\gamma)_{measured}$
3	120	120±8	144±4	1.2±0.5
15	360	351±13	387±5	1.1±0.4
30	660	660±29	590±3	0.89±0.1
60	1260	1215±73	1224±21	1.0±0.3
90	1860	1675±58	1760±9	1.1±0.2
111	2280	1920±67	2035±17	1.1±0.3

Table 5.2: The amplification of gamma and IR photons as a function of the detector's bias voltage. The error here is the standard deviation.

In the next test, we measured the total phonon energy while keeping the detector

---

[4] Pre-biasing: is performed by adjusting the bias voltage across the detector to a higher value, 10 V in this case, for a time period.

biased at 60 (111) V after pre-biasing at 70 (120) V for 90 s. The frequency was kept invariant at 10 Hz and the pulse width at 100 μs, while V_{pp} was changed to control the energy of the photon pulses, as listed in Table 5.3.

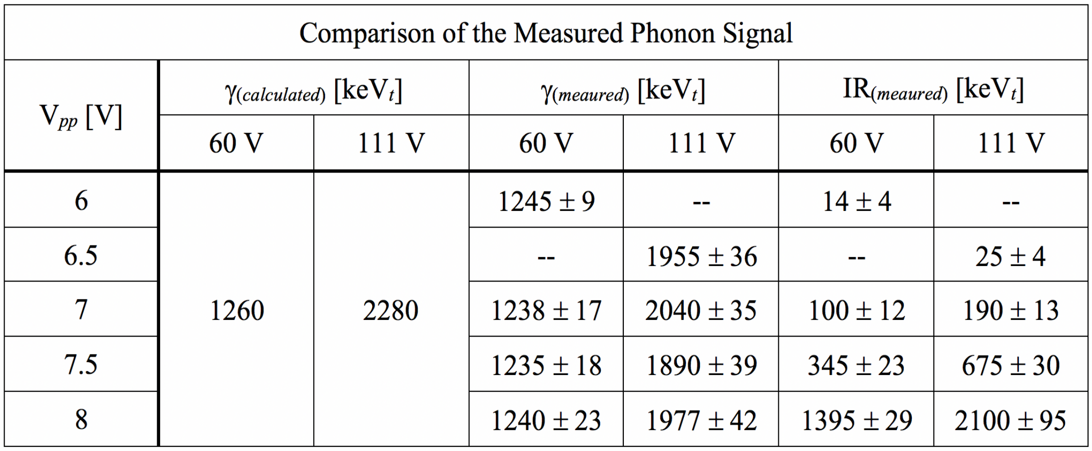

Comparison of the Measured Phonon Signal						
V_{pp} [V]	$\gamma_{(calculated)}$ [keV_t]		$\gamma_{(meaured)}$ [keV_t]		$IR_{(meaured)}$ [keV_t]	
	60 V	111 V	60 V	111 V	60 V	111 V
6	1260	2280	1245 ± 9	--	14 ± 4	--
6.5			--	1955 ± 36	--	25 ± 4
7			1238 ± 17	2040 ± 35	100 ± 12	190 ± 13
7.5			1235 ± 18	1890 ± 39	345 ± 23	675 ± 30
8			1240 ± 23	1977 ± 42	1395 ± 29	2100 ± 95

Table 5.3: The measured total phonon signal from the IR and gamma photon interactions at two different bias voltages across the detector, 60 and 111 V. The error reported here is the standard deviation.

5.3.4 Results and Future Studies

The data collected during this test demonstrates that we can operate the LEDs next to the detector while operating the detector (without causing it to warm up), and we can control the output so that the absorption in the detector is in our range of interest.

The results reported in Table 5.3 were aiming to quantify the least measurable energy of IR photons by keeping the same detector bias voltage while reducing the energy of LED pulses. We can see that the least measured energy was 25 (14) keV when the detector was biased to 111 (60) V and V_{pp} at 6.5 (6.0) V. This energy value

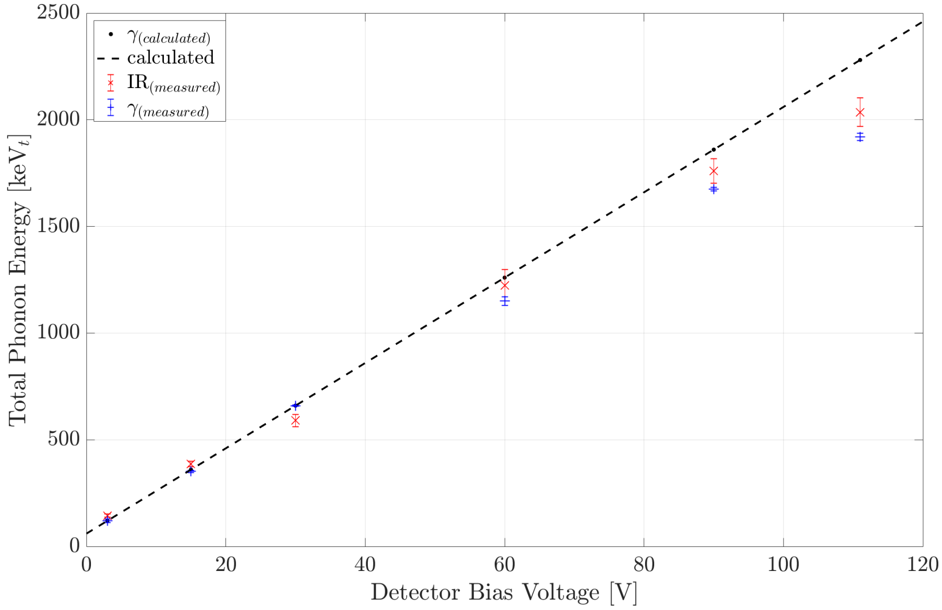

Figure 5.12: Total phonon energy collected as a function of bias voltage for gamma and IR events. The dotted line is the expected energy from the gamma photons. At high voltages, the measured phonon energy is less than the calculated and that might be related to the saturation in phonon sensors at high voltages. Error bars are the standard error.

at 111 (60) V corresponds to a pulse energy of 660 (665) eV when the detector is at $V_{bias} = 0$ V. This energy is well-below our detector energy threshold, therefore, can not be measured at 0 V. However, this energy is higher than the energy threshold of the new generation of SuperCDMS SNOLAB detectors [91], and similar tests can be performed in the future provided that, there will be no interference between the LED drive and the phonon circuit at the new generation of DCRC boards.

5.4 External LED Stability Tests (Non-collimated)

5.4.1 Introduction

Photons with energy above the direct bandgap of germanium have a very short penetration depth. Thus, these photons can only probe the detector response to surface events. On the other hand, photons with an energy below the direct bandgap have a lower interaction probability and thus, a considerably larger penetration depth. In this section, we discuss the use of LEDs with emission peaks at 1650 nm and 1550 nm and therefore have energies between the indirect and direct bandgap (see Fig. 5.1). The LEDs used here are of the same type (ceramic packaging) as the ones used for the measurements discussed in section 5.2. We have noticed that the LEDs are not durable because they start to crack after being cooled down once or twice. Therefore, this flaw was a limitation in repeating some of the measurements.

The measurements discussed in this section are used to estimate the penetration depth of photons (earlier measurements were performed using a 1550 nm LED with different setup are reported in Ref. [84]). In addition, we study the stability of the LED signal and the amplitude ratio between adjacent detectors to explore the option of producing well-controlled photon signals at very low energy.

5.4.2 Experimental Setup

The detector stack for this run contained two of the SuperCDMS detectors, T2Z1 and T2Z3, in addition to an ^{241}Am source to calibrate their energy scale. LEDs of nominal wavelength 1650 nm and 1550 nm [117] (at room temperature) were soldered to an empty housing, as depicted in Fig. 5.13, with their own wiring to room-temperature electronics to avoid any interference with the DCRC boards while taking data.

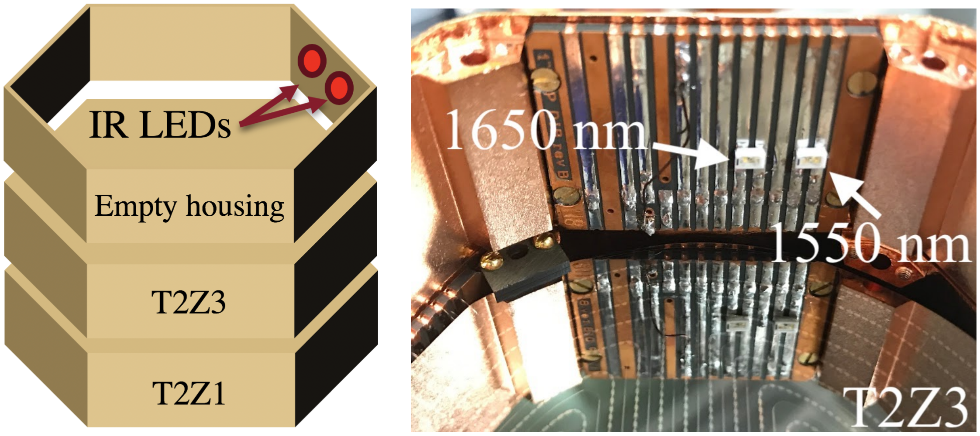

Figure 5.13: *Left*: A cartoon showing the arrangement in the detector stack. *Right*: The top part of the detector stack where both LEDs are soldered to an empty housing near the top side of detector T2Z3.

5.4.3 Methodology

At this run, we took several data sets at two different detector modes, HV and iZIP. We started by tuning the energy emitted from the IR source down to the threshold that the readout electronics can read. This corresponded to 3.9 V_{pp} at the LED, as depicted in Fig. 5.14. The detector was operated in iZIP mode at ±6 V (that is 12 V across the crystal) and the lowest measurable energy from LED pulses was about 4.0±0.2 keV.

We were interested in measuring the energy from IR events in both detectors, to study the signal stability and to give an estimate for the energy reduction, or what will be called here "Shadowing effect"[5]. The test of LED signal stability was performed by keeping the LED operational settings invariant while taking data for an extended time.

---

[5] *Shadowing effect*: is the reduction of the number of IR photons interacting with the detector that is farther away from the LEDs (Z1) due to the presence of the nearer detector (Z3).

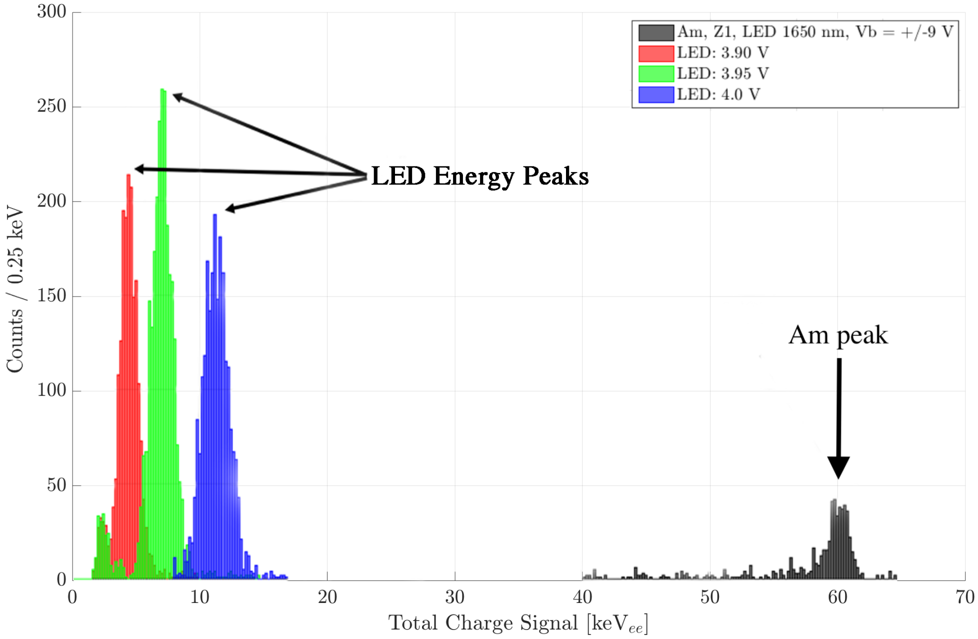

Figure 5.14: A histogram for the total charge collected in charge electrodes. The energy of IR pulses is calibrated via 60 keV peak (in black) from an ^{241}Am source. The lowest energy peak (in red) shows the least measurable IR pulses. Other peaks at higher energy are shown as well (green and blue). The LED drive circuit in this measurement was different than that in section 5.3. Hence, the voltage across the LED is also different.

5.4.4 Results and Future Tests

By comparing the signals from the two detectors, we can quantify the shadowing effect for this setup. The signal ratio between the detectors was very large, so the range of LED settings where both detectors see a well measurable signal is rather small. Since the shadowing is a purely geometrical effect, the signal ratio does not depend on the signal amplitude. Thus, we can use the energy deposition in the near detector to predict the signal amplitude in the further one. Therefore, in the plot shown in Fig. 5.15, we extrapolated the energy scale to show what energy is expected once the setup is ready to perform this measurement at a lower energy range.

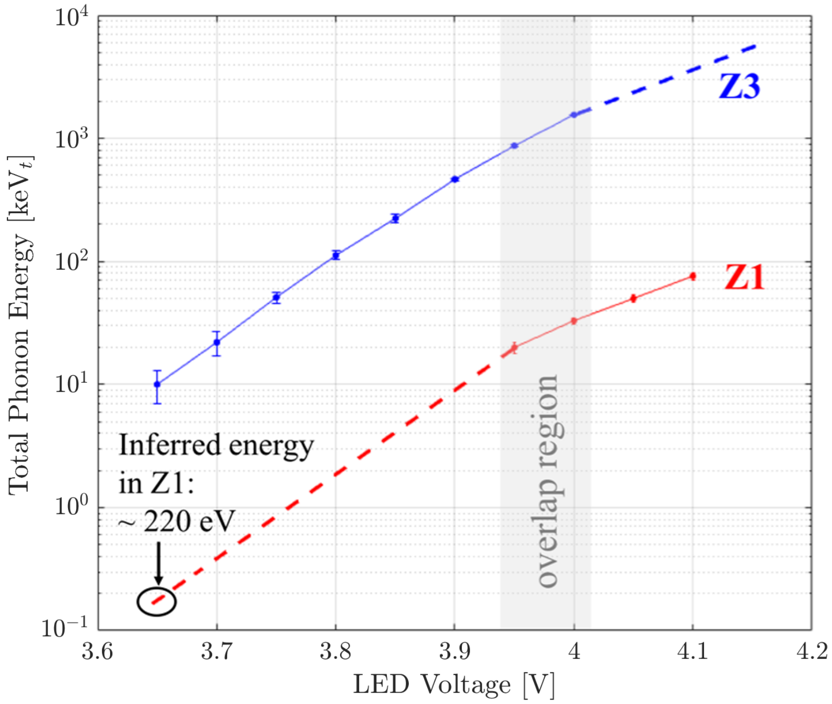

Figure 5.15: Total phonon energy as a function of LED bias voltage for detectors Z1 and Z3 while operated at 0 V.

In Fig. 5.15, the solid lines, red and blue, is a linear fit for the measured energies. While the dashed lines are the extrapolation (expected) phonon energy at the corresponding LED bias. The ratio between the two measured energies in both detectors was calculated to be 45.3±1.8 and should remain invariant (for this setup) because it depends on the geometry of the stack of detectors as well as the LED wavelength, which are invariant in this case. For LED voltages above 4.0 V in Z3, all phonon channels were saturated and below 3.95 V the energy is below our threshold in Z1. The highlighted overlap region is the region where we could turn the LED on and be able to measure the phonon signal in both detectors. The value 220 eV indicated in

Z1 is the inferred energy once our electronics and detector can achieve that limit.

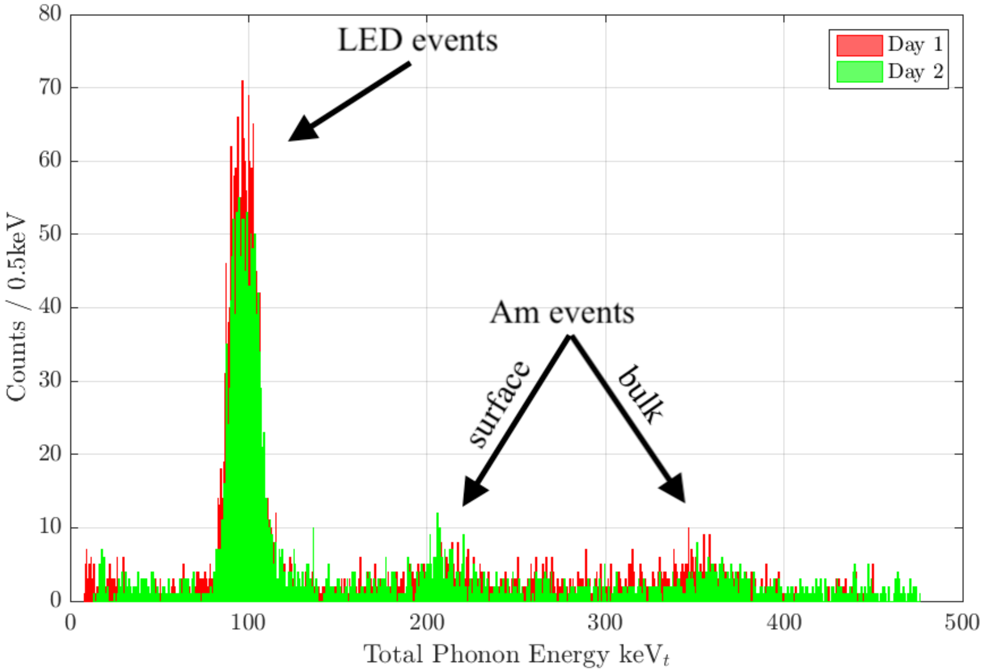

Figure 5.16: A histogram for the total phonon energy in Z3 when operated in iZIP mode on two consecutive days at ±9 V (see text above for details).

One of the key findings of this test is presented in Fig. 5.16 where we used the 1650 nm LED pulses to test the stability. The detector was operated in the same configuration (iZIP, ±9 V) and the LED was operated with the same parameters (3.95 V$_{pp}$, 14 Hz and 120 μs pulses) on two consecutive days.

Besides the LED peak, we see two more peaks at higher energy. They both stem from interactions of 60 keV photons from the ^{241}Am source; the higher one is from bulk interactions and the lower one from near-surface interactions where, due to the electric field configuration, the NTL amplification is only half of that for bulk events. The overlap of the two Am peaks demonstrates that the detector itself was stable over time, so the fact that also the two LED peaks overlap shows that the LEDs output is stable over an extended period of time if the same operational parameters were used.

The last set of measurements were performed at the LED frequency of 14 Hz, pulse-width of 120 μs. In this test, the 1550 nm LED was operated with voltages of 3.90, 3.95 and 4.00 V$_{pp}$ and the detector was biased at ±6 V while the 1650 nm LED was operated with voltages of 4.70, 4.85, and 5.00 V$_{pp}$ with a detector bias of ±9 V. The results of the penetration depth are discussed in the following section for a better comparison of results.

5.5 External LED Tests (Collimated)

5.5.1 Introduction

The measurements of this section are motivated by the results from section 5.4 and they aim to calculate the attenuation in the LED pulse energy between the near detector (Z2) and an adjacent one (Z1) over an extended range of energies to confirm the ratio for the shadowing effect, keeping in mind that shadowing is strongly dependant on the setup geometry. It also aims to provide a study for the difference between the collimated and the non-collimated LED signals where the main interest will be measuring the charges collected at each side of the detector to estimate the penetration depth of IR photons in our crystal.

The position of LED events indicates that the interaction of both photons, 1550 nm, and 1650 nm, has the same penetration depth, besides that, all interactions occur at the bulk of the crystal. However, this contradicts with our previous measurement for the 1550 nm when the LED was operated at room temperature, see Fig. D.1 in Appendix D. Moreover, there should be a significant difference between the penetration depths of the 1550 nm and 1650 nm photons, which is not the case here. So, that was an indication that photons are bouncing around "inside the detector housing" and interact at both sides of the detector, thus giving charge signal on both sides, as shown in Fig. 5.17.

For this reason, we changed the setup (compared to the previous section) for a better estimation for the absorption length and built a collimated LED source after we have confirmed the emission spectrum of the LED at cryogenic temperatures (the measurements discussed in section 5.2).

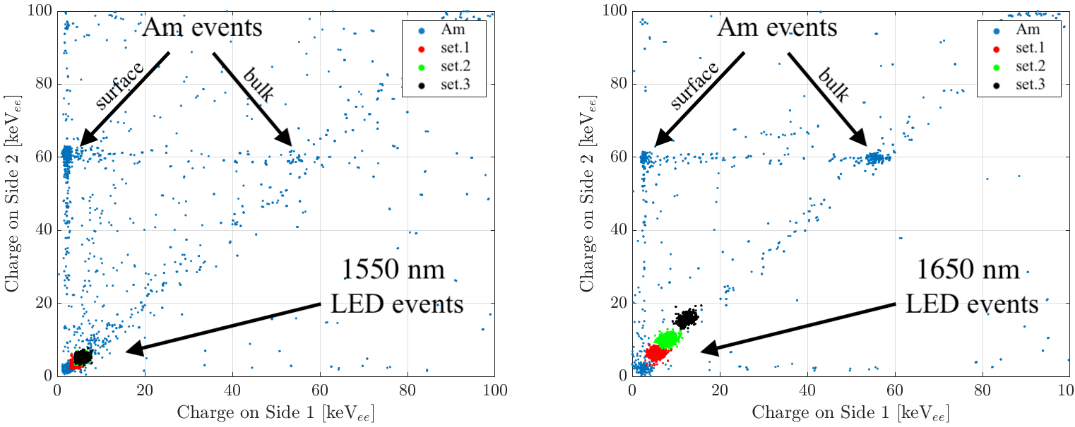

Figure 5.17: *Left*: Charge signal of side 2 vs side 1 for a 1550 nm data. *Right*: Charge signal of side 2 vs side 1 for a 1650 nm data. The different blob colors (red, green, and black are for different LED operational settings.

For the penetration depth, the initial idea from using the 1650 nm is to have photons with relatively long absorption length (relative to the 1 inch-thick detectors) which should result in mostly bulk events. Then, at this run, we needed to confirm the previous findings in addition to compare the absorption length of both, 1550 nm and 1650 nm.

5.5.2 Experimental Setup

For this run, a 1650 nm LED (peak emission at low temperature is at 1540 nm as discussed in section 5.2) was installed outside the detector housing, and photons were transmitted through a 1 mm wide and ∼3 cm long collimator ending ∼3 mm from the detector surface; the setup is depicted in Fig. 5.18.

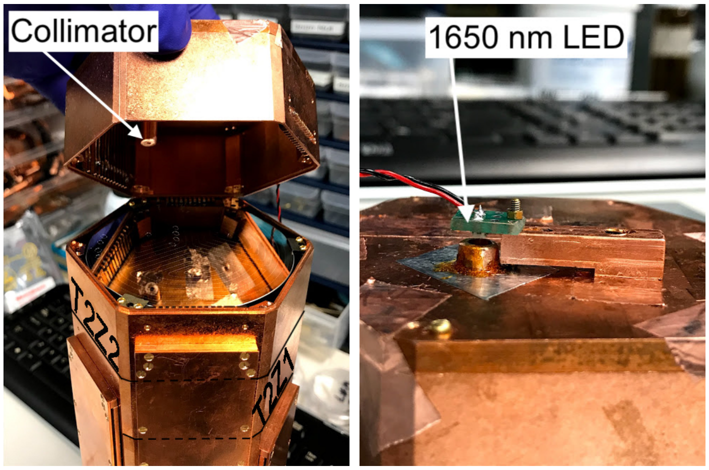

Figure 5.18: *Left*: The detector stack (Z2 at the top of Z1 with a black line added to visually differentiate detectors) and a 1 mm collimator pointing at the top surface of Z2. *Right*: A 1650 nm LED attached to a PCB and pointing downwards at the collimator.

5.5.3 Emission Spectra and Absorption Length

The absorption length for 1650 nm photons in Ge has been measured in the context of the EDELWEISS-II experiment and was reported to be 17 cm at 17 mK [110]. On the other hand, experimental data published in Ref. [122], reported the measured absorption length, in a pure germanium crystal, at various temperatures over a range of photon energies concluded a different value, as depicted in Fig. 5.19. The measured emission peak for the 1650 nm reported in section5.2 was 1542 nm (0.804 eV) at 7 K, once we map that over the absorption plot (the red dashed line in Fig. 5.19), we can estimate the absorption coefficient to be $\alpha \approx 2.5\ \mathrm{cm}^{-\frac{1}{2}}$. So, the absorption length will be ∼0.16 cm. This value (∼0.16 cm) is in agreement with the estimated absorption length measured in our detector.

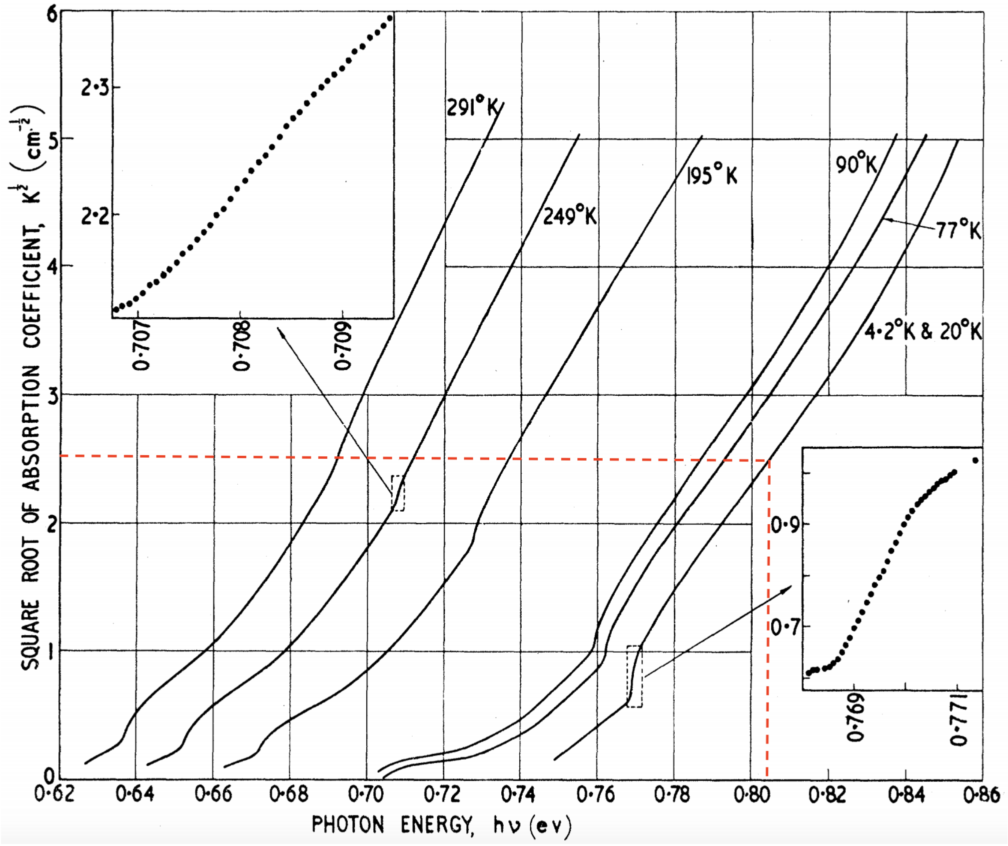

Figure 5.19: The absorption coefficient for germanium as a function of photon energy at different crystal temperatures. Image modified from the source where a red dashed-line is added to indicate the energy at 0.804 eV on the x-axis with the corresponding absorption coefficient.

5.5.4 Results and Future Studies

By comparing the charge signal on both sides from the top-detector in the stack (Z2), with that from the lower one (Z1), we observed that it is strongly asymmetric in Z2, which is proof for short penetration depth. This is shown in Fig. 5.20. The LED signal in Z1 (at the bulk of the detector) indicates that these interactions must have been occurred on the surface of each side due to the bouncing photons, rather than a long penetration depth to Z1 through Z2.

The spread of LED events, shown in the left panel of Fig. 5.20, is related to interference between the LED signal and a 60 Hz noise from the power source. We have tried to reduce the noise effect by operating the LED at selected frequencies and adding a high-pass filter to the LED drive circuit to decrease the spread in the LED spectrum as much as possible.

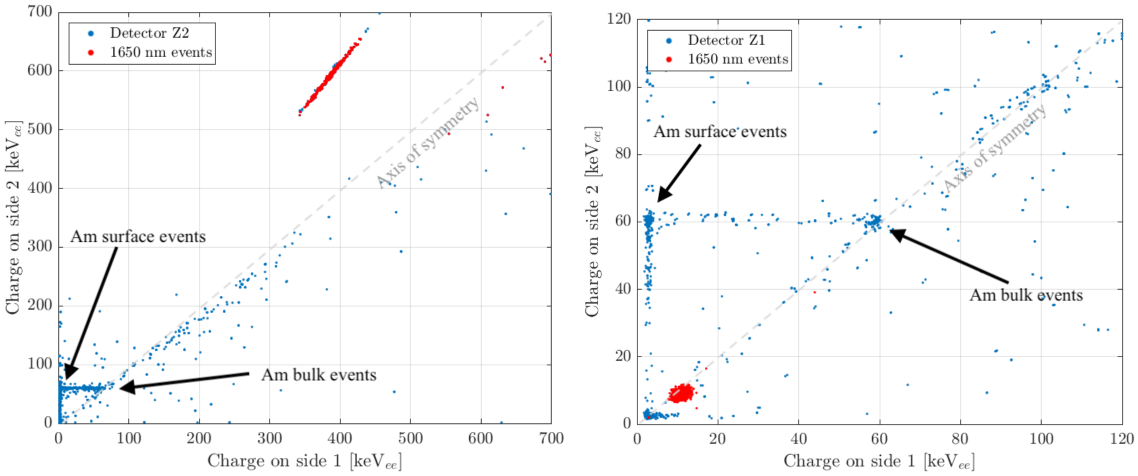

Figure 5.20: An ^{241}Am source was used to calibrate the energy scale of the plot for two different LED settings (different pulse energy). *Left*: Charge collected on both sides of the top detector (Z2), where events from the 1650 nm LED are highlighted in red. *Right*: Charge collected on both sides of the bottom detector (Z1)(see text for more details).

Unlike radioactive sources which produce localized energy depositions, irradiation with LEDs produces e$^-$/h$^+$ pairs at an extended surface area of the detector. On the other hand, the use of collimator has confirmed that what was observed earlier, when the LEDs were operated inside the empty detector housing (as shown in Fig. 5.13), was mostly resulting from photons being reflected by the within the detector setup and making their way to the bottom detector-surface and increased its charge signal.

In terms of the possibility of applying the shadowing effect for future calibration use at SNOLAB, we have also taken several data sets in each detector at identical LED settings, as listed in Table 5.4, where we changed V_{pp} while the pulse width and the frequency were fixed at 120 μs and 14 Hz. The ratio between the measured deposited energy in each of the two detectors is depicted in Fig. 5.21.

Shadowing Effect - LED Settings			
V_{pp} [V]	Z2 [keV$_t$]	Z1 [keV$_t$]	(Z2/Z1)
7.2	215±3	–	–
7.4	285±4	18±4	15.8±0.8
7.6	355±5	23±6	15.4±0.7
7.8	460±3	30±6	15.3±0.8
8.0	550±4	35.5±5.1	15.5±0.6
8.2	670±3	43.5±5.5	15.4±0.7
8.4	801±4	50.5±5.2	15.9±0.6
8.6	932±3	59.0±6.2	15.8±0.6
8.8	1073±2	68.5±5.5	15.7±0.5
9.0	1206±3	75.5±4.3	16.0±0.5
9.2	1359±4	85.5±4.5	15.9±0.7
9.5	1576±5	101±6	15.6±0.7

Table 5.4: A list of LED settings used while measuring the phonon signal at Z1 and Z2. The detectors were operated here at 0 V. At $V_{pp} = 7.2$ V, the energy in Z1 was below our threshold. The error value is the error in the mean.

In the future, SuperCDMS SNOLAB experiment, the detector geometry, and setup will be different compared to the setup of this measurement. Therefore, the attenuation will definitely have a different ratio. However, this method can still be applicable at SNOLAB once we are able to have a good calibration in the energy

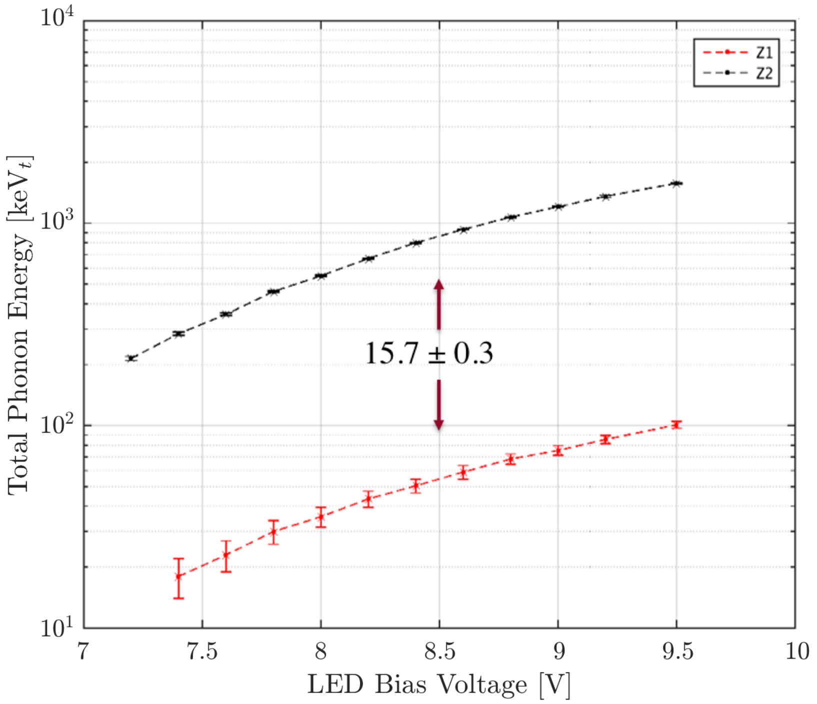

Figure 5.21: The total phonon energy collected in Z1 (red marks) and Z2 (black marks) while operating a 1650 nm LED as a function of the bias voltage (pulse energy).

range of 1 to 10 keV and we can apply similar procedures to calibrate adjacent detectors in the stack. We can utilize the LED signal and produce an interaction at the near detector (near to the LED) while being able to see the same signal at the far detector to find the corresponding attenuation ratio. Then we can repeat the process between different detectors to get a scheme for the attenuation ratio for the stack of six detectors. This can eventually provide us with an absolute energy calibration scheme for the whole stack.

If the performance of the new SuperCDMS detectors is at the upper end of the anticipated range, the resolution might be good enough to detect individual e^-/h^+ pairs. In this case, an absolute calibration would be possible if the photon flux could be reduced enough, so that each pulse only contains a small number of photons. Unfortunately, the available setup (detectors and readout electronics) can not reach such a performance, so this scheme could not be tested. However, in the next section, we initiated such steps by demonstrating that it is conceivable to produce a small enough photon flux with an LED at a low temperature.

5.6 HVeV Detector Tests at Queen's

5.6.1 Introduction

The HVeV detector we used is made of a silicon substrate of size $1\times1\times0.1$ cm^3 and ~0.25 g mass with about ~80% Aluminum surface coverage. The detector has no biasing electrode and the bias is applied to an external electrode - and therefore the actual bias across the detector is not known precisely.

This detector has been tested earlier at Northwestern University, and the results were published in Ref. [98]. In this publication, the detector was calibrated with photons from a laser diode. The laser was operated at room temperature and the photons were brought into the cryostat via an optical fiber, then the actual bias voltage was calculated by measuring the signal amplification over a range of voltages.

Our goal here is to use photons from an IR LED operated inside the cryostat to calibrate this detector and to show the feasibility of utilizing LEDs for such purposes. This opens an easier way to calibrate such detectors, and at the same time, it demonstrates that it is possible to operate an LED next to an eV-sensitive detector, without disturbing its performance. Furthermore, we were able to generate a photon signal that is small enough to generate individual e^-/h^+ pairs in the detector.

5.6.2 Experimental Setup

The HVeV detector was installed inside an empty 3-inch detector housing, then optically isolated from IR radiation with a housing lid and copper tape. An LED of a nominal wavelength of 890 nm was mounted onto a small PCB and attached at the lid, with a tiny hole of ∼0.2 mm in diameter to irradiate the detector, as depicted in Fig. 5.22. A closer look at the chip mask design is shown in Fig.5.23 to view the Al coverage at the detector's surface. The LED had its own wiring up to the room temperature electronics. An arbitrary-waveform function generator (Agilent 33210A) was used in pulsing mode to operate the LED and a generic power supply to bias the detector up to 121 V.

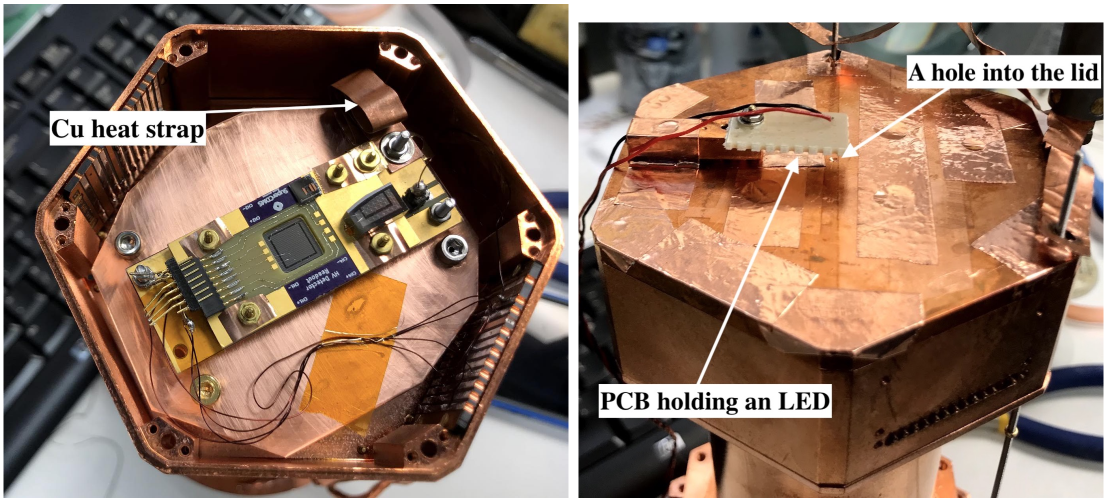

Figure 5.22: *Left*: Si HVeV detector is installed inside a 3-inch SuperCDMS detector housing with extra Cu heat strap to improve heat-sinking. *Right*: The detector lid covered at the top with Cu tape; a hole of ∼0.2 mm diameter allows the photons to reach the detector surface.

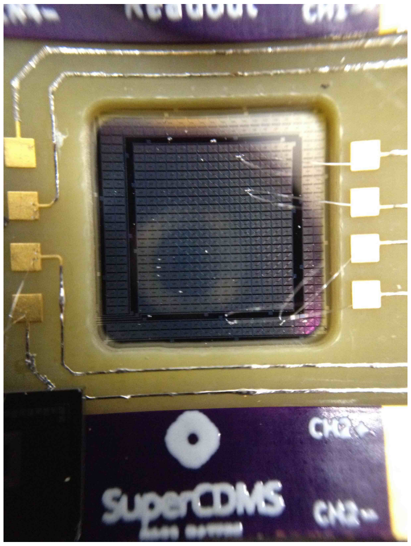

Figure 5.23: A closer look at the detector surface to show the highly Al surface coverage. Image courtesy Wolfgang Rau.

5.6.3 Data Acquisition

The detector was cooled down to ∼20 mK, then neutralized by flashing it with a 1.4 eV (890 nm) photons at the beginning of the run for about 3 hours. Data have been collected over a period of few days at different bias voltages between 0 and 121 V while keeping the LED settings invariant at a frequency of 12 Hz, the pulse width of 100 μs and a bias voltage of 4.1 V.

5.6.4 Data Quality Cuts

We have used several quality cuts to exclude bad data periods. Initially, we started by removing fluctuations in the baseline caused by changing the bias voltage. A phonon χ^2 cut, which is used frequently in SuperCDMS data analyses to filter-out bad pulses with high χ^2 events. In our data, the energy estimator is worse at low energies than at high ones. Therefore, the χ^2 cut is designed to be more strict at low energies while it has more tolerance of high χ^2 at high energies. In Fig. 5.24, the events highlighted in red have a low χ^2 and pass the cut, while blue events are filtered out. This results in a quadratic function where all events above the finely-tuned function are excluded.

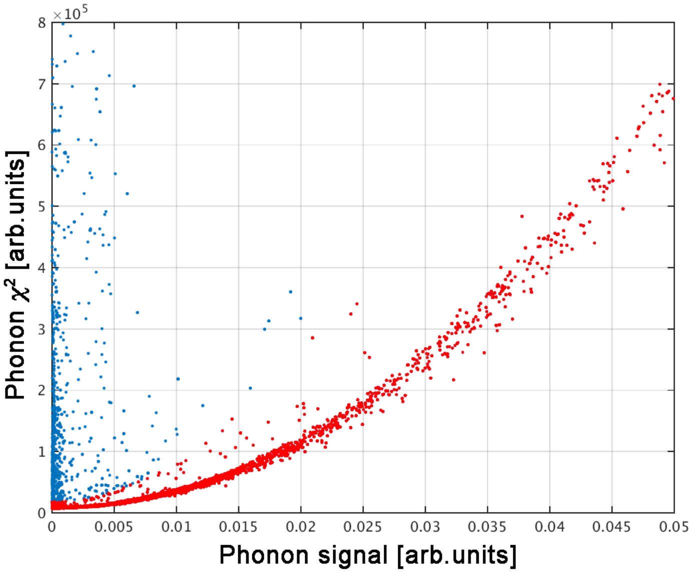

Figure 5.24: An example for the χ^2 cut applied to phonon signal. Red events have a low χ^2 and pass through the cut while blue events are filtered out.

5.6.5 Data Processing

Knowing that our regular processing procedure will not lead to usable results because we had many pile-up events in this case. Adam Mayer has generated a noise PSD for each run, then created a template for each one of the two channels of the detector. Afterward, he applied an optimal filter formula to individual pulses to determine the fit parameters (such as the amplitude and χ^2). Finally, the parameters were used to minimize the χ^2 with respect to the amplitude in the frequency domain.

5.6.6 Results and Future Work

At 0 V, the only observed peak was the offset. This peak is related to a number of photons hitting the Al fin and does not get amplified. Thus, they are not affected by the change in the detector's bias voltage, and that explains the fixed position of this peak as the voltage changes. The ratio of these events in the offset peak is relatively high due to the high Al surface coverage, as shown earlier in Fig. 5.23.

Then, at 45 V, we could observe another peak of the single e^-/h^+ pair events. As the applied voltage increases, the amplification of the phonon signal increase due to the NTL effect [99] and the peaks in the spectrum move to the right, as depicted in Fig. 5.25, Fig. 5.26 and Fig.5.27 for the voltages from 45 to 121 V.

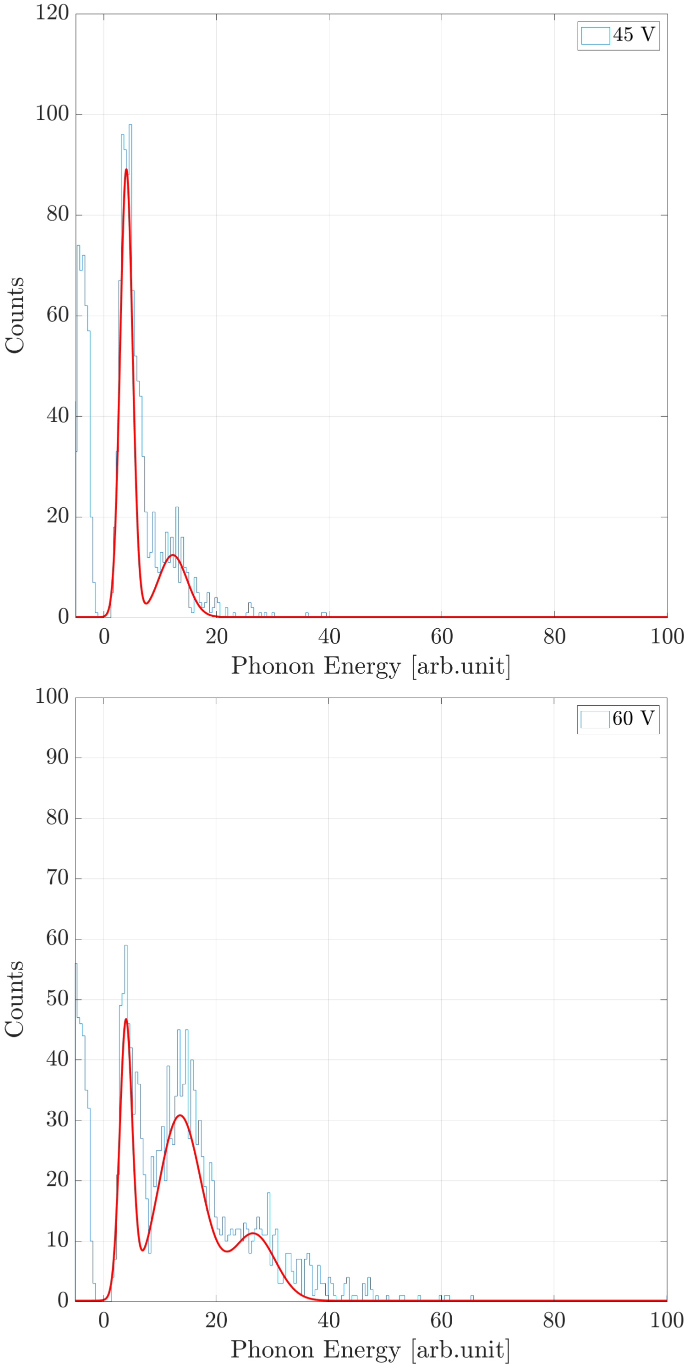

Figure 5.25: Energy spectra from HVeV detector for bias voltages 45 and 60 V(see text for more details).

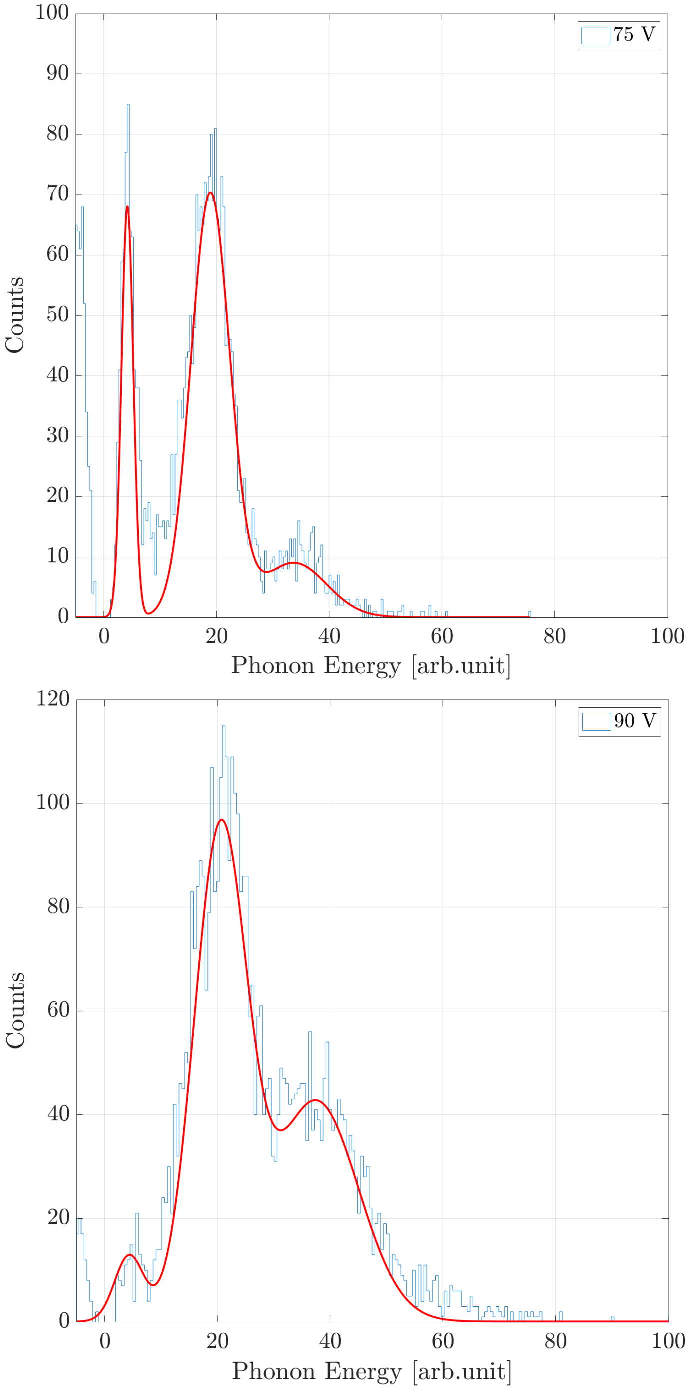

Figure 5.26: Energy spectra from HVeV detector for bias voltages 75 and 90 V (see text for more details).

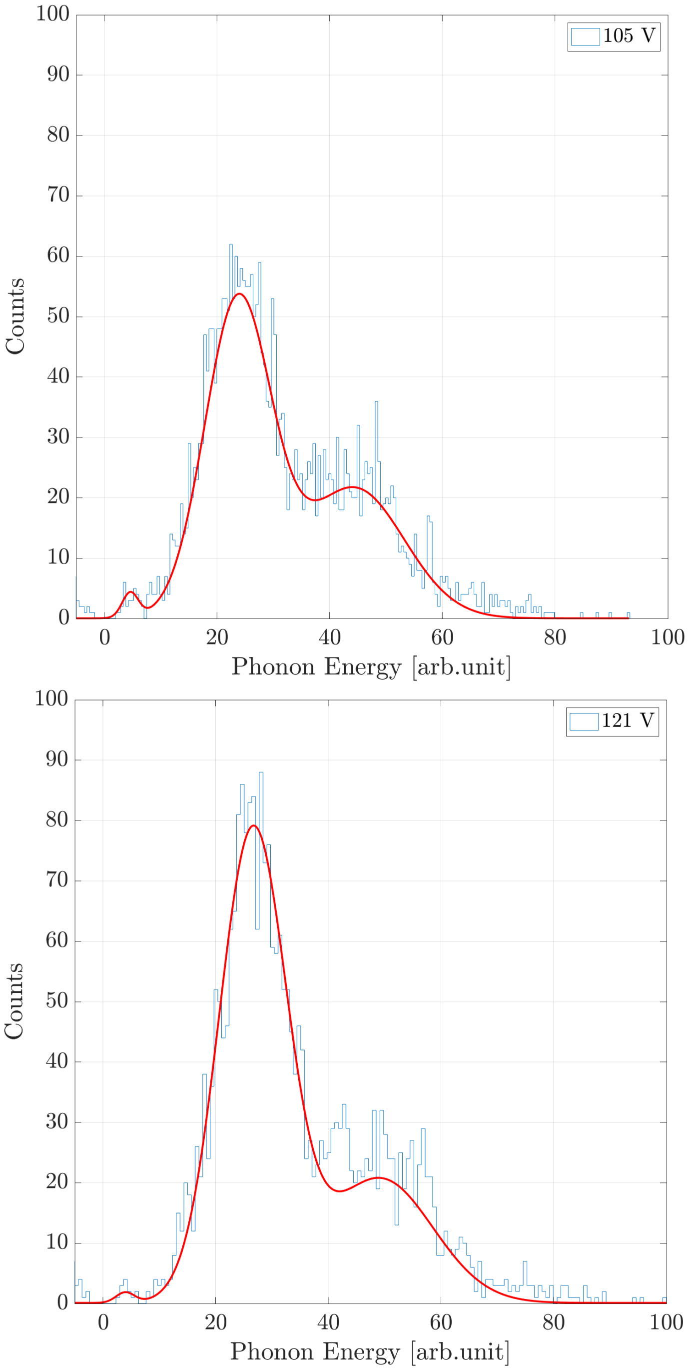

Figure 5.27: Energy spectra from HVeV detector for bias voltages 105 and 121 V (see text for more details).

Fit Parameters

Table. 5.5 below lists the fit parameters for the different peak positions for each applied voltage. The μ is the mean position and σ is the standard deviation of the fit. The index (0) is for the offset peak while 1 and 2 are for the first and second peaks, i.e. one and two e^-/h^+ pair peaks.

Applied Voltage	Fit Parameter					
	μ_0	σ_0	μ_1	σ_1	μ_2	σ_2
0 V	3.900±0.003	0.551±0.001	--	--	--	--
30 V	4.098±0.004	1.195±0.005	--	--	--	--
45 V	3.989±0.001	1.100±0.001	12.246±0.033	2.539±0.034	--	--
60 V	4.001±0.003	1.093±0.004	13.574±0.013	3.880±0.016	26.782±0.053	3.992±0.064
75 V	4.200±0.002	1.051±0.002	18.904±0.004	3.454±0.005	33.675±0.072	5.667±0.095
90 V	4.433±0.043	2.469±0.046	20.502±0.004	4.706±0.004	37.509±0.014	7.496±0.019
105 V	4.600±0.106	1.215±0.130	23.674±0.012	5.903±0.012	44.294±0.042	9.012±0.057
121 V	4.215±0.159	0.686±0.211	26.609±0.008	6.013±0.008	49.134±0.042	9.404±0.061

Table 5.5: The fit parameters for plots in Fig. 5.25, 5.26 and 5.27 in addition to two more data sets at 0 and 30 V where the offset peak was only observed.

To correlate the position of each peak with the voltage, we plotted the mean value against the applied voltage[6] in Fig. 5.28. The y-intercept of the linear fit provides the ratio between the applied and bias voltages. However, in this case, we had a negative y-intercept value for the measurements in positive polarity. This might be related to insufficient detector neutralization time prior to taking data. Therefore, we used a value reported for the same detector in earlier measurements performed at Northwestern University.

---

[6] The bias voltage across the detector is less than the applied because the HVeV detector is floating.

For the negative polarity measurements, the amplification of the phonon signal is not comparable to that in positive polarity. This might be related to some residual charges in the detector because the detector was not neutralized after performing the positive polarity. Consequently, an internal counter-field may have existed in the crystal. These measurements could not have been repeated and the statistics were low due to limited cryostat availability at QTF.

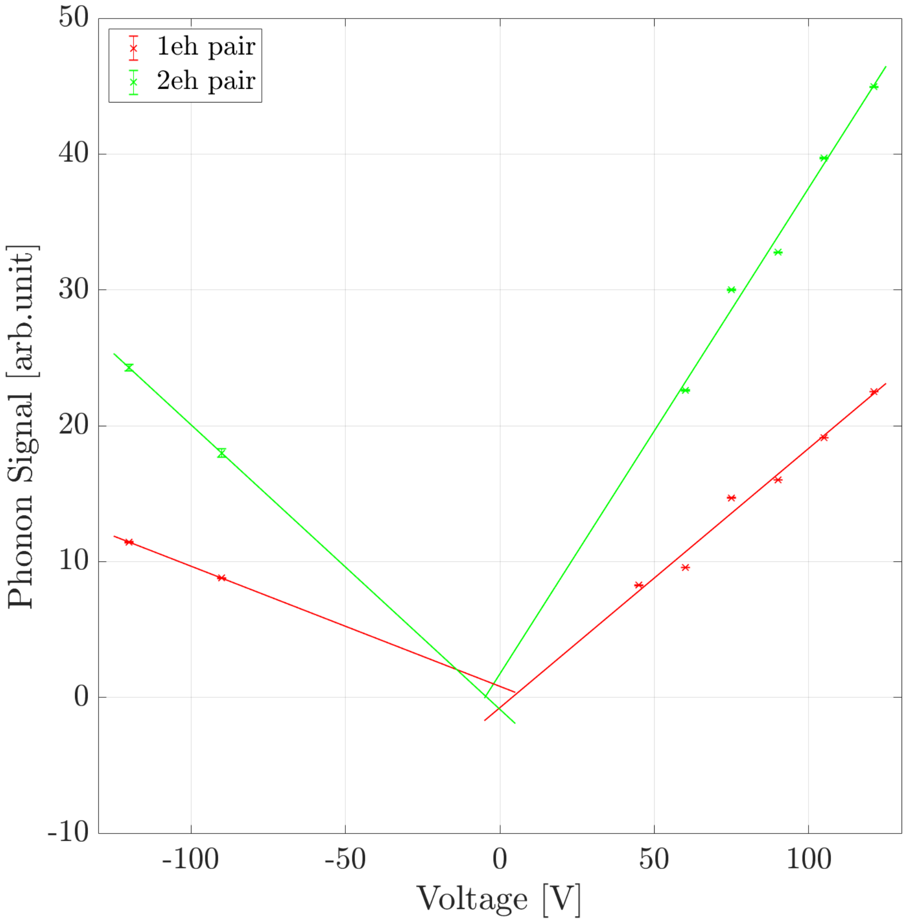

Figure 5.28: The mean value for single (in red) and double (in green) e^-/h^+ peaks as extracted from the Gaussian fit vs. applied voltage. Error bars are the standard error of the mean.

Energy Scale and Resolution

To calculate the total phonon energy, E_{total} of the n^{th} e^-/h^+ peak as a function of voltage we use: $E_{total} = E_o + n(E_{photon} + eV_{bias})$, where E_o is the energy deposited by photons that are absorbed in the sensor and thus do not produce e^-/h^+ pairs, n = 1, 2 or 3, is the number of e^-/h^+ pairs in the interaction, E_{photon} is the energy from the photon source and equals ~1.5 eV in our case[7], and V_{bias} is the bias voltage and equals to $V_{bias} = V_{applied} \times c$, where c quantifies the fraction of this voltage that drops off across the detector due to the vacuum gap between the electrode and the detector. For this analysis, we used c = 0.31, which is the factor calculated earlier (by R. Ren, SuperCDMS internal documentation) for the same detector.

If c (and thus V_{bias}) is known, we can use the measured slope S_n of the n^{th} e^-/h^+ pair peak position listed in Table .5.6, to calibrate our output signal $A_{measured}$:

$$E_{measured} = \frac{A_{measured} \times n \times e \times c}{S_n}$$

the total energy can be expressed in terms of the recoil energy as:

$$E_{total} = E_o + E_{recoil} + n\ e\ c\ V_{applied}$$

where $E_{recoil} = n\ E_{photon}$. With the above calibration factor we can convert the measured widths of the peaks into an energy resolution.

Fig. 5.29 shows the resolution in (eV) as function of applied voltage. To convert that into units of e^-/h^+ pairs, we can divide the peak energy over the bias voltage across the detector. From this figure, we can see that the best phonon resolution for the first e^-/h^+ peak was ~4 eV at 45 V, while for the double e^-/h^+ peak was ~6 eV at

---

[7] The LED wavelength is 890 nm which is equal to 1.4 eV at room temperature. However, we found earlier in this chapter that the spectrum shifts by about 10% when the LED is operated at cryogenic temperatures.

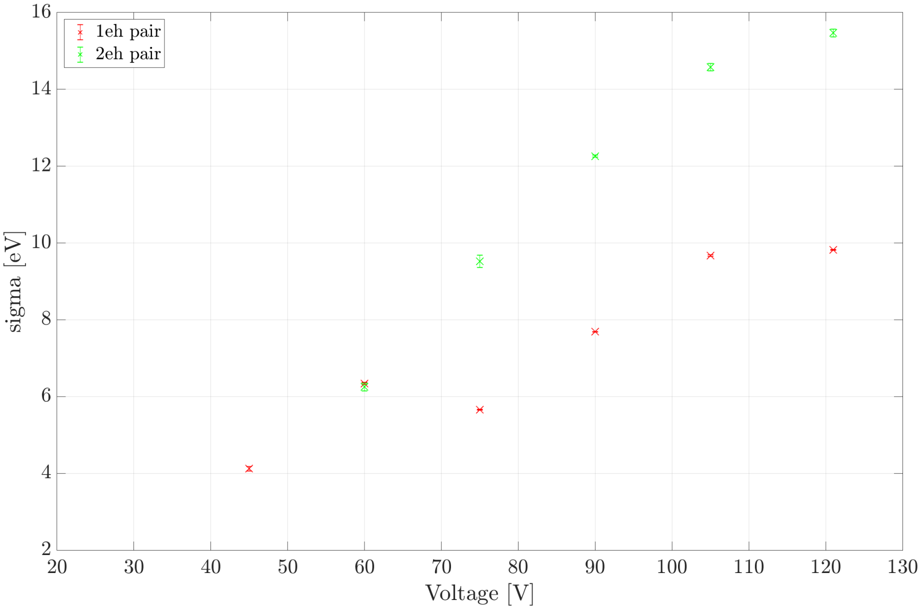

Figure 5.29: The phonon resolution of the first and second e^-/h^+ peak in eV. The best phonon resolution was at 45 V (60 V) for the first (second) peak.

Measurement Type	Slope	Y-intercept
One e^-/h^+	0.1894/V	-0.759
Two e^-/h^+	0.3474/V	1.727

Table 5.6: The linear-fit parameters of the positive bias (from Fig. 5.28).

60 V. On the other hand, the same detector had achieved a better phonon resolution of 4.0 (3.4) eV at +100 (-100) V, when it was operated at Northwestern University. The variation between the two measurements is referred to as the difference in the readout electronics where extra noise exists in our readout electronics

5.6.7 Suggestions for Future Measurements

So far, we have shown that LEDs can be operated close to detectors with eV sensitivity without disturbing them. We have also shown that we are able to produce single and individual e^-/h^+ pairs utilizing LEDs which leaves the door open for calibrating very-low energy devices without the need for an optical fiber to bring the photons in from room temperature. However, several improvements are suggested for future measurements, such as:

- Pre-biasing the detector by 20 V will improve the detector resolution. This is supported by the improved detector's resolution in the measurement at Northwestern University.
- Neutralizing the detector for an extended period of time (more than 24 hours) could potentially improve the detector resolution.
- Consider using an external trigger that is coincident with the LED drive pulse to minimize the background in the phonon signal.

5.7 Electron Gun

5.7.1 Introduction

The newly improved SuperCDMS detectors are expected to have energy thresholds in the range of a few eV. Therefore, new calibration methods at the proposed energy scale are necessary. Energies in this range are relatively easily accessible by accelerating electrons with potentials between a few volts and a few hundred volts, which is technically an easily accessible range.

The first prototype of an electron gun was designed, built and initial tests were performed. This section describes the design, construction, and tests performed as well as simulations that were conducted to aid the design and estimate the performance.

5.7.2 Motivation

The motivation for designing an electron gun is to calibrate detectors at any desired energy from a few eV to a few hundred eV, via producing a small number of electrons and accelerating them by an adjustable potential to eventually have a calibration source with a well-defined energy electron-bursts.

5.7.3 Prototype Design

The components of the e-gun were designed to fit into our 3-inch detector housing. The design is based on having the components listed below to be at different potentials. Therefore, the structure was supported by PTFE cylindrical supports. A sketch for the major components is shown in Fig. 5.30.

- LED holder, Top plate and Al film: 0 - 1 V
- Electron concentrating cylinder, Retarding grid and Wehnelt cylinder: 5 - 30 V
- Bottom plate: grounded (connected to the chassis)

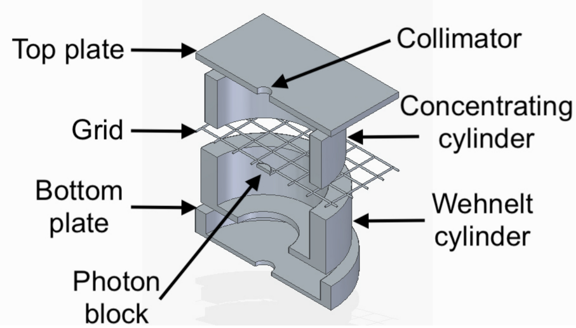

Figure 5.30: A cross-sectional view of the e-gun components. All components shown are held together via a PTFE cylinder to provide electrical isolation.

5.7.3.1 Design Specifications

Standard electron sources use heated filaments; however, in a cryogenic environment, this is not an option. Therefore, we chose to utilize the photoelectric effect. In this case, an ultraviolet LED was used to shine ~4 eV photons onto a 20 nm Al film coated on the bottom side of a UV-transparent fused-silica wafer of dimensions 30×20×1 mm^3, as shown in Fig. 5.31.

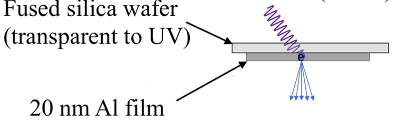

Figure 5.31: A cartoon for the photoelectric effect process at the Al film (not to scale).

To avoid interactions between UV photons and the silicon crystal (the detector), a 1 mm disk “photon block” was fixed at the center of the grid, in the line of sight of the LED, to block photons from directly reaching the detector underneath the bottom plate, as shown in the top left panel of Fig. 5.32.

The gird is located in the space between the two cylinders and aims to filter the electrons in order to have only electrons with well-defined energy passing through it towards the bottom plate.

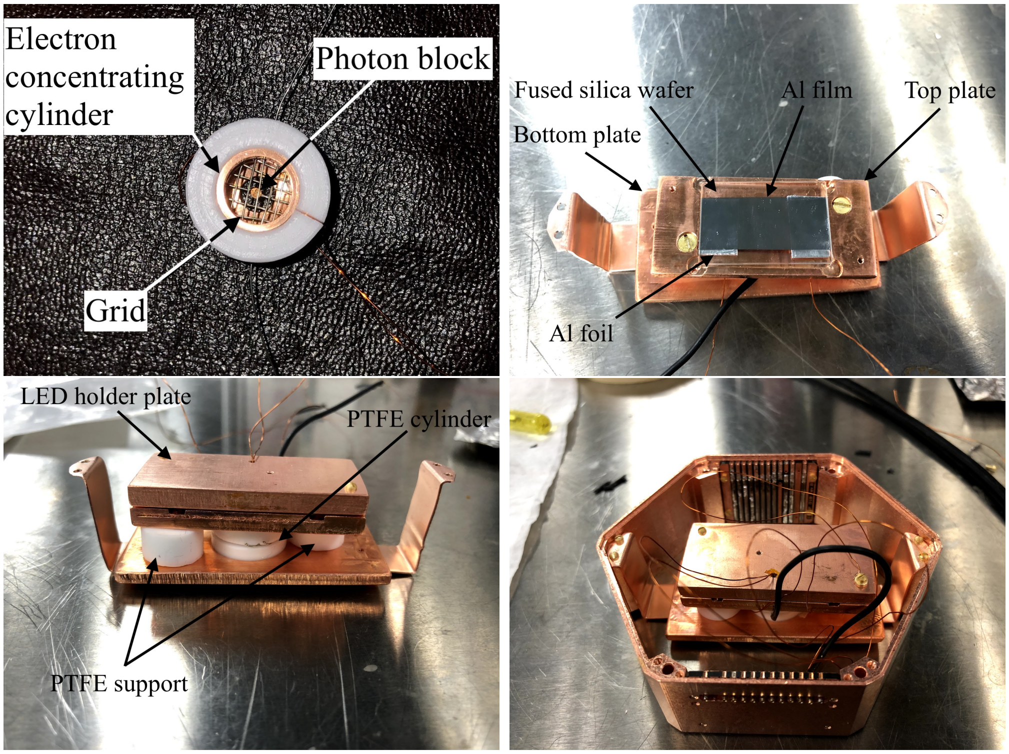

Figure 5.32: *Top Left*: Electron concentrating and Wehnelt cylinders are inserted into a PTFE cylindrical holder. The photon block (a 1 mm disc) is attached to the grid (in between the cylinders) in line of sight between the LED and the detector. *Top Right*: Fused silica wafer attached to its copper holder and supported by Al foil to enhance electrical contact at the top of PTFE support. *Bottom Left*: LED holder attached to the top plate. *Bottom Right*: The whole setup after assembly in an empty 3 inch detector housing.

A PTFE cylinder was produced to enclose the two copper cylinders and the grid at a fixed distance while keeping them electrically isolated, as depicted in the bottom and top left panel of Fig. 5.32.

5.7.3.2 Al Coating Process

The Al film was evaporated at the fused silica wafer using a vacuum system in which a pressure of $\mathcal{O}(10^{-5})$ mbar can be maintained. Then, a pure Al filament was heated via a high-voltage DC glow and a deposition rate of 500 A/sec was achieved. We have selected to have a thickness of 20 nm because the estimated absorption in Al is ∼9% for a 300 nm photons at room temperature [123]. This thickness should be sufficient for our purpose and we expect to be able to liberate electrons at a reasonable intensity.

5.7.3.3 Prototype Work Principle

The electrons are produced via the photo-electric effect, using a 310 nm (∼4 eV) InGaAsP LED shining on a 20 nm Al film (Al work function is about 4 eV [124]).

The liberated electrons from the Al film are then concentrated inside the top cylinder and filtered by their energy by adjusting the grid potential to moderate energies (a few, to a few 10s of eV). This can be achieved by controlling the bias voltages at different stages. Eventually, only electrons with the desired energy will be able to exit the bottom plate and hit the detector. Therefore, by controlling the accelerating potential, we can have well-controlled electrons at energies within the desired range.

5.7.3.4 E-Field Simulation

Since the emission spectrum of the photo-electrons is not well known, we assumed in our simulations a spectrum that decreases linearly from 0 to 1 eV. Simulations were performed with a retarding potential (V_R) of 0.8 eV and accelerating voltages (V_A) between 5 and 30 V. The electric field map is shown in the left panel of Fig. 5.33 and the electron trajectories for the same potential is shown in the right panel.

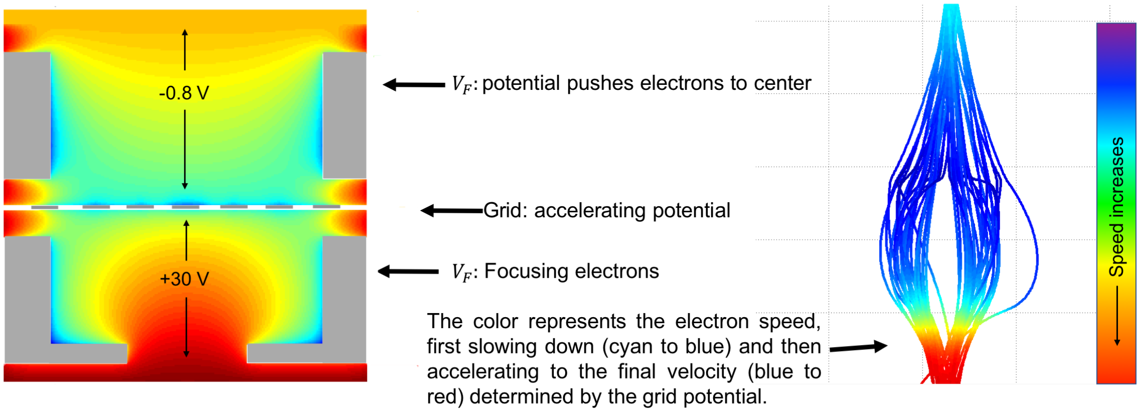

V_F: potential pushes electrons to center

Grid: accelerating potential

V_F: Focusing electrons

The color represents the electron speed, first slowing down (cyan to blue) and then accelerating to the final velocity (blue to red) determined by the grid potential.

Figure 5.33: *Left*: An example of a calculated E-field distribution within the e-gun, where the grid is set to 30 V in this example. *Right*: Simulation of the electron paths through the e-gun; tracks are shown only for electrons able to get past the retarding grid, and go through the collimator in the bottom plate. The color indicates the speed, to show for this potential electron can make it through the bottom plate (simulations performed by Wolfgang).

The focusing potential (V_F) was set equal to the accelerating potential and the bottom plate was always kept grounded (V_S). For the assumed emission spectrum, we found transmission of the order of a percent and - as expected - a very narrow energy distribution (with a spread of less than 1 eV).

5.7.4 Prototype Testing

5.7.4.1 Room Temperature Test Setup

An arbitrary-waveform function-generator (Agilent 33210A) was used to drive the LED circuit. A generic DC power supply to bias the top plate and a pico-ammeter (610C Keithley Instruments) to measure the current passing through the e-gun, as shown in Fig.5.34. In addition to that, the e-gun was situated in a vacuum chamber, where a vacuum of $\mathcal{O}\left(10^{-3}\right)$ mbar was achieved. A custom-made vacuum feed-through was built to feed the e-gun wiring to the readout electronics.

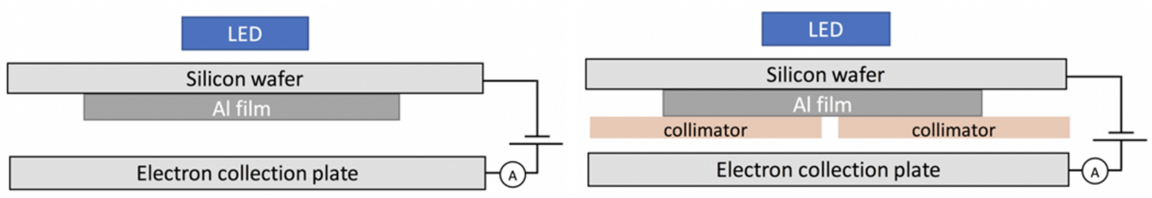

Figure 5.34: *Left*: A cartoon for the room temperature setup before adding the collimator. *Right*: The collimator is added in this setup is of $\phi \approx 1$ mm, and current is measured again to cross-check simulations with the actual produced parts (sketch not to scale).

5.7.4.2 Results from Tests at Room Temperature

As a first test, the electron emission from the Al film at room temperature was measured under vacuum, with the LED at 80% of its maximum emission. The emitted electrons were collected on a Cu plate biased at +12.5 V. A photo-current of 1.5±0.2 pA was measured using a pico ammeter connected between the collection Cu plate and Al film holder plate (a cartoon for the setup is depicted in the left panel of Fig. 5.34). This current was reduced to about 0.20±0.05 pA once the collimating top plate is added to the setup, as shown in the right panel of Fig. 5.34.

The number of measured electrons in the non-collimated measurement is $I_{meas.}/e$ $= 1.5\times10^{-12}/1.6\times10^{-19} = 9.38\times10^{6}$ electrons/second. For a pulse width of 50 μs, this will result in ∼470 electrons. While the number of measured electrons in the collimated setup was about 60 electrons, if we roughly assume a single-digit percent level transmission, as suggested by the simulations, this will lead to about 1 electron for the corresponding measured current.

Measurement type	# of measured electrons
Non-Collimated	468.8 ± 62.5
Collimated	62.5 ± 15.6

Table 5.7: Number of electrons emitted at room-temperature measurement. The error reported is the S.E.

5.7.5 Results of the Tests at Cryogenic Temperature

After the successful test performed at room temperature, the plan was to perform the next test at a cryogenic temperature at the TRIUMF test facility. However, certain circumstances did not allow for that for an extended period of time. In the meantime, we had the opportunity to install the e-gun assembly along with detector PD2 for run 11 at the CUTE Facility at SNOLAB (more details about detector PD2 can be found in Chapter. 4). But, due to the limited number of available readout wires in this run, we connected the three biasing voltages V_A, V_F, and V_R into a single output wire, which could lead to a spectrum of a wider range of energies. After cooling the dilution refrigerator at the CUTE facility, we were able to turn the LED on at optimal settings without causing any rise in the detector's temperature and varied the LED operational settings (pulse width and forward voltage) to confirm the change in the LED pulse energy, as depicted in Fig. 5.35. This only confirms that the LED turns on because we can clearly see the photon signal from the LED. In this plot, the red pulses show some noise frequency of an unknown source.

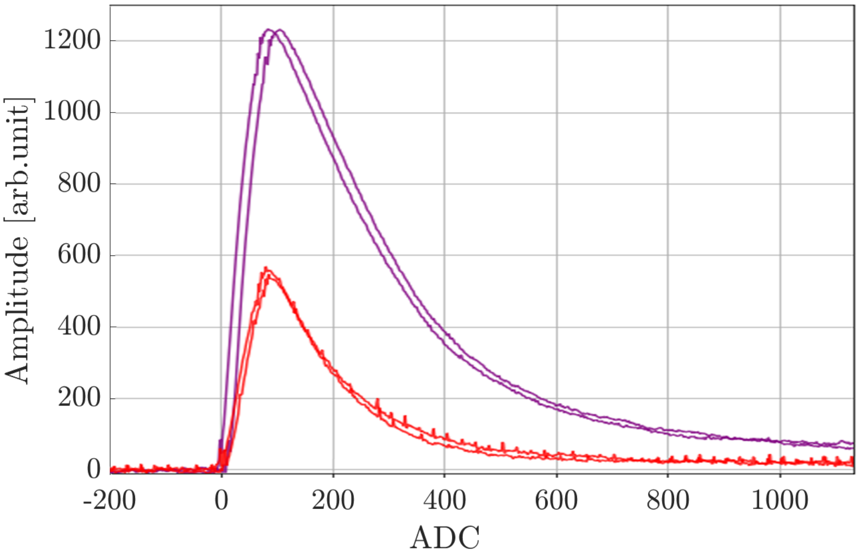

Figure 5.35: A selection of two pulses in PD2 when turning the LED on, showing a difference in pulse amplitude when the pulse width changes from 60 μs (in red) to 80 μs (in purple). Figure courtesy Adam Mayer.

Few data sets were taken while applying a range of voltages (between 0 to 100 V) at the e-gun components (V_A, V_F, and V_R). However, there was no indication that we had electrons being emitted from the Al film because there was no change nor amplification in the output phonon signal, as depicted in Fig. 5.36.

5.7.6 Future Work

The results from both tests, at room and at cryogenic temperature suggest that we in principle have the opportunity to liberate electrons from the Al film at our desired

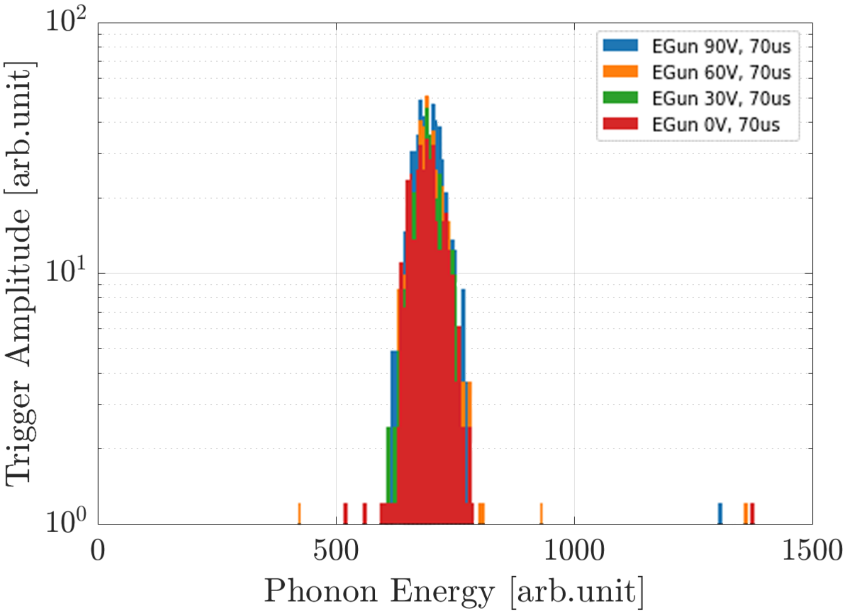

Figure 5.36: Trigger amplitude for detector PD2 while attempting to operate the e-gun and ramp the voltage to test the phonon signal amplification. Figure courtesy Adam Mayer.

intensity and energy range. However, more testing at a surface facility is required before we can perform such tests underground at the CUTE facility. The tests at the surface facility must confirm the emission of electrons, and the availability of readout cables will enable us to apply the required potential at each component of the e-gun to control the energy of emitted electrons. Once this has been performed, we think it will be reasonable to test that again at the CUTE facility and utilize the e-gun for future calibrations studies for the future SuperCDMS detectors.

Chapter 6

Conclusions

The field of dark matter search has developed over the past few decades and many experiments have competed, and still competing, to set new limits in the dark matter parameter space [125–127]. The lack of dark matter signatures in the current experiments has pushed through exploring other theories targeting various dark matter candidates, and some are motivated by the symmetries between dark and normal matter or dark sector [128] to explore the possibility of existing dark matter particles of mass less than 10 $\mathrm{GeV/s^2}$.

The future SuperCDMS SNOLAB experiment is aiming at the low-mass WIMP area [76]. This area of interest requires development in many aspects, such as the detectors' sensitivity to low-energy interactions, readout electronics, and mitigation of background sources. The work on the installation of the experiment at SNOLAB is still in progress and it is expected to start taking science data by early 2023.

The completion of the installation of the CUTE facility at SNOLAB will have a major impact on testing the future detector towers of the SuperCDMS experiment. In order to facilitate the detector testing, several modifications have already been made to accommodate the new towers into the dilution refrigerator at the facility.

Initial tests have been made utilizing a pathfinder tower and detector to confirm the compatibility of the produced parts. The pathfinder detector in addition to other devices has been used in several runs to study the fridge performance, evaluate the background levels, and to study the potential science reach at the facility. From the time of writing this thesis, it is over 2 years till SuperCDMS experiment is ready to start taking data. During this time, a full utilization for the CUTE facility will benefit the discovery of any issues with the detector towers before being installed at SuperCDMS and the first science data from the new detectors with new exclusion limits could potentially come from the CUTE facility.

We have measured the emission spectrum from an IR LED at room temperature and compared that with the emission spectra at cryogenic temperatures. We found that the value of the mean emitted wavelength decreases by about 10%. This change in the emission spectrum has a significant impact on the photon penetration depth in the crystal if the energy of the selected photons is close to the bandgap of the detector material.

Several tests have been performed to check the possibility of utilizing IR LEDs for calibration purposes at cryogenic temperatures. Tests revealed that the LED pulses are stable and the pulse energy was reproducible provided that the same setup and operational settings were used. Tests have also shown that we can operate LEDs in the proximity of eV-sensitive detectors without impacting their performance. Using the shadowing effect (described in section 5.4.3), we showed that the attenuation ratio in the LED pulse energy can be utilized to reach very low energies, and comparable to the energy threshold of the new SuperCDMS SNOLAB detectors.

The initial tests for the calibration studies via an electron source (e-gun) were promising and in agreement with simulations. The simulations suggest that with the measured photo-current, we can achieve the desired single - or few-electron pulses that would allow us to calibrate the detectors in the energy range from a few to roughly a hundred eV. The tests of the complete setup at low temperature are forthcoming and will be performed at the TRIUMF test facility, BC.

Bibliography

[1] I. Masina. Dark matter and dark radiation from evaporating primordial black holes. 4 2020. arXiv:2004.04740.

[2] S. Bhattacharjee and P. K. Sahoo. Big bang nucleosynthesis and entropy evolution in f(r,t) gravity. *The European Physical Journal Plus*, 135(4), Apr 2020.

[3] Asger G. Gasanalizade and Ramin A. Hasanalizade. Determination of dark energy and dark matter from the values of redshift for the present time, planck and trans-planck epochs of the big-bang model. 2011.

[4] M. Johnson-Groh. Inflation leaves its mark, Jul 2018. [online]. Available: https://astronomy.com/magazine/2018/07/inflation-leaves-its-mark.

[5] R. A. Alpher, H. Bethe, and G. Gamow. The origin of chemical elements. *Phys. Rev.*, 73:803–804, Apr 1948.

[6] C. Bernard, C. Sebastien, and G. Juan. Primordial black holes, dark matter and hot-spot electroweak baryogenesis at the quark-hadron epoch. 2019. arXiv:1904.02129.

[7] V. Antunes, I. Bediaga, and M. Novello. Gravitational mechanism for baryogenesis in the cosmological QCD phase transition. 11 2016. arXiv:1611.07802.

[8] G. Lazarides. Particles and the Universe. In *19th Hellenic School and Workshops on Elementary Particle Physics and Gravity*, 5 2020.

[9] A. Faessler, R. Hodak, S. Kovalenko, and F. Simkovic. Can one measure the Cosmic Neutrino Background? feb 2016.

[10] S. Hawking. Gravitationally Collapsed Objects of Very Low Mass. *Monthly Notices of the Royal Astronomical Society*, 152(1):75–78, 1971.

[11] J. Garca-Bellido, B. Carr, and S. Clesse. A common origin for baryons and dark matter. 4 2019. arXiv:1904.11482.

[12] Jeremiah P. Ostriker. Discovery of "Dark Matter" In Clusters of Galaxies. , 525C:297, November 1999.

[13] F. Zwicky. Republication of: The redshift of extragalactic nebulae. *General Relativity and Gravitation*, 41(1):207–224, 2009.

[14] V. C. Rubin, Jr. Ford, W. K., and N. Thonnard. Extended rotation curves of high-luminosity spiral galaxies. IV. Systematic dynamical properties, Sa -> Sc. , 225:L107–L111, November 1978.

[15] E. Corbelli and P. Salucci. The extended rotation curve and the dark matter halo of M33. *Monthly Notices of the Royal Astronomical Society*, 311(2):441–447, 01 2000.

[16] M. De Leo. Rotation curve of spiral galaxy messier 33 (triangulum), 2018. [online]. Available: https://commons.wikimedia.org/w/index.php?curid=74398525.

[17] M. Cristina, T. Anna-Maria, T. Ken Van, and W. Neal. First results on dark matter substructure from astrometric weak lensing. 2020. arXiv:2002.01938.

[18] D. Croon, D. McKeen, and N. Raj. Gravitational microlensing by dark matter in extended structures. *Physical Review D*, 101(8), Apr 2020.

[19] X. Huang, C. Storfer, A. Gu, V. Ravi, A. Pilon, W. Sheu, R. Venguswamy, S. Bankda, A. Dey, M. Landriau, D. Lang, A. Meisner, J. Moustakas, A. D. Myers, R. Sajith, E. F. Schlafly, and D. J. Schlegel. Discovering new strong gravitational lenses in the DESI legacy imaging surveys. 2020.

[20] ESA/Hubble. Hubble maps dark matter web in a large galaxy cluster, 2008. [online]. Available:https://www.spacetelescope.org/images/heic0802a/.

[21] David Kraljic and Subir Sarkar. How rare is the bullet cluster (in a cdm universe)? *Journal of Cosmology and Astroparticle Physics*, 2015(04):050050, Apr 2015.

[22] J. R. Brownstein and J. W. Moffat. The bullet cluster 1e0657-558 evidence shows modified gravity in the absence of dark matter. *Monthly Notices of the Royal Astronomical Society*, 382(1):2947, Nov 2007.

[23] P. A. R. Ade, N. Aghanim, M. I. R. Alves, C. Armitage-Caplan, M. Arnaud, M. Ashdown, F. Atrio-Barandela, J. Aumont, H. Aussel, and et al. Planck2013 results. i. overview of products and scientific results. *Astronomy Astrophysics*, 571:A1, Oct 2014.

[24] R.F.L. Holanda, S.H. Pereira, and Deepak Jain. Cosmic transparency and acceleration. *Physical Review D*, 97(2), Jan 2018.

[25] J. Limlingan. Standard Model, 2016. [online]. Available:https://sites.google.com/site/joshlimlinganphysicslife/particle-physics/standardmodelprezi.

[26] J. Sonneveld. Searches for physics beyond the standard model at the lhc. 2019.

[27] Edward W. Searching for a black hole in the outer solar system. 2020.

[28] K. Griest, Agnieszka M. Cieplak, and Matthew J. Lehner. New limits on primordial black hole dark matter from an analysis of kepler source microlensing data. *Phys. Rev. Lett.*, 111:181302, Oct 2013.

[29] Y. Wu. Peak statistics for the primordial black hole abundance. *Physics of the Dark Universe*, 30:100654, Dec 2020.

[30] B. Iason, D. Quentin, Deanna C. Hooper, and Laura Lopez-Honorez. Non-cold dark matter from primordial black hole evaporation. 2020.

[31] A. Albert. Investigating dark matter with cosmic gamma rays. In *Searching for Dark Matter with Cosmic Gamma Rays*, 2053-2571, pages 3–15. Morgan & Claypool Publishers, 2016.

[32] F. Wilczek. Problem of strong p and t invariance in the presence of instantons. *Phys. Rev. Lett.*, 40:279–282, Jan 1978.

[33] K Zioutas, M Tsagri, Y Semertzidis, T Papaevangelou, T Dafni, and V Anastassopoulos. Axion searches with helioscopes and astrophysical signatures for axion(-like) particles. *New Journal of Physics*, 11(10):105020, Oct 2009.

[34] S. Andriamonje, S. Aune, and et al. Search for solar axions: the CAST experiment. *AIP Conference Proceedings*, 878(1):395–401, 2006.

[35] I. Stern. ADMX Status. *PoS*, ICHEP2016:198, 2016. arXiv:1612.08296.

[36] S. C. Inan and A. V. Kisselev. A search for axion-like particles in light-by-light scattering at the clic. 2020. arXiv:2003.01978.

[37] G. Senjanovic and V. Tello. Strong CP violation: problem or blessing? 4 2020. arXiv:2004.04036.

[38] N. Crisosto, G. Rybka, P. Sikivie, N. S. Sullivan, D. B. Tanner, and J. Yang. Admx slic: Results from a superconducting lc circuit investigating cold axions. 2019.

[39] G. Rybka. Direct detection searches for axion dark matter. *Physics of the Dark Universe*, 4:14–16, 2014.

[40] Ricardo G. Landim. Dark photon dark matter and fast radio bursts. 2020. arXiv:2005.08621.

[41] T. Aralis, T. Aramaki, and et al. Constraints on dark photons and axionlike particles from the SuperCDMS Soudan experiment. *Phys. Rev. D*, 101(5):52008, mar 2020.

[42] J. Cooley. Overview of non-liquid noble direct detection dark matter experiments. *Physics of the Dark Universe*, 4:92–97, 2014.

[43] E. Aprile, J. Aalbers, and et al. Dark matter search results from a one ton-year exposure of xenon1t. *Phys. Rev. Lett.*, 121:111302, Sep 2018.

[44] D.S. Akerib, S. Alsum, H.M. Arajo, X. Bai, A.J. Bailey, J. Balajthy, P. Beltrame, E.P. Bernard, A. Bernstein, T.P. Biesiadzinski, and et al. Results from a search for dark matter in the complete lux exposure. *Physical Review Letters*, 118(2), Jan 2017.

[45] X. Cui, A. Abdukerim, W. Chen, X. Chen, Y. Chen, B. Dong, D. Fang, ChangC.bo Fu, K. Giboni, F. Giuliani, and et al. Dark matter results from 54-ton-day exposure of pandax-ii experiment. *Physical Review Letters*, 119(18), Oct 2017.

[46] P. Agnes, I.F.M. Albuquerque, and et al. Low-mass dark matter search with the darkside-50 experiment. *Physical Review Letters*, 121(8), Aug 2018.

[47] G. Aad, B. Abbott, J. Abdallah, S. Abdel Khalek, O. Abdinov, R. Aben, B. Abi, M. Abolins, O. S. AbouZeid, and et al. Search for new phenomena in final states with an energetic jet and large missing transverse momentum in pp collisions at sqrt(s)=8 s = 8 tev with the atlas detector. *The European Physical Journal C*, 75(7), Jul 2015.

[48] Annapaola de Cosa. LHC results for dark matter from ATLAS and CMS. In *12th Conference on the Intersections of Particle and Nuclear Physics*, 10 2015.

[49] C. Doglioni and D. Tovey. Searching for Dark Matter with the ATLAS detector, 2019. [online]. Available:https://atlas.cern/updates/atlas-feature/dark-matter.

[50] Super-Kamiokande Collaboration, :, K. Abe, and et al. Indirect search for dark matter from the galactic center and halo with the super-kamiokande detector, 2020.

[51] G. Shao-Feng, H. Hong-Jian, W. Yu-Chen, and Y. Qiang. Probing flavor structure of cosmic ray $e^{\mp}$ spectrum and implications for indirect dark matter searches. 2020.

[52] J. Bovy and S. Tremaine. On the local dark matter density. *The Astrophysical Journal*, 756(1):89, Aug 2012.

[53] R. W. SCHNEE. Introduction to dark matter experiments. *Physics of the Large and the Small*, Mar 2011.

[54] S. Lazanu, I. Lazanu, and G. Ciobanu. Modelling the transient processes produced under heavy particle irradiation. *Nuclear Instruments and Methods in Physics Research Section B: Beam Interactions with Materials and Atoms*, 269(4):498503, Feb 2011.

[55] A. Jim, B. Marco, and et al. Dark sectors 2016 workshop: Community report. 2016. arXiv:1608.08632.

[56] D. Kaplan, M. Luty, and K. Zurek. Asymmetric dark matter. *Phys. Rev. D*, 79:115016, Jun 2009.

[57] R. Agnese, A.J. Anderson, T. Aralis, T. Aramaki, I.J. Arnquist, W. Baker, D. Balakishiyeva, D. Barker, R. Basu Thakur, D.A. Bauer, and et al. Low-mass dark matter search with cdmslite. *Physical Review D*, 97(2), Jan 2018.

[58] T. Shutt, P. Barnes, A. Cummings, and et al. A cryogenic detector with simultaneous phonon and ionization measurement for background rejection. *Nuclear Instruments and Methods in Physics Research Section A: Accelerators, Spectrometers, Detectors and Associated Equipment*, 326(1):166–171, 1993.

[59] D.S. Akerib, P.D. Barnes, D.A. Bauer, P.L. Brink, B. Cabrera, D.O. Caldwell, R.M. Clarke, A. Da Silva, A.K. Davies, B.L. Dougherty, and et al. Preliminary limits on the wimp-nucleon cross section from the cryogenic dark matter search (cdms). *Nuclear Physics B - Proceedings Supplements*, 70(1-3):6468, Jan 1999.

[60] R. Schnee, R. Abusaidi, D. Akerib, and et al. Results of the Cryogenic Dark Matter Search. In H V Klapdor-Kleingrothaus, editor, *Dark Matter in Astro- and Particle Physics*, pages 569–574, Berlin, Heidelberg, 2001. Springer Berlin Heidelberg.

[61] D. S. Akerib, M. S. Armel-Funkhouser, M. J. Attisha, C. N. Bailey, L. Baudis, D. A. Bauer, P. L. Brink, R. Bunker, B. Cabrera, D. O. Caldwell, and et al. Exclusion limits on the wimp-nucleon cross section from the first run of the cryogenic dark matter search in the soudan underground laboratory. *Physical Review D*, 72(5), Sep 2005.

[62] R W Schnee. First Results from the Cryogenic Dark Matter Search at Soudan. *Nuclear Physics B - Proceedings Supplements*, 143:429–431, 2005.

[63] CDMS II COLLABORATION. Dark Matter Search Results from the CDMS II Experiment. *Science*, 327(5973):1619–1621, 2010.

[64] Z. Ahmed and et al. Search for inelastic dark matter with the CDMS II experiment. *Phys. Rev. D*, 83:112002, 2011.

[65] R. Agnese, A. J. Anderson, and et al. First direct limits on lightly ionizing particles with electric charge less than $e/6$. *Phys. Rev. Lett.*, 114:111302, Mar 2015.

[66] SuperCDMS SuperCDMS Collaboration, R. Agnese, and et al. WIMP-Search Results from the Second CDMSlite Run. sep 2015.

[67] ACS. American Cleanroom Systems, 2020. [online]. Available:https://www.americancleanrooms.com/cleanroom-classifications/.

[68] N. Smith. Development of Deep Underground Facilities, 2018. [online]. Available:https://indico.cern.ch/event/699961/contributions/3056786/attachments/1693141/2724683/2018-07-24_IDM_NJTS.pdf.

[69] S. Guetersloh, C. Zeitlin, L. Heilbronn, J. Miller, T. Komiyama, A. Fukumura, Y. Iwata, T. Murakami, and M. Bhattacharya. Polyethylene as a radiation shielding standard in simulated cosmic-ray environments. *Nuclear Instruments and Methods in Physics Research Section B: Beam Interactions with Materials and Atoms*, 252(2):319–332, 2006.

[70] J. Wilhelmi, R. Bopp, R. Brown, and et al. The water purification system for the daya bay reactor neutrino experiment. 2014.

[71] D.S. Akerib, P.D. Barnes, and et al. Preliminary limits on the WIMP-nucleon cross section from the cryogenic dark matter search (CDMS). *Nuclear Physics B - Proceedings Supplements*, 70(1-3):64–68, jan 1999.

[72] R. Schnee, D. Akerib, and et al. Results and status of the Cryogenic Dark Matter Search (CDMS). *Physics Reports*, 307(1):283–290, 1998.

[73] Z. Ahmed, D. S. Akerib, and et al. Search for weakly interacting massive particles with the first five-tower data from the cryogenic dark matter search at the soudan underground laboratory. *Phys. Rev. Lett.*, 102:011301, Jan 2009.

[74] SuperCDMS SuperCDMS Collaboration, R. Agnese, and et al. Low-Mass Dark Matter Search with CDMSlite. jul 2017.

[75] R. Agnese and et al. Low-mass dark matter search with cdmslite. *Phys. Rev. D*, 97:022002, Jan 2018.

[76] R. Agnese, A. J. Anderson, and et al. Projected Sensitivity of the SuperCDMS SNOLAB experiment. sep 2016.

[77] R. Agnese, A. J. Anderson, and et al. Search for Low-Mass WIMPs with SuperCDMS. feb 2014.

[78] G. Angloher, A. Bento, and et al. Results on light dark matter particles with a low-threshold CRESST-II detector. *The European Physical Journal C*, 76(1):25, 2016.

[79] D. S. Akerib and et al. Improved limits on scattering of weakly interacting massive particles from reanalysis of 2013 lux data. *Phys. Rev. Lett.*, 116:161301, Apr 2016.

[80] R. Basu Thakur. *The Cryogenic Dark Matter Search low ionization-threshold experiment.* PhD thesis, Illinois U., Chicago, 2014. [online]. Available: http://lss.fnal.gov/archive/thesis/2000/fermilab-thesis-2014-33.shtml.

[81] D. Abrams, D. S. Akerib, M. S. Armel-Funkhouser, L. Baudis, and et al. Exclusion limits on the wimp-nucleon cross section from the cryogenic dark matter search. *Phys. Rev. D*, 66:122003, Dec 2002.

[82] A. Kennedy. *SuperCDMS Prototype Detector Design and Testing*. PhD thesis, Minnesota U., 2017. [online]. Available: http://lss.fnal.gov/archive/thesis/2000/fermilab-thesis-2017-31.pdf.

[83] Charles Kittel. *Introduction to Solid State Physics*. Wiley, 8 edition, 2004.

[84] M. Ghaith. Calibration of Infrared Photons in Cryogenic Germanium Detectors. Master's thesis, Queen's University, Kingston, 2017-04. [online]. Available: https://qspace.library.queensu.ca/handle/1974/15657.

[85] N. Kurinsky. *The Low-Mass Limit: Dark Matter Detectors with eV-Scale Energy Resolution*. PhD thesis, Stanford U., Phys. Dept., 2018.

[86] K. Kimmo. Studies of transition-edge sensor physics : thermal models and noise. 2011.

[87] SuperCDMS SuperCDMS Collaboration, R. Agnese, and et al. Low-Mass Dark Matter Search with CDMSlite. jul 2017.

[88] C. Isaila. *Development of Cryogenic Light Detectors with Neganov-Luke Amplification for the Dark Matter Experiments CRESST and EURECA*. PhD thesis, Technische Universit at Munchen, 2010.

[89] R. A. Moffatt, B. Cabrera, B. M. Corcoran, J. M. Kreikebaum, P. Redl, B. Shank, J. J. Yen, B. A. Young, P. L. Brink, M. Cherry, A. Tomada, A. Phipps, B. Sadoulet, and K. M. Sundqvist. Imaging the oblique propagation of electrons in germanium crystals at low temperature and low electric field. *Applied Physics Letters*, 108(2):022104, jan 2016.

[90] B. Cabrera, M. Pyle, R. Moffatt, K. Sundqvist, and B. Sadoulet. Oblique propagation of electrons in crystals of germanium and silicon at sub-Kelvin temperature in low electric fields. page 3, apr 2010.

[91] R. Agnese, A.J. Anderson, T. Aramaki, I. Arnquist, W. Baker, D. Barker, R. Basu Thakur, D.A. Bauer, A. Borgland, M.A. Bowles, and et al. Projected sensitivity of the supercdms snolab experiment. *Physical Review D*, 95(8), Apr 2017.

[92] D. M. Mei, R. B Mukund, W. Z. Wei, and et al. Impact of charge trapping on the energy resolution of ge detectors for rare-event physics searches. 2019.

[93] E. Lopez Asamar. Low-threshold WIMP search at SuperCDMS. *Nuclear and Particle Physics Proceedings*, 273-275:395–398, 2016.

[94] W. Z. Wei, L. Wang, and D. M. Mei. Average energy expended per e-h pair and energy scale function for germanium-based dark matter experiments. 2016.

[95] R. H. Pehl, F. S. Goulding, D. A. Landis, and M. Lenzlinger. Accurate determination of the ionization energy in semiconductor detectors. *Nuclear Instruments and Methods*, 59(1):45–55, February 1968.

[96] J. Lindhard, V. Nielsen, M. Scharff, and P.V. Thomsen. Integral equations governing radiation effects. (notes on atomic collisions, iii). *Kgl. Danske Videnskab., Selskab. Mat. Fys. Medd.*, 33, 1 1963.

[97] R. Agnese, A. J. Anderson, and et al. Demonstration of surface electron rejection with interleaved germanium detectors for dark matter searches. *Applied Physics Letters*, 103(16):164105, may 2013.

[98] F. Ponce, C. Stanford, S. Yellin, W. Page, C. Fink, M. Pyle, B. Sadoulet, B. Serfass, S.L. Watkins, P.L. Brink, and et al. Measuring the impact ionization and charge trapping probabilities in supercdms hvev phonon sensing detectors. *Physical Review D*, 101(3), Feb 2020.

[99] B. S. Neganov and V. N. Trofimov. Colorimetric method measuring ionizing radiation. *Otkryt. Izobret.*, 146:215, 1985.

[100] N. Mast, M. Fritts, D.J. Sincavage, P. Cushman, and V. Mandic. An in-situ movable calibration source for cryogenic particle detectors. *Nuclear Instruments and Methods in Physics Research Section A: Accelerators, Spectrometers, Detectors and Associated Equipment*, 971:164070, Aug 2020.

[101] M. Abhold and C. Lovejoy. Chapter 14 - Field Detection of Nuclear Materials. In James E Doyle, editor, *Nuclear Safeguards, Security, and Nonproliferation (Second Edition)*, pages 411–446. Butterworth-Heinemann, Boston, second edition edition, 2008.

[102] CDMS Collaboration. CDMS Internal Pages. [online]. Available:https://confluence.slac.stanford.edu/display/CDMS/Home.

[103] W. Hampel and L. P. Remsberg. Half-life of ^{71}Ge. *Phys. Rev. C*, 31:666–667, Feb 1985.

[104] F. Pobell. *Matter and methods at low temperatures.* Berlin ; New York : Springer, c2007., 3rd, rev. edition, 1937.

[105] Ph. Camus, A. Cazes, A. Dastgheibi-Fard, K. Dering, G. Gerbier, W. Rau, S. Scorza, and X. Zhang. CUTE: A Low Background Facility for Testing Cryogenic Dark Matter Detectors. *Journal of Low Temperature Physics*, 193(5):813–818, 2018.

[106] Magnicon GmbH. Magnicon - physical research and instrumentation, 2016. [online]. Available: http://www.magnicon.com/squid-systems/noise-thermometer.

[107] CUTE Operations. CUTE Run 11 Slow Control Rack Noise Tests, 2020. [online]. Available: https://confluence.slac.stanford.edu/display/CDMS/CUTE+Run+11+Slow+Control+Rack+Noise+Tests#slowcontrol–737522443.

[108] CUTE Operations. Accelerometer Measurements. [online]. Available: https://confluence.slac.stanford.edu/display/CDMS/Accelerometer+Measurements#PurgeGas-2567727.

[109] S. M, Sze. *Physics of Semiconductor Devices*. John Wiley & Sons, New York, 2nd edition, 1998.

[110] J. Domange, A. Broniatowski, E. Olivieri, M. Chapellier, and L. Dumoulin. Quantum Efficiency for ElectronHole Pair Generation by Infrared Irradiation in Germanium Cryogenic Detectors. *AIP Conference Proceedings*, 1185(1), 2009.

[111] Camacho-Aguilera. *Ge-on-Si laser for silicon photonics*. PhD thesis, MIT, 2013.

[112] Y.P. Varshni. Temperature dependence of the energy gap in semiconductors. *Physica*, 34(1):149–154, 1967.

[113] A. J. Saldivar-Garcia and H. F. Lopez. Temperature effects on the lattice constants and crystal structure of a Co-27Cr-5Mo low-carbon alloy. *Metallurgical and Materials Transactions A*, 35(8):2517–2523, 2004.

[114] M.A. Humayun, M.A. Rashid, F.A. Malek, and A.N. Hussain. Effect of lattice constant on band-gap energy and optimization and stabilization of high-temperature InxGa1xN quantum-dot lasers. *Journal of Russian Laser Research*, 33(4):387–394, 2012.

[115] Ocean Optics Webpage. NIRQuest512-2.5 Specifications. [online]. Available: https://oceanoptics.com/product/nirquest512-2-5/#tab-specifications.

[116] TGP. Technical Glass Product. [online]. Available: https://technicalglass.com/enlarged_technical/lg_transmittance_graph.html.

[117] Marubeni, Inc., 2016. [online]. Available: http://www.tech-led.com/product/smc/.

[118] H. Kressel. *SEMICONDUCTOR DEVICES FOR OPTICAL COMMUNICATION*. Springer, Berlin, Heidelberg, 1982. [online]. Available: https://link.springer.com/book/10.1007/3-540-11348-7#about.

[119] Dmercer. Solid-state diodes and diode characteristics, 2017. [online]. Available:https://wiki.analog.com/university/courses/electronics/text/chapter-5.

[120] P. L. Fulmek, P. Haumer, F. P. Wenzl, W. Nemitz, and J. Nicolics. Time dependent and temperature dependent properties of the forward voltage characteristic of InGaN high power LEDs. *AIP Advances*, 7(3):035206, 2017.

[121] M. Ghaith, W. Rau, M. Peterson-Galema, P. Di Stefano, E. Fascione, R. Germond, and R. Underwood. New Approaches to Low-Energy Calibration of Cryogenic Detectors. *Journal of Low Temperature Physics*, pages 305–311, May 2020.

[122] G. G. Macfarlane, T. P. McLean, J. E. Quarrington, and V. Roberts. Fine structure in the absorption-edge spectrum of ge. *Phys. Rev.*, 108:1377–1383, Dec 1957.

[123] Optical properties of al at 300 nm. [online]. Available: https://psec.uchicago.edu/library/photocathodes/Optical_Properties_of_Aluminum_300nm.pdf.

[124] Y. Zhang, S. Krishnamoorthy, and et al. Reflective Metal/Semiconductor Tunnel Junctions for Hole Injection in AlGaN UV LEDs. may 2017.

[125] W. Rau. Dark matter search experiments. *Physics of Particles and Nuclei*, 42(4):650660, Jul 2011.

[126] C. Prez de los Heros. Status of direct and indirect dark matter searches, 2020.

[127] C. Amole, M. Ardid, I.J. Arnquist, D.M. Asner, D. Baxter, E. Behnke, M. Bressler, B. Broerman, G. Cao, C.J. Chen, and et al. Dark matter search results from the complete exposure of the pico-60 c3f8 bubble chamber. *Physical Review D*, 100(2), Jul 2019.

[128] K. Petraki and R. Volkas. Review of asymmetric dark matter. *International Journal of Modern Physics A*, 28(19):1330028, Jul 2013.

[129] M. Ghaith. IR Photon Calibration Studies, 2016. [online]. Available: https://cdms.phy.queensu.ca/cdms_restricted/Cryostat/Runs/Run_068/Run_068.html.

[130] M. Ghaith, X. Zhang, R. Underwood, and W. Rau. Feasibility Study for an IR-LED-Based Calibration System for SuperCDMS Detectors. *Journal of Low Temperature Physics*, 193(5):827–832, Dec 2018.

Appendix A

Tc Measurements at QTF

Here, I provide a summary of the internal documentation for runs 61 and 65 at Queen's Test Facility (QTF) where we were using eight samples bonded to the eight channels in a detector housing (ZB1T-19) and conncted at the two DIBs. Four of these samples labeled (1, 2, 3 & 4) are from SLAC while the other four samples labeled (A, B, C & D) are from TAMU. The transition temperatures (T_c) of SLAC samples were measured at the Stanford (KO-15) fridge. The Stanford fridge is known to have a base temperature offset of ∼19.5 mK.

A.1 Methodology

We used the Mixing Chamber heater to gradually increase the temperature of TES chips. The temperature was measured using a Noise Thermometer (a magnetic field fluctuation thermometer) [106].

A.2 Results

Comparison of results between Queen's and Stanford			
Channel	Stanford [mK]	QTF - Run 61 [mK]	QTF - Run 65 [mK]
SLAC-1	59	40	37
SLAC-2	64.5	48	44.2
SLAC-3	70.5	51.5	48.5
SLAC-4	74.5	53.5	50.1

A.3 Conclusion

T_c measurement in run 65 were lower than that in run 61 by ∼3.3 mK. We think that this is related to the installation of an optical fiber into the fridge between the two runs. It is conceivable that the optical fiber allows some radiation to pass through, to the detector housing, which may have increased the temperature of the detector. Thus, less transition temperature will be measured. Moreover, T_c values as measured at Stanford are higher than that measured at Queen's by ∼19.5 mK, due to offset in their base temperature.

Appendix B

More Results - Shift in Band Gap

This appendix aims to provide additional plots for an LED of wavelength 1200 nm. The analysis has already been introduced in section. 5.2.3, but these plots were not included to avoid redundancy.

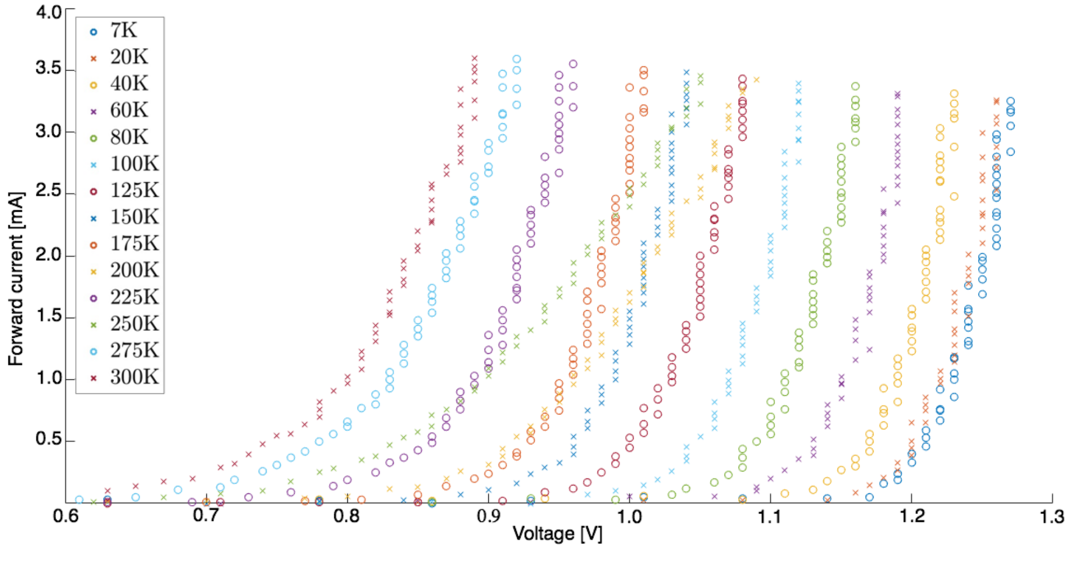

Figure B.1: IV curve for the 1200 nm LED as a function of temperature. See section 5.2.8 for more deteils.

The cut-in voltage was calculated from Fig. B.1, by fitting data points at each temperature to a line, after excluding the non-linear part of the curve, i.e. above

0.75 mA and the cut-in values for all temperature points are reported in Fig. B.2.

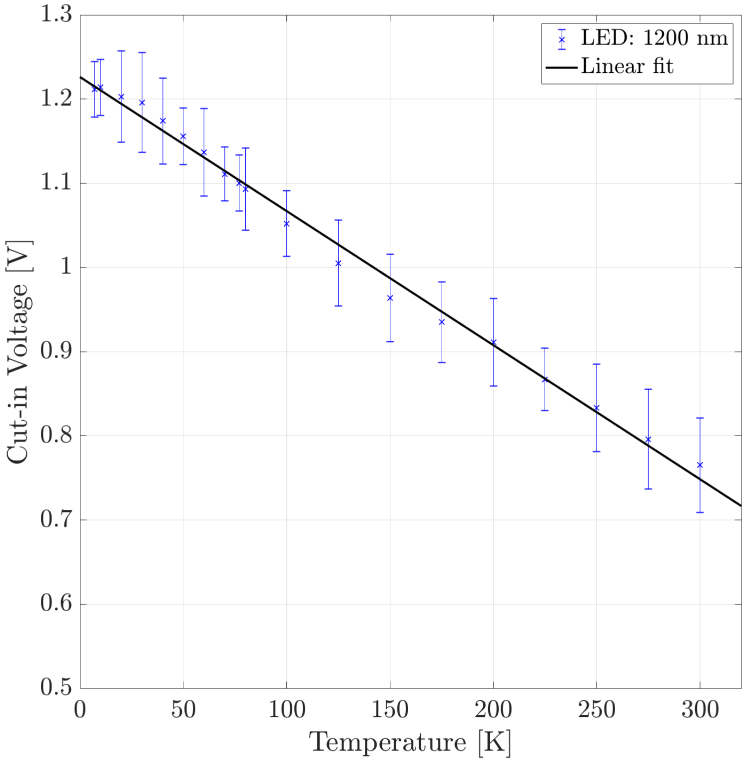

Figure B.2: Cut-in values for the 1200 nm LED as a function of temperature. Error bars for 95% C.L. See section 5.2.9.1 for more details.

The emission spectra for a 1200 nm LED were recorded at each temperature point for two current values, 1 mA and 3.3 mA as shown in Fig. B.3, through the LED using the Arduino circuit. For the 1 mA data, the emitted wavelength at room temperature was 1198±1 nm. After cooling down to 7 K, the measured peak emission at the same current value was 1149±1 nm. This resulted in a change of 49±2 nm. For the maximum current measurement at 3.3 mA, the peak emission at 7 K was 1143±1 nm giving a difference of 55±2 nm from room temperature.

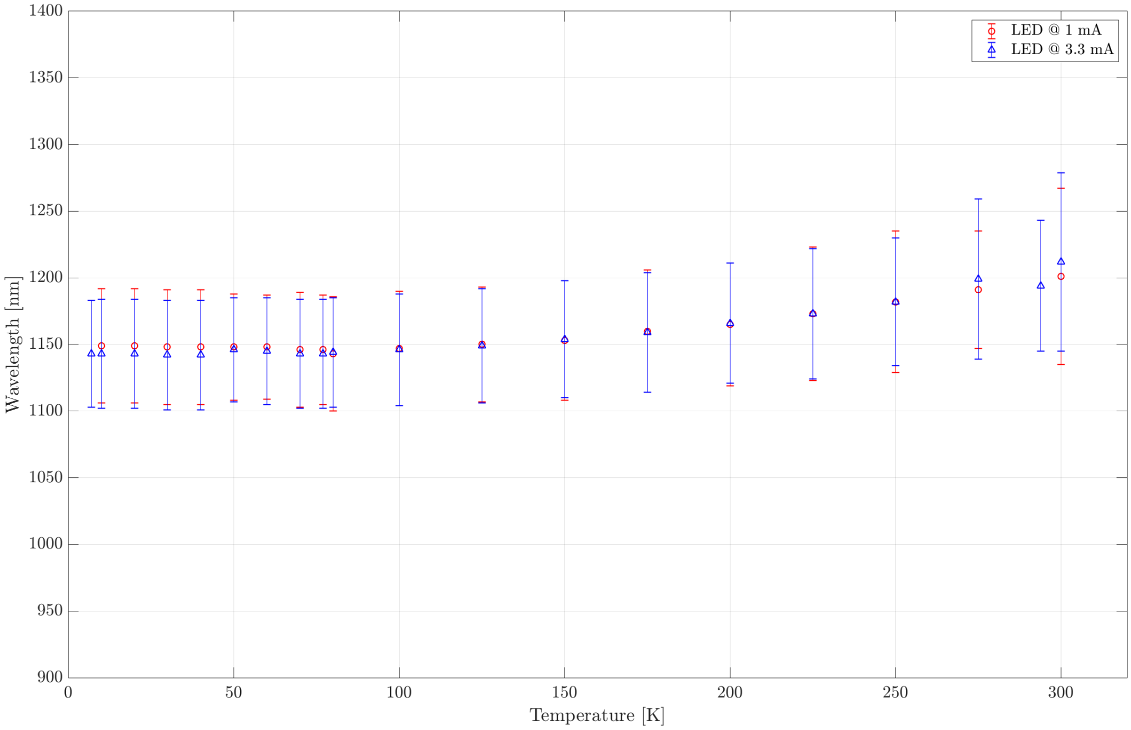

Figure B.3: The change in peak emission of 1200 nm at various temperatures. Error bars are the standard deviation of the Gaussian fit. See section 5.2.9.1 for more details.

Appendix C

Modifications to the Charge Readout Circuit

C.1 Introduction

This setup was designed for earlier studies [84], to be able to apply a high voltage (∼120 V) across one of the former Soudan detector, called G16.

The E-Box adapter, shown in Fig.C.1, included modifications to charge channels readout wiring, to protect the different components of the side coax from any potential current overload. This was done by connecting a 40 M resistor and shoring the Source and Drain lines. Then we added another 100 M resistors after shorting all charge lines to reduce the flowing current when high voltage is applied.

C.2 List of Modifications

We designed two modification boxes, where we made changes to readout wiring of Q_i and Q_o in the first, and Q_o only. in the second.

The pin assignments are listed in Table C.1, and they correspond to the 50 pin D-sub connector.

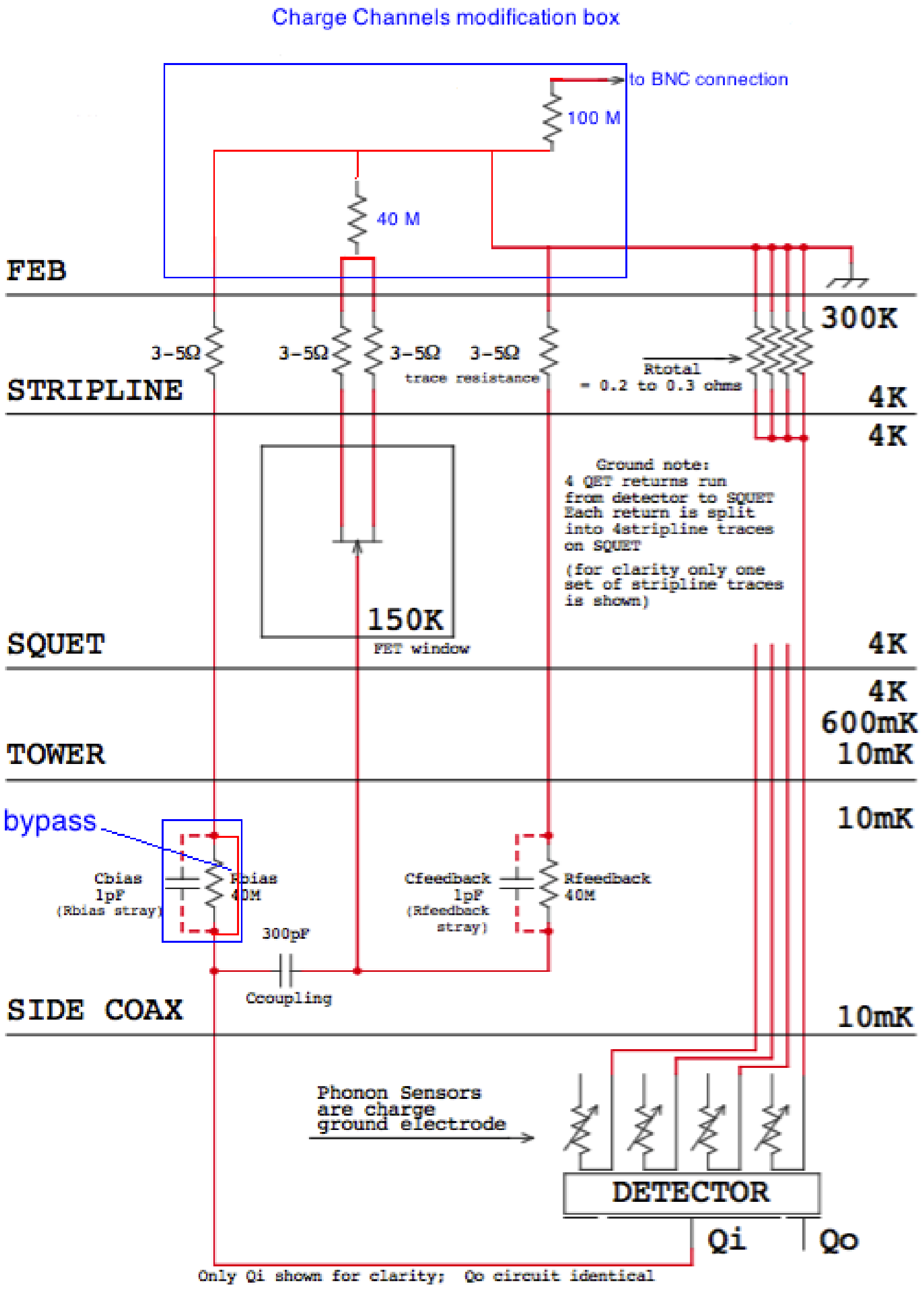

Figure C.1: A circuit diagram for a typical charge readout with modifications marked in blue

Pin No.	Pin Name	Modification
31 16	Q_iSource Q_iDrain	Q_iSource and Drain connected to a 40 MΩ
15 50	Q_iBias Q_iFB	Q_i (Bias, FB and the 40 MΩ resistor) are connected to a 100 MΩ resistor to Q_i of the BNC connector
27 12	Q_oSource Q_oDrain	Q_o (Source and Drain) connected to a 40 MΩ
11 31	Q_oBias Q_oFB	Q_o (Bias, FB and the 40 MΩ resistor) are connected to a 100 MΩ resistor to Q_o of the BNC connector

Table C.1: A list of pin assignments for the 50D-subminiature connector and the changes made to each line at the connection box

Appendix D

IR LED Study at RT

D.1 Introduction

To transmit the photons from the LED, while operated at room temperature, an optical fiber was installed in the cryostat to transmit the photons from the LED down to the detector surface.

Initial tests in utilizing LEDs to calibrate our detectors at Queen's Test Facility, full detail of the setup, data sets, and analysis can be found in Ref. [129, 130]. In the next section, I will only be showing the final result and a summary of the findings.

D.2 Summary of Results

The key finding that is related to section 5.5.4 is the comparison of the interaction position of the 1550 nm photons when operated at room temperature to that when it's cold. From Fig. D.1, we can say that penetration depth is closer to side 2, i.e. more charges were collected on side 2 than on side 1. So, to a first-order approximation, the interaction position can roughly be estimated as the ratio of the maximum number of charges collected on each side, which is $\sim(75/325) \approx 0.23$, multiplied by the detector thickness. This will give an estimate of ∼0.6 cm penetration into the detector (assuming a full charge collection efficiency).

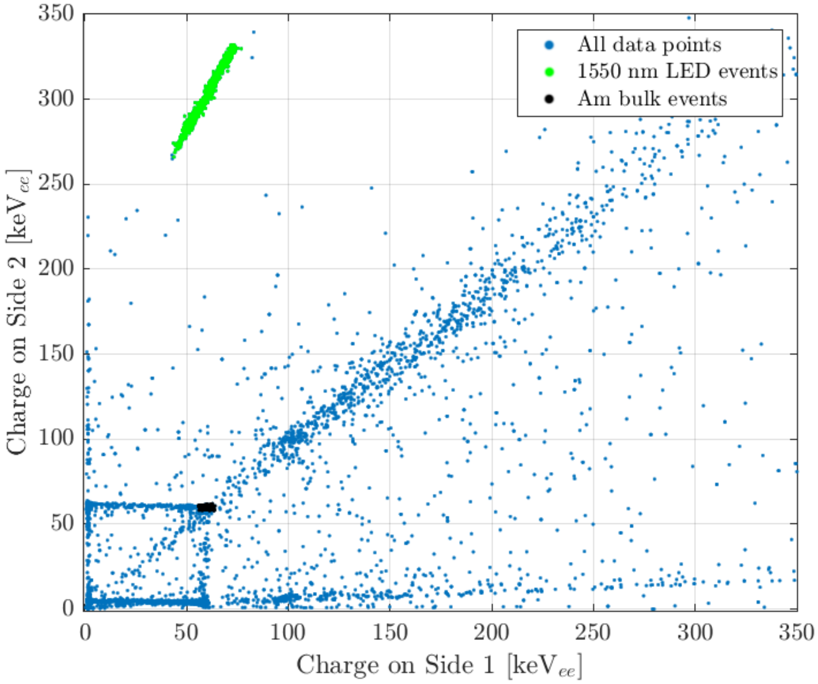

Figure D.1: The charge collected on side 2 vs. side 1 in detector G16K operated in iZIP mode at ±9 V. The events highlighted in black are from an ^{241}Am source and the ones highlighted in green are from a 1550 nm LED when operated at room temperature.